Aalto-yliopisto
Insinööritieteiden
korkeakoulu

Michael McCluskey

Error characterization for digital image correlation measurements in industrial environments

Diplomityö, joka on jätetty opinnäytteenä tarkastettavaksi diplomi-insinöörin tutkintoa varten.

Espoossa 31.07.2017
Valvoja: Sven Bossuyt

Aalto-yliopisto
Insinööritieteiden
korkeakoulu

Aalto University, P.O. BOX 11000, 00076
AALTO
www.aalto.fi

Abstract of master's thesis

Author Michael McCluskey

Title of thesis Error characterization for digital image correlation measurements in industrial environments

Degree programme Mechanical Engineering

Major/minor Mechanical Engineering **Code** IA3027

Thesis supervisor Sven Bossuyt

Thesis advisor Sven Bossuyt

Date 31.07.2017 **Number of pages** 78 **Language** English

Abstract

Digital image correlation (DIC) is a non-contact, full field displacement measurement technique. It is primarily suited to making high precision and high accuracy measurements, and is therefore commonly used in laboratories for experimental work. However, in recent years, improvements to technology and commercial interest in the industrial internet have created the potential for methods such as DIC to be utilized widely in industry.

This thesis makes a preliminary investigation of errors that are likely to occur when DIC is performed in an uncontrolled environment. The characteristics of displacement and strain field measurements affected by camera motion, changing focus and inconsistent illumination are compared. To achieve this, computer graphics software is used to simulate a scene in which a stationary plate is viewed by a stereo imaging system. Animations of systematic changes to camera position, focus and lighting are made, and a ray-tracing render engine is used to produce the resultant photo-realistic images. In later simulations, the plate is substituted for a cylinder in different orientations, to investigate how error characteristics vary with surface angle and distance.

The DIC algorithms are found to be robust, allowing viable measurements even when significant changes are made to the imaging environment. Changes to illumination and focus are seen to produce random noise, most likely resulting from incorrect matching of subsets. Conversely, camera motion is seen to result in systematic error, with each transformation component displaying distinct characteristics. This observation is significant, since it indicates a possibility for identifying and correcting for such errors in industrial applications. Surface curvature is found to have minimal impact on the error characteristics for most camera transformations, but significant differences are observed for camera translations along the y-axis and rotations around the x-axis.

Keywords DIC, Digital Image Correlation, Ray Tracing, Industrial Internet

Acknowledgements

I must express my most sincere gratitude to my supervising professor, Sven Bossuyt, for providing counsel, supportive resources, and funding for this thesis. His role in helping to choose a topic and providing academic guidance throughout my degree program are further appreciated.

I would also like to give my deepest thanks to my family, Ken, Bronwyn, Caitlin, Giles and Charlotte, for always taking an interest in my work and being supportive of me in all my endeavors.

Espoo 31.7.2017

Michael McCluskey

Table of Contents

Symbols

A	Camera to sensor coordinate system transformation matrix
a	Photometric transformation scale parameter
b	Photometric transformation scale parameter
c_i	Transformation by intrinsic camera parameters
D	Distance between camera and plate
$\bar{d}$	Current estimate of average motion
$\overline{\boldsymbol{d}}_{opt}$	Minimal displacement vector
e_L	Epipole in left image
e_R	Epipole in right image
E_{BA}	Reprojection error in bundle adjustment algorithm
F	Fundamental matrix
G	Transformed image
H	Reference image
I	Three-dimensional identity matrix
m	Apparent plate shift
P	Projective camera matrix
Q	Non-linear function giving image coordinates of real-world point
$\boldsymbol{R}$	Rotation matrix
R	Camera rotation component
s	Displacement measurement
s_{x0}	Initial grid spacing in x-direction
s_{y0}	Initial grid spacing in y-direction
T	Transformation by extrinsic camera parameters
$\boldsymbol{t}$	Translation matrix
t	Camera translation component
X	Three-dimensional point in the real world
x	Two-dimensional point on a camera image sensor
γ	Shear strain
Δ	Motion update
ϵ	Normal strain
θ	Camera rotation angle
ξ	Shape function
Φ	Photometric transformation
$[e_R]_\times$	Cross product matrix of right epipole

Abbreviations

1D	One-dimensional
2D	Two-dimensional
3D	Three-dimensional
BSDF	Bidirectional scattering distribution function
DIC	Digital image correlation
IIC	Industrial internet consortium
SSD	Squared sum of differences
ZNSSD	Zero-normalized sum of squared differences

1 Introduction

In recent decades, advances in computer, sensor and communications technology have allowed for the development of new measurement techniques that are finding use in a wide variety of fields. Among these, optical computer vision methods are particularly fast growing, and are utilized in research as well as both consumer and industrial applications. [1]

This thesis is focused on digital image correlation (DIC), a technique where conventional digital cameras can be used to measure deformation and strain. While a variety of computer vision methods can provide geometrical and displacement information, they are typically concerned with maximizing robustness and processing speed, which are essential in the dynamic, real-time applications where they are commonly applied. Conversely, DIC is most often used for experiments, and prioritizes precision and accuracy, sometimes down to the micro scale [2]. DIC is versatile, allowing for 2D displacement measurements with a single camera, or 3D measurements with multiple cameras. Furthermore, DIC measurements are both full field and non-contact, which combined with simple optical arrangement, ease of specimen preparation and relaxed requirements for the surrounding environment, make it a prominent technique in engineering research applications [3].

Currently, DIC is almost exclusively used in controlled environments. However, non-contact, full field, high precision measurement could also be extremely valuable in industry [4]. This is particularly the case in view of the developing industrial internet, which could serve to increase the value of placing sensors on devices and machines [5].

One especially useful quality of DIC is that it can be used to make measurements retrospectively. That is, the investigator does not have to know what they want to measure in advance, but can instead use DIC software to make measurements after the fact, as long as images are available. This means that introducing DIC to industrial applications is, for the most part, simply a case of monitoring with cameras. Conversely, traditional deformation measurement techniques, such as strain gauges, require the instrument to be placed in the precise location of interest. This becomes prohibitively expensive if, for example, one wishes to collect data throughout an entire factory.

DIC can provide any information that can be inferred from motion or deformation of a material surface. This includes strain, stress, vibrations, and crack detection or propagation. It can also be used to measure quantities that are not directly associated with motion, such as temperature [6]. If the economic value of this information outweighs the cost of installing cameras, then there is a case for the wide adoption of DIC in industry. Furthermore, the possible applications and value of installing cameras in industrial settings extends beyond DIC. For example, they can be used for security, performance monitoring, quality assurance and occupational health and safety.

Despite the potential benefits of DIC in industrial applications, there remain some significant barriers to its implementation. Some of these, such as data storage requirements and the prohibitive cost of quality cameras, will likely be resolved as relevant technologies improve and mature. However, to the knowledge of the author, there has been limited research on how the accuracy and reliability of DIC might be affected in an uncontrolled environment, where lighting conditions may vary and cameras have the possibility of being bumped by people or equipment. [4]

This thesis investigates possible DIC measurement errors that might occur in industrial settings. Specifically, it seeks to characterize the types of errors that result under variable illumination or when a camera is disturbed. The intention is to provide insight into how these errors can be recognized and compensated for without recalibration. Using computer graphics software, scenes of moving cameras and lights are created. Images of stationary objects within these environments are rendered, and then analyzed using commercial DIC software to investigate the resulting errors.

2 Background and theory

2.1 Overview and basic concepts of DIC

Digital Image Correlation is a full field, high precision, high accuracy, computer vision measurement technique. It is applied in a variety of research fields, and is commonly used for deformation and strain measurements in experimental mechanics [4]. A single camera can be used to measure in plane displacement of a surface. However, the research presented here is primarily concerned with 3D DIC, which utilizes multiple cameras to allow out of plane measurements.

Fundamentally, cameras are instruments that measure directions. That is, each pixel in an image corresponds to a particular direction from the camera's projection center. This means that a single camera provides no depth information and can only determine the location of a point in two dimensions. However, if the pixel location of a real-world point is known in multiple images, then its 3D location can be determined by computing the intersection of the light rays that correspond to those pixels. Determining motion is then a case of measuring changes in time and location between consecutive images. [2]

The central task in DIC is to identify corresponding feature points in multiple images. That is, for a given point in the real world, the aim is to determine on which pixel it lies in each image. Pixels can only take on a finite number of intensity values, so they are typically non-unique. Therefore, to find correspondences between different images, it is necessary to consider small neighborhoods of pixels, called subsets. For a given real-world point, the neighborhood of surrounding pixels will appear similar, but not identical, in each image. Therefore, the task of finding corresponding subsets of pixels in multiple images is an optimization problem, where the objective is to find the minimal discrepancy between neighborhoods. [7]

In order for 3D location of points to be computed, the orientation of the cameras must be known. Therefore, another important task in DIC is to accurately determine their location and pose. This is commonly achieved by capturing images of a calibration plate, which comprises a grid of marks with known dimensions. Here, we face another optimization problem, where the objective is to find the camera orientation that best fits the recorded images to the known dimensions of the calibration plate. [2]

2.2 The industrial internet

The future of the industrial internet is expected to provide new opportunities for technologies and techniques such as DIC, and thus serves as a key element of motivation for this research.

In recent years, an increasing number of devices, appliances and machines are being connected to the internet, which allows them to gather and share information. The industrial internet refers to this convergence of physical objects and intelligent data, and has been proposed as the foundation for a probable future of smart homes, smart cities and smart factories [8]. As developments are made that allow objects to share, access and utilize data more effectively, it is envisaged that significant increases to productivity and efficiency will be possible, with tangible benefits to individuals, society and the environment [5].

The perceived economic value in this data is evident from the significant commercial interest it has received. This includes the industrial internet consortium (IIC), which is comprised of hundreds of large companies across a multitude of industries [9]. It is clear that as information gathered by objects becomes more useful and valuable, so too do the sensors and algorithms that perform those measurements. This should especially be true for versatile sensors such as cameras. Since DIC facilitates high accuracy and precision measurements with conventional hardware, there are likely to be significant opportunities for its implementation in different applications as the industrial internet develops.

2.3 Digital photography

In order to understand DIC, it is first necessary to be familiar with some fundamental characteristics of digital photography. Cameras are instruments that measure light intensity in different directions. They work by using lenses to focus light rays through a small hole and onto a digital image sensor for a brief time interval. The sensor is divided into a grid of small regions known as pixels. Pixels gain charge depending on how much light they are exposed to. These charges are then recorded and removed from the sensor, after which subsequent images or frames can be captured.

The size of the hole through which the light is focused is referred to as the aperture, and the distance between the hole and the image sensor is the focal length. These, combined with shutter speed, determine basic photographic image properties such as brightness and depth of field. Figure *1* is an illustration of a simplified camera known as the perspective or pinhole model. Here it is assumed that all light rays are straight, and pass through the same point, referred to as the projection center. This model is sufficient for many computer vision applications. However, when large distortions can be expected, such as with wide-angle lenses, the more general projective camera model can be used. Unless otherwise stated, the pinhole camera model is assumed in the theory presented in subsequent sections of this thesis.

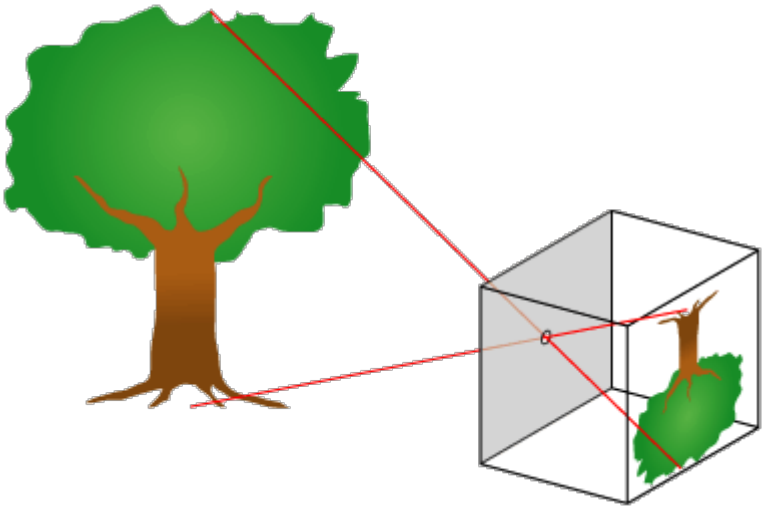

Figure 1 Pinhole-camera [10].

The properties of a particular camera define how it maps 3D points in the real world onto an image. The relationship between a real-world point, X, and its image on the sensor, x, can be described as follows:

$$\mathrm{x} = P\mathrm{X} = A[\boldsymbol{R} \mid \boldsymbol{t}]\mathrm{X} \tag{1}$$

where $P = [\boldsymbol{R} \mid \boldsymbol{t}]$ is known as the projective matrix of the camera, and encodes the rotation matrix $\boldsymbol{R}$ and translation matrix $\boldsymbol{t}$. These transform real-world points to their image on the sensor. A is the matrix that transforms the camera coordinate system to the sensor coordinate system. [7].

In relation to DIC, it is useful to consider some inherent limiting properties of digital cameras. The most significant consideration is that cameras do not provide depth or scale information, since each pixel simply corresponds to a light source in a given direction. Therefore, depending on the way cameras are arranged, the ability to accurately detect motion in certain directions may be limited. To obtain scale information, camera systems must be calibrated by observing something of known dimensions.

Another consideration is that there are several sources of noise when capturing digital images. Some of this is due to uncontrolled elements of the physical environment, such as dust particles or varying natural light. However, real optical systems always cause some degree of distortion and digital sensors are also imperfect and introduce further noise to measurements. In addition to noise, there is also a loss of information in digital photography. For example, small regions of the sensor are typically covered by wires and other hardware, making those sections insensitive to light.

2.4 Epipolar geometry

As mentioned, a single photograph can only provide two-dimensional information, so multiple images are required to make 3D measurements. A pair of images used for making such measurements is known as a stereo image pair. Given corresponding points in a pair of images, recovering 3D information is a simple case of determining the intersection of light rays as shown in figure *2*. For a real-world point X, if we know the coordinates x_L of its image in the left camera, we can determine one of the intersecting light rays using equation (1). The other light ray can be determined in the same manner from the point's image x_R in the right camera. However, before we can calculate this intersection, we first need a way of identifying corresponding points in our two images. The most obvious approach is to search through every pixel. However, computational cost can be reduced by making some geometrical assumptions.

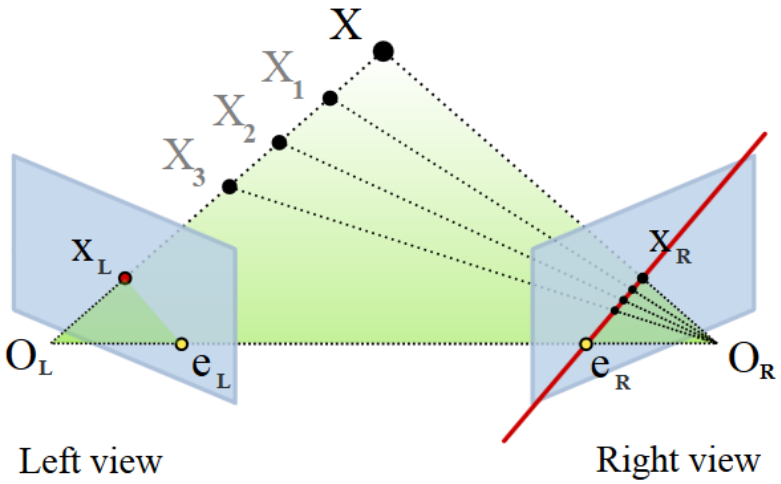

Figure 2 Epipolar geometry [11].

As seen in figure *2*, given that any three points must lie in the same plane, we can assume that a point in 3D space, X, and the projection centers of our two cameras are coplanar. This is known as the coplanarity constraint. The plane intersects with the two camera image planes to form two lines, known as epipolar lines. The epipolar line of the right camera is shown in red in figure *2*. If we assume that light rays are straight, then for a given image point x_L in the left image, the corresponding point x_R must lie on the epipolar line. This means that for a given image point, the task of searching for the corresponding point in the other image can be approximately reduced from a 2D search to a 1D search. [2]

Following from the derivation given by Birchfield [12] and using the form presented by Wöhler [7], the epipolar constraint can be written as:

$$x_L{}^T F x_R = 0 \tag{2}$$

Where x_L and x_R are expressed in homogeneous coordinates, and F is 3x3 matrix of rank two, known as the fundamental matrix. It encodes the orientation parameters of the camera system. For a given image point, equation (2) defines the epipolar line on which the corresponding image point must lie.

The line between the projection centers of the two cameras is known as the baseline, and the points where it intersects the image of each camera are known as epipoles. These are shown in figure *2* as e_L and e_R for the left and right images respectively. A concept of great significance to stereo measurement techniques, is that for any real-world point X, the corresponding epipolar line in each image passes through the camera's epipole [7]. Figure *3* shows several epipolar lines drawn onto one image from a stereo image pair. The lines were obtained by using the targets in the scene to mark corresponding points in the left and right images, which facilitated computation of the fundamental matrix. Note that each epipolar line passes through one of the circles, indicating which targets were used as corresponding points. The location of the epipole in this image is shown by the intersection of the epipolar lines.

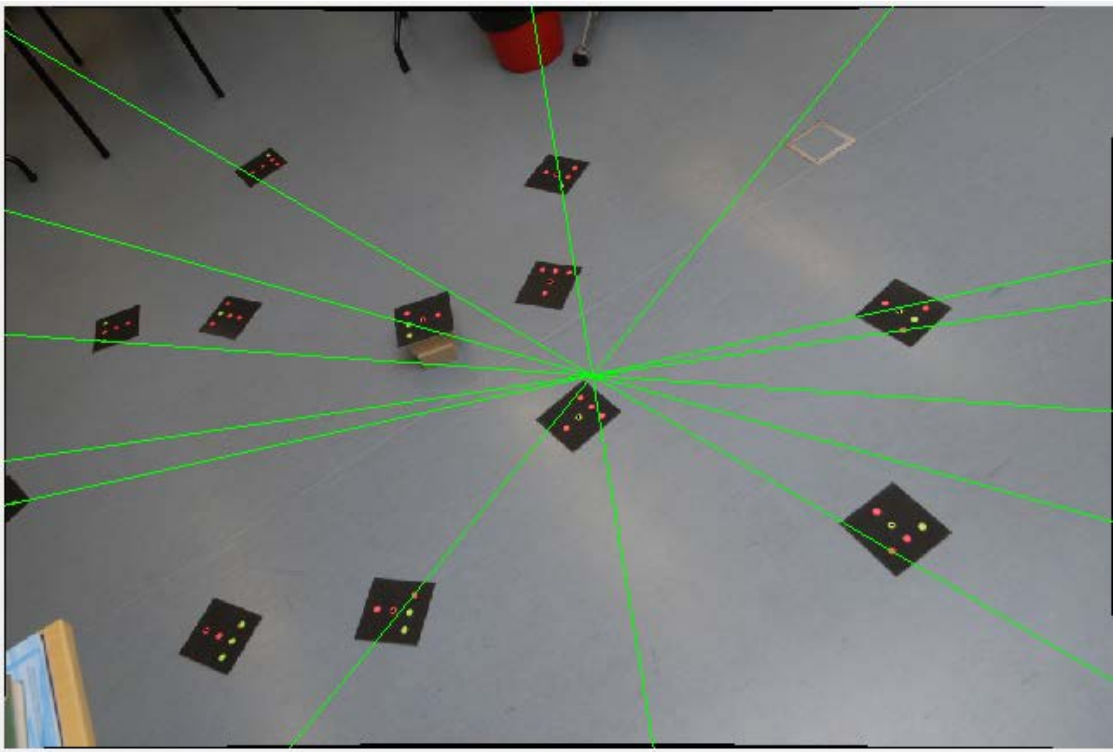

Figure 3 Epipolar lines for a stereo camera system, showing the location of the epipole for this camera [13].

2.5 Camera calibration

In order to make 3D measurements using DIC, the relative orientation parameters of the camera system must be determined. These can be separated into extrinsic and intrinsic parameters.

Extrinsic parameters describe the relative location and pose of the two cameras. If we take the location and pose of one camera to define the global coordinate system, then the required external orientation parameters are three rotations, describing the pose of the second camera, and two angles describing the direction of the second camera from the first. It should be noted that without an external reference, scale cannot be determined using computer vision methods. That is, the distance between the two cameras is unknown or arbitrary until otherwise defined by an object of known dimensions in the scene. The intrinsic parameters define a given camera according to whichever camera model is used. That is, they describe how real-world points are projected onto the image plane coordinate system. [7]

The projective matrices P_L and P_R contain the required calibration information, and can be recovered from the fundamental matrix F. Since we are using the projection center of one camera as the origin, let the projective matrix of the left camera be $P_L = [I \mid 0]$. Referring to equation (1), note that this projective matrix is comprised of the 3 x 3 identity for the rotation matrix and a zero translation matrix. The projective matrix of the right-hand camera is then given by:

$$P_R = \left[[e_R]_\times F \mid e_L\right] \tag{3}$$

where e_R and e_L are the left and right epipoles in homogeneous coordinates, and $[e_R]_\times$ is the 'cross product matrix'. If $e_R = (d, e, f)^T$, it is given by:

$$[e_R]_\times = \begin{bmatrix} 0 & -f & e \\ f & 0 & -d \\ -e & d & 0 \end{bmatrix} \tag{4}$$

Given equation (3), our calibration task is then to calculate the fundamental matrix F. This can be done by substituting a sufficient number of corresponding point pairs into equation (2). [7]

While it is possible and common in many computer vision applications to measure the geometry of an object and calibrate cameras simultaneously from one set of images, in DIC, calibration is typically performed separately [2,7]. This is because a high level of precision and accuracy is desirable, and more significantly, because DIC is commonly used to measure objects undergoing deformation.

In theory, the required corresponding point pairs can be acquired by taking images of any object with known geometry. However, the most common method is to use a plate with a regular grid pattern. Images are recorded with the plate in multiple poses and in different regions of the field of view.

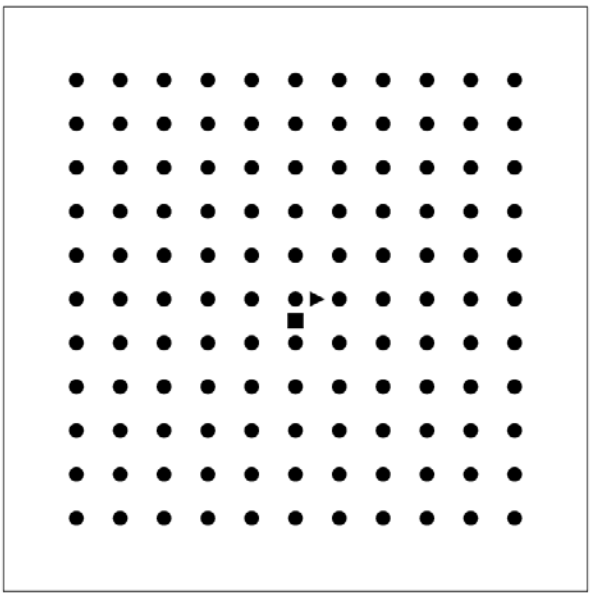

Figure 4 An example grid pattern used for DIC calibration.

Since the number of rows and columns in the grid pattern are known, corresponding points in different images can easily be identified. To ensure that this is performed accurately, a human usually marks some of these point pairs manually in the DIC software. Without additional assumptions or constrains, a minimum of eight point pairs are required to find the fundamental matrix [14]. However, to account for the effect of outliers, redundant observations are always made [15]. Instead of solving directly, a least squares optimization method known as bundle adjustment is used to find the parameters that best fit the set of image point observations to equation (2). [2]

2.6 Surface patterns for DIC

DIC measurements rely on successfully identifying points within an image based on a small subset of pixels. If the algorithm cannot match corresponding pixels in different images or matches them incorrectly, measurement errors will occur, or in some cases the measurement may fail altogether [16]. To aid in the identification of corresponding pixel subsets between multiple images, regions of the surface should be such that they are non-unique in appearance and are able to be easily measured by the cameras. In practice, this means that the imaged surface should have a coating or texture that is comprised of a high-contrast, non-periodic pattern. This randomness should be present at multiple scales to facilitate matching between images without the need for searching the entire field of view. In most applications, it is essential that this pattern is bonded to the material surface, so that the pattern deforms with the material [2].

A common and versatile method to achieve this goal is to spray paint the surface, first in a uniform light or dark color, then with a random speckle pattern in a contrasting color. Sutton et al. [2] find that this technique works well in a variety of applications, however more optimal methods have become available in recent years.

Bossuyt [16] presents a method for developing patterns with ideal characteristics for DIC. Specifically, patterns can be produced mathematically that show a statistically significant change in correlation for small displacements, while also exhibiting larger scale modulation that facilitates finding a specific neighborhood within the full field of view. That is, they contain unique arrangements of features at small scales that lie within regions that also appear unique at large scales. Other considerations are that the pattern should not contain features that are too small to be resolved by the imaging system, nor large featureless areas. An example pattern demonstrating these characteristics is shown in figure *5*.

Patterns with the characteristics described above have been utilized in experimental DIC measurements, and have been shown to produce accurate and reliable results [17]. These same patterns have been applied for DIC measurements performed in this work.

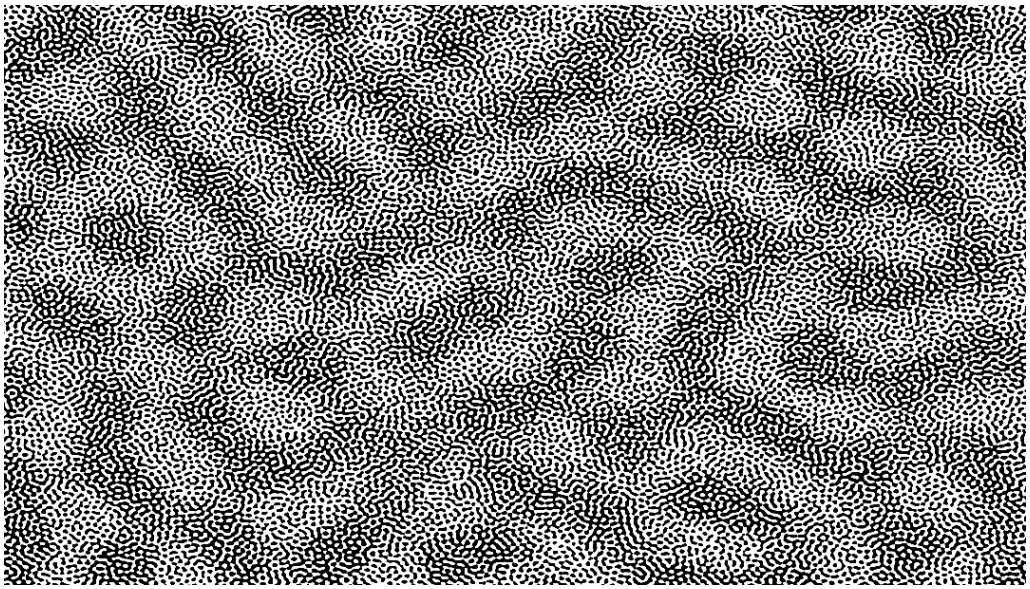

Figure 5 Example of an optimal surface pattern developed by Bossuyt [16] for DIC measurements.

2.7 Optimization algorithms in DIC

The main tasks of DIC are concerned with solving optimization problems. Calibration requires finding the fundamental matrix and projective matrices that best fit the observations of the calibration plate to equation (1). Similarly, when making DIC measurements, we seek a best fit between neighborhoods of pixels in different images. This includes finding subsets along the epipolar lines in stereo image pairs for 3D DIC, and also finding corresponding subsets between consecutive images in both 2D and 3D DIC.

It should be noted that in many cases, direct solution methods are available, however optimization methods offer numerous advantages. Firstly, they allow for the use of redundant measurements, which increases robustness and decreases sensitivity to outliers. Additionally, in the case of calibration, common direct linear methods cannot determine non-linear camera intrinsic parameters, such as lens distortion [2].

Iterative least squares optimization methods are widely used in DIC. While there are many different algorithms that may be suitable depending on the application, the following general optimization procedure is common:

1. An initial estimate of the solution is made.
2. The squared errors between the predicted image projections and the actual observations are calculated. These discrepancies are known as residuals.
3. The weighting of each observation is adjusted.
4. The closest solution to the re-weighted data is calculated.
5. The procedure is repeated from step 2.
6. Iterations are continued as per step 5 until the solution converges to within a chosen threshold.

2.7.1 Bundle adjustment

Bundle adjustment is a commonly used optimization method in modern DIC stereo calibration. It was first introduced to computer vision by Lavast et al. in 1998, though it had been used in photogrammetry applications for decades prior [2]. Bundle adjustment is an iterative least squares method, which determines a solution giving the location of observed 3D points at the same time as extrinsic and intrinsic camera parameters. It utilizes redundant observations to find a best fit and gives precise results that can be easily interpreted for error analysis and quality control [18]. This means that a solution can be found that incorporates all the information from image observations of the calibration grid in multiple poses and that it is possible to assess the quality of the calibration.

The main principle of the method is that an estimate of the solution is used to model expected observations which are then compared with the real measurements. The optimization goal is to minimize the difference between these two values, known as the reprojection error. This can be expressed mathematically by considering observed image points x_{ik} and the non-linear function $Q(T_i, c_i, \mathrm{X}_k)$ that gives the modeled image coordinates of real-world point X_k, following transformation by extrinsic camera parameters T_i and intrinsic parameters c_i. The reprojection error to be minimized is then given by:

$$E_{BA} = \sum_{i=1}^{L} \sum_{k=1}^{K} \| Q(T_i, c_i, \mathrm{X}_k) - \mathrm{x}_{ik} \|^2 \tag{5}$$

where L is the number of images and K is the number of observed real-world points [7]. Applying a process similar to that presented in section 2.7, a solution that minimizes (5) can be found.

2.7.2 Image matching

Given a calibrated camera system, image matching is the core task of DIC. The goal is to identify which pixels in one image correspond to which pixels in another image. The two images could be subsequent frames taken at different times, or in the case of 3D DIC, they could be recorded with different cameras at the same time.

Image matching is non-trivial, since a given pixel value may occur many times within the same image. As mentioned previously, this is accounted for by searching for a corresponding local neighborhood of pixels, however, this too presents challenges. Illumination may vary between frames, which could cause significant pixel value discrepancies in different images. Also, given that DIC is largely concerned with measuring deforming objects, it cannot generally be assumed that the shape of subsets is conserved between frames. Random noise and bias further add to the challenge of correctly matching between images. [2]

Multiple algorithms exist for image matching, and the best choice may depend strongly on the specific application [2]. Significant considerations are computation speed, accuracy and robustness. Described here are the basic concepts of a common template matching process known as the Lucas-Kanade tracker algorithm, presented in the form and notation used by Sutton et al. [2].

The method estimates motion by minimizing the difference between a template local pixel subset in one image and a transformed copy of that template in another image. If we first assume that no lighting changes occur between frames, then we can define a best fit of matching subsets by minimizing the squared sum of differences (SSD) between pixel gray values in those sets. Mathematically, this can be expressed as:

$$\bar{\boldsymbol{d}}_{opt} = argmin \sum \left\| G\left(x + \bar{\boldsymbol{d}}\right) - H(x) \right\|^2 \tag{6}$$

where H is the reference image from which the template is taken and G is the transformed image. $\bar{\boldsymbol{d}}_{opt}$ is the value of displacement vector $\bar{\boldsymbol{d}}$ that brings G as close as possible to H over all the pixels in the subset. This objective function can be expanded into a first order Taylor series, giving rise to an iterative algorithm that can be used to solve for $\bar{\boldsymbol{d}}_{opt}$. This can be expressed as:

$$\chi^2\left(\bar{d}_x + \Delta_x, \bar{d}_y + \Delta_y\right) = \sum \left\| G\left(x + \bar{\boldsymbol{d}}\right) - \frac{\partial G}{\partial x}\Delta_x - \frac{\partial G}{\partial y}\Delta_y - H(x) \right\|^2 \tag{7}$$

where $\bar{d}_x$ and $\bar{d}_y$ are current estimates for the average motion of the subset and Δ_x and Δ_y are motion updates sought incrementally at each iteration. Taking partial derivatives of (7) with respect to Δ_x and Δ_y and setting them to zero gives the following linear equation system for updating motion:

$$\begin{bmatrix}\Delta_x\\ \Delta_y\end{bmatrix} = \begin{bmatrix}\Sigma(\frac{\partial G}{\partial x})^2 & \Sigma\frac{\partial G}{\partial x}\frac{\partial G}{\partial y}\\ \Sigma\frac{\partial G}{\partial x}\frac{\partial G}{\partial y} & \Sigma(\frac{\partial G}{\partial y})^2\end{bmatrix}^{-1}\begin{bmatrix}\Sigma\frac{\partial G}{\partial x}(H-G)\\ \Sigma\frac{\partial G}{\partial y}(H-G)\end{bmatrix} \tag{8}$$

Equation (8) can then be used to make incremental improvements to $\bar{\boldsymbol{d}}$ according to:

$$\bar{\boldsymbol{d}}^{n+1} = \bar{\boldsymbol{d}}^{n} + \Delta \tag{9}$$

This iterative process continues until the displacement converges to $\bar{\boldsymbol{d}}_{opt}$.

The SSD optimization criterion presented in equation (6) can detect arbitrarily large motions as long as the initial estimate falls within the convergence radius. However, it cannot account for variations in lighting that may occur between images. To account for this, different optimization criteria can be used. One possibility is the normalized cross-correlation criterion, which attains a maximum for identical subsets and is independent of intensity scale. However, it is computationally expensive and therefore not ideal. Presented here is one suitable alternative that can manage changes in both offsets and scale changes in lighting. Firstly, the following photometric transformation of G is made:

$$\Phi(G) = aG + b \tag{10}$$

where a and b are additional parameters related to the change in scale and offset respectively. Creating a new criterion with Φ, and using a similar form to the SSD gives:

$$\chi^2 = \sum(aG_i + b - H_i)^2 \tag{11}$$

At a given iteration, optimal values for a and b are given by:

$$a_{opt} = \frac{\Sigma\bar{H}_i\bar{G}_i}{\Sigma\bar{G}_i^{\,2}}$$
$$b_{opt} = \bar{F} - \bar{G}\frac{\Sigma\bar{H}_i\bar{G}_i}{\Sigma\bar{G}_i^{\,2}} \tag{12}$$

where $\bar{H}$ and $\bar{G}$ are the average values of H and G across all the iterations, $\bar{H}_i = H_i - \bar{H}$, and $\bar{G}_i = G_i - \bar{G}$.

This optimization criterion is suitable when lighting conditions vary. However, it still has one significant limitation, in that it assumes that square pixel subsets remain approximately square. In the majority of DIC applications, it is desirable to be able to match subsets between images of a deforming object. An example of this, presented by Sutton et al. [2] is shown in figure *6*.

To facilitate matching of deformed subsets, a shape function $\xi(x,p)$ can be introduced that approximately transforms pixel coordinates in the reference subset to coordinates in

the deformed image. Incorporating this into the SSD criterion in the same form as equation (6) gives:

$$\chi^2(p) = \sum (G(\xi(x,p)) - F(x))^2 \tag{13}$$

The ideal choice of shape function depends on the type and extent of subset deformation, balanced against computational complexity. While there are numerous considerations, it is essential that the selected function can accurately represent the displacement field over the size of the subset. If the function cannot accurately represent the deformation, then decorrelation may occur, and the algorithm may fail to correctly match subsets. [2]

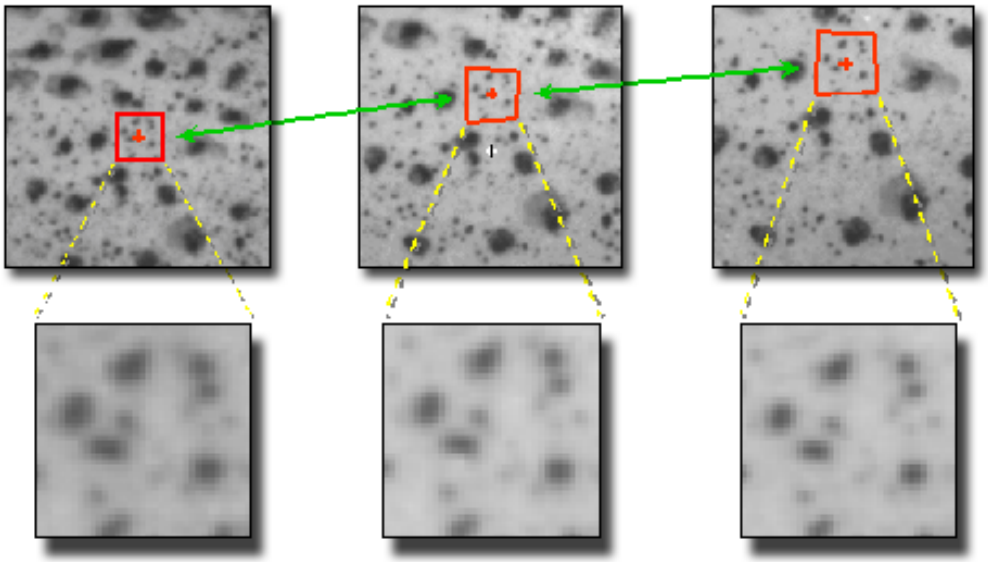

Figure 6 Pixel subset matching between images [2].

2.7.3 Sub-pixel accuracy

DIC is performed by determining corresponding pixels between images, so it is intuitive to think that this is the limit of precision. However, it is possible and common for DIC systems to make measurements with sub-pixel accuracy [19].

If a border between light and dark features lies somewhere on a pixel, then the grayscale value of that pixel will depend on the location of the border. Therefore, measuring with sub-pixel accuracy requires interpolation. Several interpolation schemes exist, however Pan et al. [20] find that the iterative spatial domain cross-correlation algorithm is the most accurate. Other schemes may be preferable when computational speed is a priority, however this is not typically the case in DIC applications. Since the choice of interpolation scheme determines how sub-pixel displacement is measured, it can also be a source of measurement error. [21]

2.8 Error sources and implications for industrial applications

Consideration of the image acquisition, calibration and image matching processes provides insight into common error sources in DIC. Table *1* lists some of the error sources identified by Pan et al. [21]. These errors can be separated into two categories, those

relating to experimental setup and hardware, and those related to computation. In a controlled environment, these error sources are generally manageable, and in recent years DIC has been repeatedly reported as a reliable, precise, and accurate measurement technique [20]. However, some aspects of error in DIC measurements are not fully understood or consistently dealt with by experimentalists, and error estimation remains an area of investigation [22]. In uncontrolled environments, it is likely that the effects of many error sources would be increased, and as such, investigations into characterizing and managing error in DIC are required. The scope of this thesis is limited to errors that might be caused by disturbance of cameras and changing lighting conditions. However, a wider variety of error sources and their potential implications for industrial applications are mentioned briefly in this section.

As discussed in section 2.6, an inappropriate choice of speckle pattern can have a significant impact on results. DIC algorithms rely on the surface pattern to identify corresponding pixels between images. Therefore, if the pattern is inadequate, then the system may incorrectly match subsets, and measurement error or failure will occur.

In the case of 2D DIC, it is essential that the camera sensor and measured surface are parallel, and that there are no out of plane displacements. While stereo vision systems are capable of measuring out of plane displacement, sensitivity and accuracy can be heavily dependent on placement and pose of the cameras [2]. For example, cameras placed close together with approximately the same pose will not be sensitive to out of plane motion. Placing cameras far apart and angled a long way toward each other allows the system to detect motion in all directions, however, this causes the scene to appear significantly different in each camera, and may lead to correlation difficulties and reduced accuracy in some cases [2]. Choosing an appropriate experimental setup for the conditions and desired measurements is therefore very important. This could be particularly relevant in industrial applications, where non-ideal lighting conditions or surface patterns could exacerbate the effects of poor experimental setup.

Image distortion and noise can have considerable influence on the accuracy of DIC measurements [23,24]. Lenses and sensors are both causes of such errors, and therefore the best results can be achieved by using high quality cameras. This is again of significant importance for industrial applications, since the expense of such equipment may be prohibitive. Therefore, before DIC can be widely adopted, investigations may be required to examine the feasibility of using lower quality cameras and balancing equipment choice with accuracy and precision requirements for certain applications.

The size of pixel subsets can also affect the accuracy of DIC measurements. If subsets are too small, then they may not be sufficiently distinct from each other, and correct image matching may not occur. However, large subsets are more likely to undergo complex deformation and are therefore more difficult to accurately approximate with shape functions. For this reason, commercial DIC software packages typically allow the user to select a subset size based on their requirements. [21]

Table 1 Error sources in DIC

Errors related to experimental setup	Speckle pattern Non-parallel sensor and object surface (2D DIC only) Out of plane motion and camera orientations Image distortion Noise
Errors related to DIC algorithms	Subset size Optimization criterion Sub-pixel algorithm and interpolation scheme Shape function

As discussed in section 2.7.2, there are many possible selections of optimization criteria for image matching. Since the chosen optimization criterion determines how matching subsets are identified, it can affect the results. In some cases, a poor choice could lead to correlation failure where others might not [21]. However, Tong [25] finds that of one commonly used criteria, the zero-normalized sum of squared differences (ZNSSD) offers both the best reliability and robustness. Some other criteria are less computationally expensive, resulting in faster measurements. Speed is not usually a high priority in DIC applications since measurements can be made a posteriori, however the ability to adjust the balance between speed and robustness could be useful in some applications.

The role of shape functions in DIC algorithms was briefly mentioned in section 2.7.2. The choice of shape function, along with the subset size, determines how well the shapes of deformed subsets are approximated, and thus influences measurement errors [2]. For example, Lu and Cary [26] find that second order and linear shape functions produce similar error for small displacements, but that the accuracy of second order functions degrades less rapidly as deformation increases.

Of the errors mentioned above, those related to experimental setup have the potential to become more significant in uncontrolled environments. In general, errors arising from the DIC algorithms would not be directly influenced by the environment, as measurements are performed independently of image acquisition. However, since image quality may be compromised, the best choice of algorithms could differ in some situations. For example, with poor images, it may be preferable to prioritize robustness over accuracy.

2.9 Ray tracing software

The investigations presented in this thesis utilize ray tracing software to simulate image pairs from which DIC measurements can be made. Ray tracing is a global illumination rendering method that can produce photo-realistic images. It is so called because it comprises tracing light rays through a virtual scene and accurately modeling their behavior when they interact with surfaces. The task of rendering an image is then to determine how much light from each object in the scene is eventually reflected through each pixel in the camera [27]. This is relatively straight forward if every surface is comprised of well-understood materials, however, surfaces with complex reflectance properties can be very difficult to model [28].

Ray tracing software is commonly used in computer graphics and game development, and is therefore widely available. Figure 7 shows an example of the level of photo-realism

that can be achieved when rendering images. While some aspects of surface interactions cannot necessarily be modeled accurately, the ability to easily manipulate geometry, lighting and reflectance properties make ray tracing software a desirable simulation tool for these investigations.

Figure 7 Ray traced image of glass objects [29].

3 Research context and motivation

While DIC is predominantly used in laboratory conditions, there has been some previous work aimed at facilitating future use of the method in industrial applications. A selection of this research is presented briefly here. Much of this has been focused on structural health monitoring of bridges. While this is just one of countless possible applications of DIC, many of the challenges faced are similar to those that could be expected in other industrial environments.

In 2007, Yoneyama et al. [30] used 2D DIC to measure deflections of a steel girder bridge loaded by a truck, stationed at various positions along its length. They compared their results with conventional measurements made using transducers. Temporary speckle patterns were applied to some parts of the bridge using magnets, while other sections were left blank to investigate whether surface patterns were essential in that application. Their DIC system used conventional equipment, however the tests were performed at night under artificial illumination, and no mention was made of other environmental conditions such as wind speed. The investigators found that under these conditions, DIC with an applied pattern showed close agreement with transducer measurements. Data recorded without patterns was significantly noisier, and failed in some local regions. However, the investigators still claimed that patternless DIC presented a viable alternative to transducer measurements.

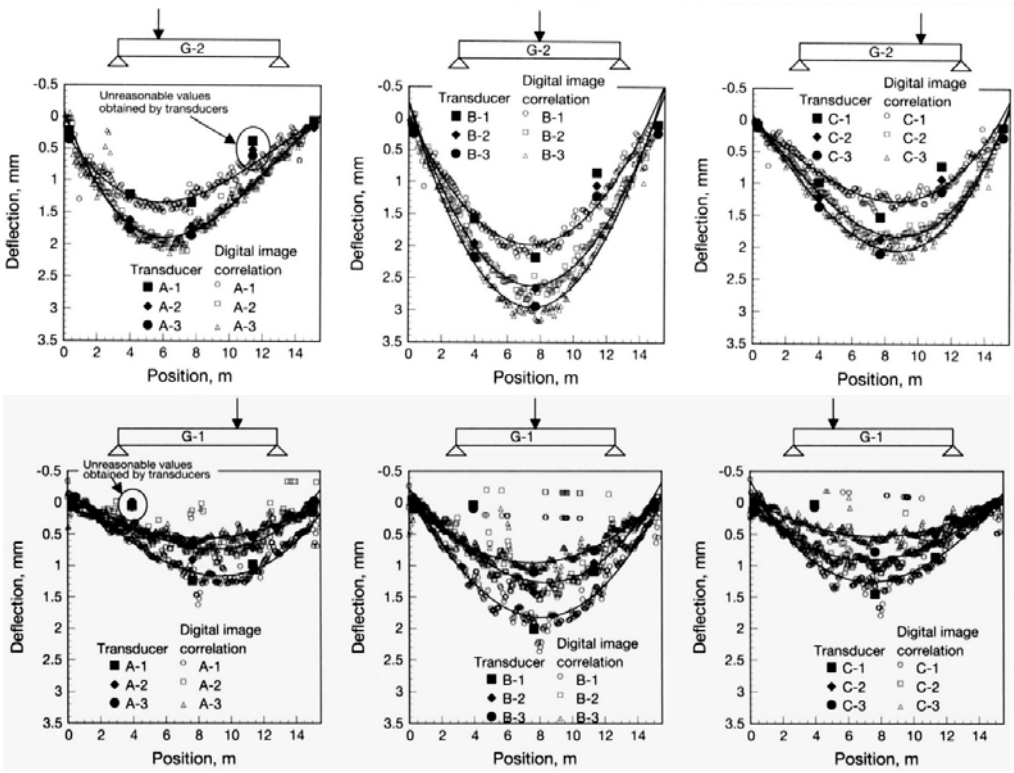

Figure 8 Comparison of 2D DIC and transducer measurements of bridge girder deflections presented by Yoneyama et al. [30]. Girder G-2 had a speckle pattern applied and girder G-1 did not.

In 2010, Kujawinska et al. [31] presented a multi-sensor system, utilizing both 2D and 3D DIC for online measurement of civil structures. While the system also incorporated other sensor technologies, it demonstrated that DIC could be utilized to monitor a variety of structures, including gathering and archiving valuable data remotely.

Peddle et al. [32] conducted further investigations into the feasibility of both 2D and 3D DIC for monitoring bridges. They too performed field tests that compared results with conventional transducer measurements. Their method used a chalk speckle pattern, which offers the benefit that it can be easily applied and removed after use. The authors reported that DIC was a viable alternative to conventional methods that offered potential improvement in both time and cost. However, they acknowledged some limitations, which included resolution limits, and questioned the suitability of the method in adverse weather conditions.

In 2012, Pan et al. [3] made modifications to conventional hardware in a 3D DIC measurement system that facilitated use in high-temperature, non-controlled environments. This comprised fitting an optical band-pass filter before the imaging lenses, and illuminating the measured object with monochromatic light. The filter made the system insensitive to variations in ambient light. This is noteworthy, since sensitivity to variable illumination could be a significant limitation to the performance of DIC in some industrial applications. Their test case in an extreme high-temperature environment was particularly challenging, due to the additional influence of thermal radiation, however they were still able to capture high quality images with constant contrast, suitable for DIC. Their system also offers benefits in semi-controlled environments, as even in experiments with artificial illumination, there is typically noise present from natural light sources.

Yoneyama and Ueda [33] showed that 2D DIC can be used for structural health monitoring of structures in outdoor environments, even when cameras are disturbed by wind or other non-ideal conditions. They performed laboratory measurements and analyzed the deformation of a real bridge, in conditions where the camera orientation was known to be affected by wind. Their method involved using non-deforming features in the scene to determine the unknown coefficients of the perspective transformation of the camera. Inverse transformations were then used to correct the measurements.

In 2013, Malesa et al. [4] used 3D DIC to measure displacements and strains of steel struts caused by temperature changes in an outdoor environment. They also studied displacements on a section of pipeline caused by flowing water. They achieved higher accuracy than that of common geodetic surveying methods, without the use of optical filters. However, modifications to the typical DIC method were required. These included additional hardware to protect cameras against environmental conditions, and development of new software methods for merging data distributed over long timescales.

Further investigations into the practicality of using 2D DIC for bridge deflection measurements were reported by Pan et al. [34]. They designed a “video deflectometer” that offered some significant advancements over those previously tested. Firstly, their system utilized an off-axis image configuration, allowing measurements to be taken when the camera axis was not perpendicular to the bridge. This removes some of the limitations on camera positioning and facilitates taking measurements from riverbanks or other easy to access locations. Their algorithms were also able to track the motion of existing features on the bridge without the addition of targets or surface patterns, thus eliminating the need for accessing difficult places on the bridge and surrounds. The authors claimed that the combination of these features made their method significantly easier to implement than other contact and non-contact techniques. Finally, their system had the additional benefit that it could take measurements in real time. Despite these advancements, the investigators acknowledged some significant limitations. Their field tests were noisy compared

with transducer measurements, and they noted that environmental conditions such as wind and temperature variation have the potential to disturb cameras. As part of their conclusion, the authors suggested that further investigations were needed to characterize and suppress or eliminate these problems.

Recently, Feng and Feng [35] have investigated the suitability of non-contact vision methods for use in structural health monitoring, which included utilizing 2D DIC for measuring vibrations of the Manhattan bridge during train crossings. They found that the technique showed significant potential as a low-cost alternative to conventional analysis with accelerometers. However, they also noted a required tradeoff between measurement resolution and field of view. Previously, the same group [36] investigated the robustness of some DIC algorithms in non-ideal environmental conditions. This included tests under low and variable light, background disturbance and partial template occlusion. They found that gradient based correlation methods, which are independent of total light intensity, were necessary to deal with the variable light conditions.

The research presented in this section outlines some of the challenges faced when implementing DIC in uncontrolled environments, and gives insight into possible solutions to some of those problems. The investigations conducted in this thesis directly address some of the knowledge gaps identified by researchers in the field as described above. This work is predominantly focused on the type of errors that occur when one of the cameras in a stereo system undergoes movement. The intention is that by characterizing these errors, it may be possible to first identify when a system needs to be recalibrated, and secondly to compensate for those errors when taking measurements from affected images. While Yoneyama and Ueda [33] addressed a similar problem, their investigation was limited to 2D DIC measurements with known stationary points in the scene. The work presented here is specific to 3D systems, and makes no assumption that stationary objects can be identified.

The errors resulting from varying light conditions are also investigated in this thesis. The band-pass filtering method presented by Pan et al. [3] provides one solution to this problem, however, it requires the additional hardware expense of optical filters and monochromatic lighting. Therefore, there is potential benefit in determining whether lighting induced errors can be compensated for retrospectively using a software based approach.

4 Experimental investigations

4.1 General method

These investigations examined DIC measurement errors that could occur in uncontrolled environmental conditions, by considering possible changes to the exterior camera calibration parameters, as well as other phenomena that might affect the quality of captured images. This primarily involved studying the resultant errors when one of the cameras in a stereo image system was moved. Experiments were also performed to investigate the effects of cameras becoming out of focus, and the impact of variable light conditions.

These experiments were performed using the following process:

1. Animations were made through two camera views of a simulated stationary surface using ray tracing software. In each animation, one of the calibration or environmental parameters was systematically varied.
2. These image sequences were processed using DIC software to obtain the apparent resultant displacement fields on the simulated surface.
3. Transformations and surface strains of the simulated object were calculated from the displacement field.

In each case, the aim was to identify distinguishing characteristics of the transformation and resultant displacement and strain fields that could potentially be used to identify and compensate for the effects of that error source.

4.2 Simulations using ray tracing software

The primary experimental task presented in this thesis is the modeling of varying camera and environmental parameters that could occur while capturing images with a typical DIC measurement system. These simulations were performed with Blender, a commonly used open-source 3D computer graphics program.

Simple scenes were created in Blender with the surface of interest placed in the x-y plane and centered at the origin. Two cameras were positioned at a distance of approximately half a meter from the object. An example scene is shown in figure *9*. The cameras were placed 40cm apart and each angled toward the center of the plate, 10° from perpendicular to the surface. In practice, DIC is used in a wide variety of applications at both very small and very large scales, so the simulated setup cannot be considered representative of all measurement systems. However, it is approximately typical of a system used for medium scale mechanical testing in laboratory conditions.

As Blender is designed for computer graphics animation, it allows for motion control of objects, cameras and lighting within the scene. In the tests presented here, it was used to create short image sequences of a stationary object surface. This object was initially a flat plate. Later tests were performed on the curved surface of a cylinder to investigate the effects of surface angle and distance from the camera on resultant errors. In each test, camera calibration or lighting parameters were varied at a constant rate while the image sequence was produced.

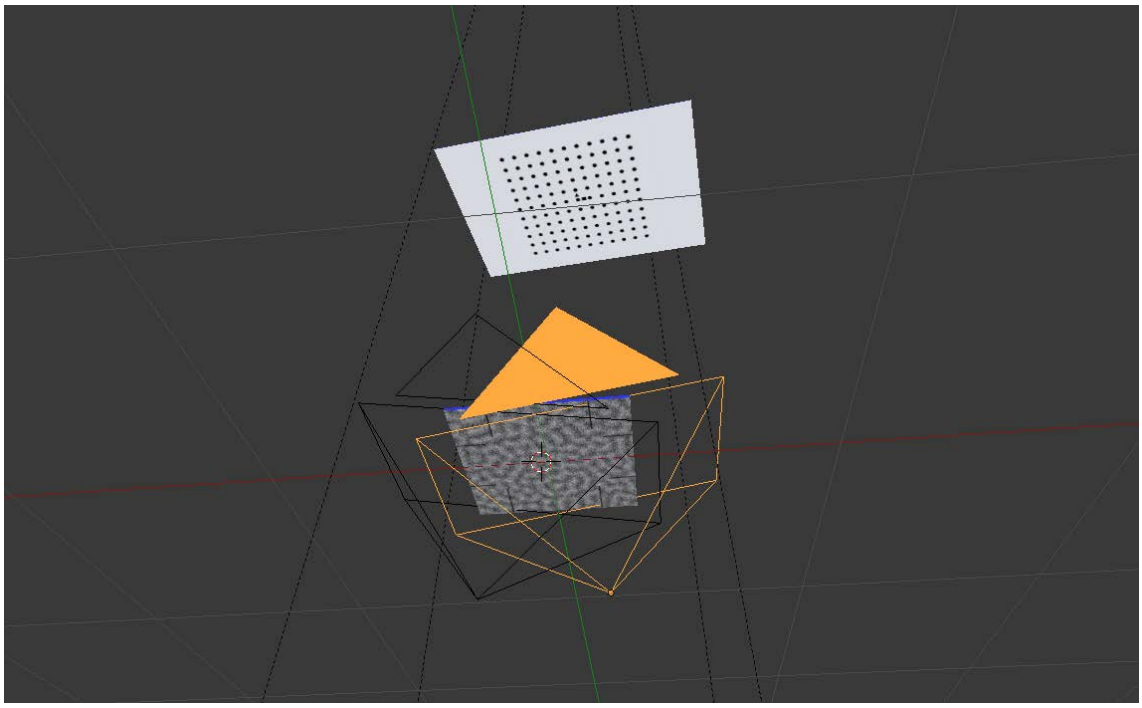

Figure 9 The experimental setup created as a scene in Blender. Two cameras in the foreground view the plate, which has a speckle pattern texture applied. The grid used for calibration is shown in the background. Lighting is provided by a diffuse large area light source positioned behind the cameras.

4.2.1 Calibration and scale validation test

Before conducting experiments, it was necessary to produce a sequence of DIC calibration images. A custom calibration grid template was created using the calibration tools in LaVision DaVis. This grid was applied as a texture to a plate in Blender, as seen in figure *9*. A diffuse bidirectional scattering distribution function (BSDF) material reflectance was used, as specular reflections are generally undesirable for DIC. Illumination was simulated as a large area diffuse light source positioned behind the cameras, providing consistent brightness and contrast across the entire object surface. The plate was initially placed in the x - y plane with its center at the origin, then moved to three alternate locations in the field of view with varying poses.

Next, a simple validation test was performed to assess the suitability of Blender as a simulation tool and its compatibility with DIC software. This involved taking two images of a plate, with the dimensions increasing uniformly by 5% between frames. To make the image sequence suitable for DIC measurements, an optimized speckle pattern as described in section 2.6 was applied to the plate as a texture. The plate dimensions and camera parameters used in the experiment are shown in Appendix 1, table *A1.1* .

4.2.2 Camera motion simulations

Camera motion is the primary area of investigation presented in this work. Simulated image sequences were created using Blender with the same initial setup as used for the scale validation test shown in table *A1.1* The effects of translating the camera in the x, y and z directions as well as rotating about the x, y and z axes were investigated individually. In all cases, the right-hand camera was kept stationary while the left-hand camera

was assigned a constant motion between frames. For translations, the camera was moved at a velocity of 1mm/frame, while rotation tests were performed at a rate of 1°/frame.

4.2.3 Camera de-focus simulations

The effect of a camera becoming out of focus during measurements was tested by producing image sequences where the point of focus in the left-hand camera was varied in 1cm increments. This was achieved by creating an invisible object in Blender, and setting the camera to auto-focus on that object. It was then moved towards or away from the camera along the *z*-axis. To emphasize the effects of changing focus, a particularly low f-stop value of 1.8 was used to reduce the depth of field. The remainder of the simulation settings were the same as those used for the validation and motion tests.

4.2.4 Variable illumination simulations

Errors introduced by variable light were investigated by creating an image sequence where a bright spot was moved across the plate. This was performed by animating a spotlight object in Blender. To emphasize the impact of this light variation, the plate was given a glossy BSDF reflectance, such that all reflections off the surface were specular. This meant that the bright spot was only visible in one camera view at a time, depending on the rotation angle of the spotlight. The intensity of the spotlight was selected such that fine details on in the speckle pattern were not visible to the naked eye, as shown in figure *10*. Specific parameter values for this test can be seen in Appendix 1, table *A1.3*. Besides the lighting, all other simulation settings were the same as those used in the validation test and camera motion simulations.

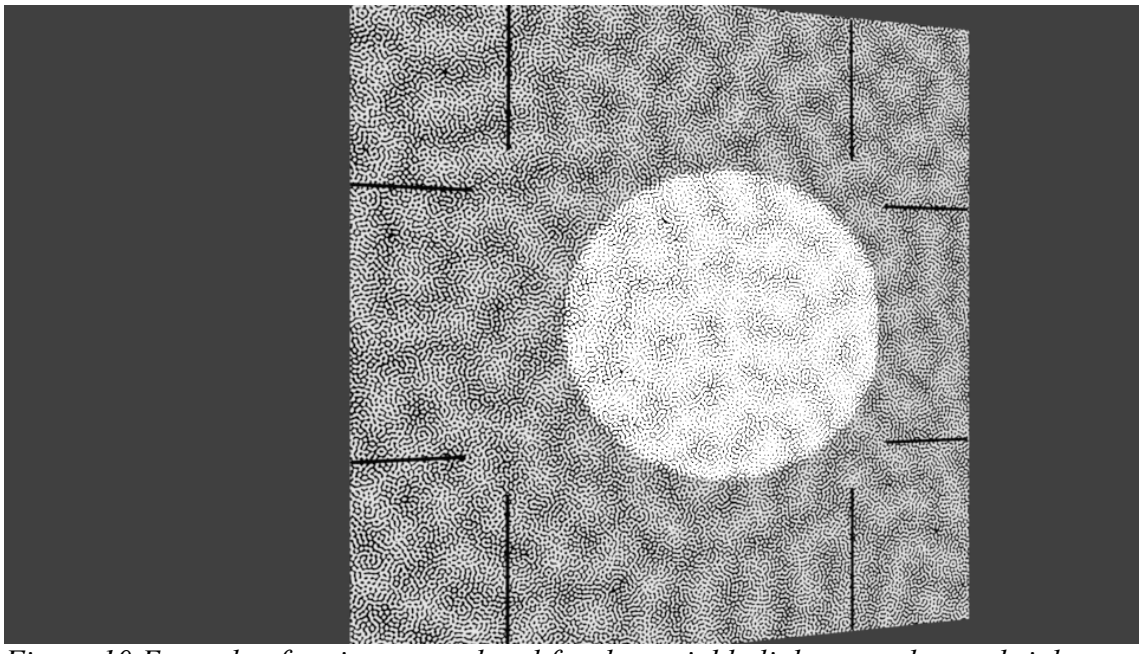

Figure 10 Example of an image rendered for the variable light test, where a bright spot was moved across the surface of the plate. The intensity of the spotlight was chosen such that fine details in the pattern were not visible to the naked eye.

4.3 Digital image correlation and results processing

DIC measurements were performed on the simulated image sequences described in section 4.2, using LaVision DaVis software with the StrainMaster plug-in. Calibration was performed using the grid pattern images described in section 4.2.1. While the calibration tools in DaVis can solve all the camera orientation parameters simultaneously, only the extrinsic parameters were fitted in these experiments. Once calibration was completed, the remaining image sequences were imported into DaVis, and processed using the StrainMaster plug-in to produce displacement fields.

Results were analyzed using Matlab. Strain tensor components were approximated from displacement fields using central finite differences in the x and y directions and the grid spacing of the displacement data. At a given grid location (n, n), these approximations can be expressed as:

$$\epsilon_{xx} = \frac{s_{n+1,n} - s_{n-1,n}}{2s_{x0}}$$

$$\epsilon_{yy} = \frac{s_{n,n+1} - s_{n,n-1}}{2s_{y0}} \qquad (14)$$

$$\gamma_{xy} = \frac{s_{n+1,n} - s_{n-1,n}}{2s_{y0}}$$

where $s_{i,j}$ is the displacement measurement of grid point (i, j) relative to the first frame, s_{x0} is the initial grid spacing in the x-direction, and s_{y0} is the original grid spacing in the y-direction.

Data was extracted from DaVis and divided into two-dimensional matrices, each of which contained values of a particular displacement component for a given frame, at a two-dimensional array of grid points on the measured surface. An example of how this data was used to perform strain calculations is shown in figure *11*.

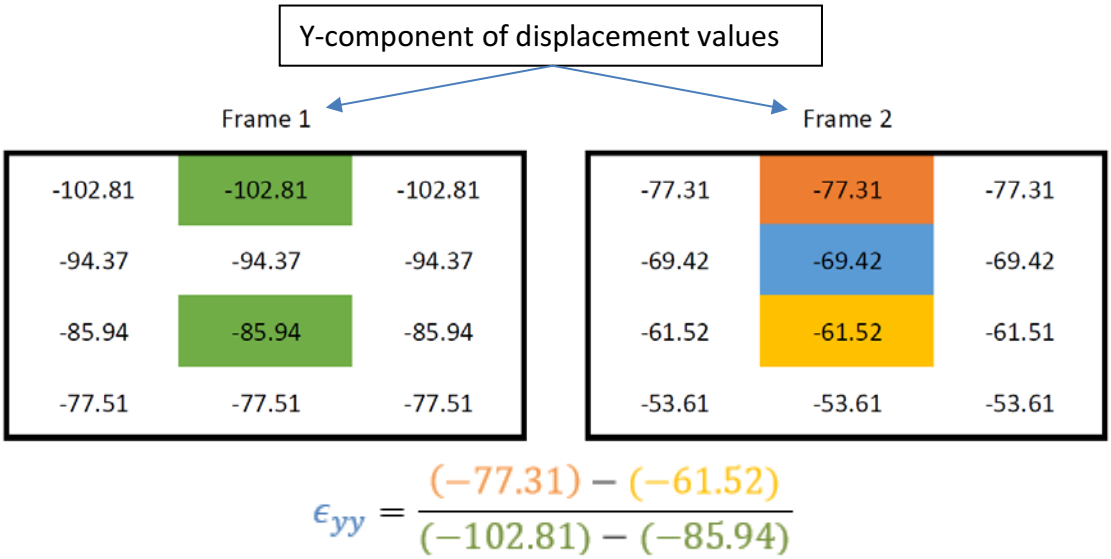

Figure 11 Example of how strain component ϵ_{yy} was calculated for frame 2 at the grid point indicated in blue.

5 Results and discussion

5.1 Scale test validation

The results of the scale test are shown in figure *12*. Homogeneous normal strains of approximately 5% and shear strain of 0% were measured. This matches the dimension increase that was applied in Blender, and validates the simulation method. Some discernable noise is visible, but the magnitude of these errors is relatively small.

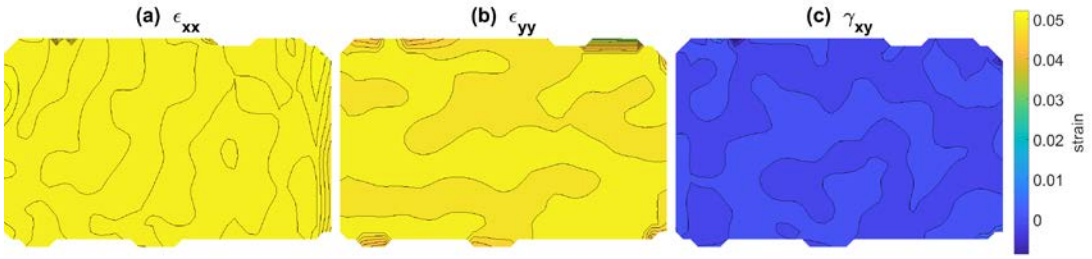

Figure 12 Measured strains on the simulated plate after the dimensions were increased by 5% in blender.

5.2 Camera translations

Translation of a single camera in a two-camera system in the x and z directions was found to produce significant measurement errors with clearly identifiable apparent plate motion and deformation characteristics. Translations along the y-axis produced small errors, however, the characteristics still appeared to be systematic and distinct.

5.2.1 Translations along x-axis

Errors resulting from positive x-axis camera translations (t_x) displayed distinct characteristics, both in terms of apparent displacement of the plate and apparent deformation. Displacements are presented in figure *13*, and show that the surface appears to move to the left in the negative x-direction. This is intuitive, since the left-hand camera was translated to the right. The plate is also observed to move in the z-direction. This too is anticipated, because the right-hand camera image remains unchanged. This creates a geometrical constraint, limiting possible translations of a given point on the plate to the pixel ray corresponding to that point in the right-hand camera. In most configurations, movement along such rays necessitates displacement in the z-direction. The red arrows in figure *13* indicate the location and pose of the two cameras. Here we can see that the camera axis is orientated such that a plate translation in the negative x-direction must be accompanied by a translation in the negative z-direction.

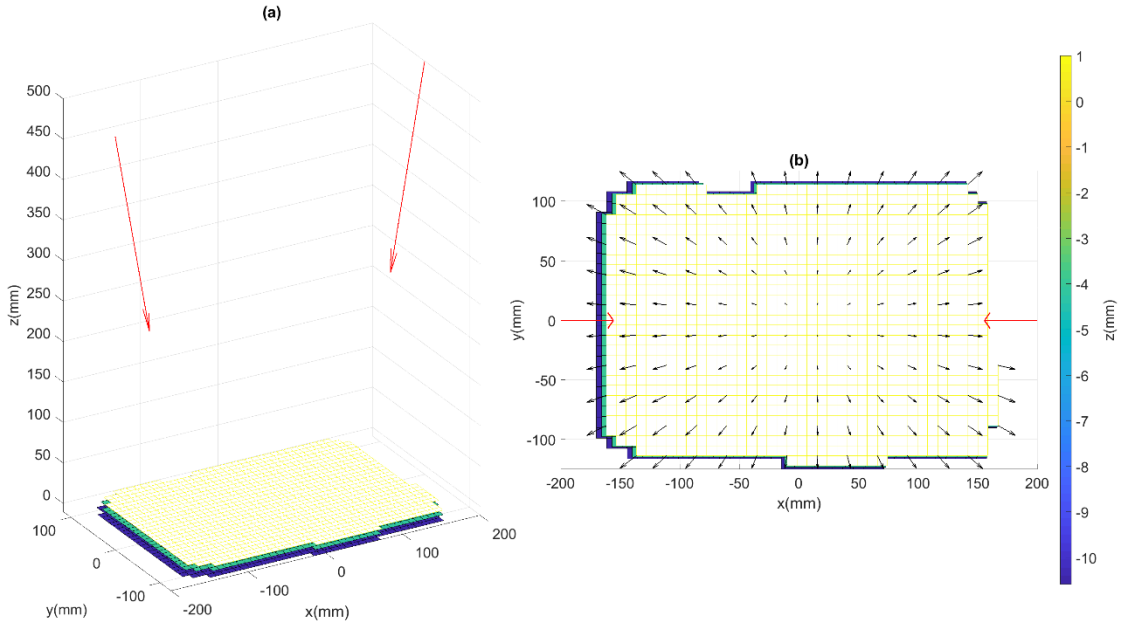

Figure 13 (a) Positions and poses of the cameras (red), plate position (yellow/white) and apparent measured plate position when the left camera is translated along the x-axis toward the right camera. Results are shown for translations of 4mm (green) and 9mm (purple). (b) The extent of apparent translations in x and y. Arrows on (b) give an indication of how the plate is observed to deform.

Translations along the x-axis also caused apparent deformation of the plate. Strain components for a 4mm and 9mm translation are shown in figure *14*. Normal strains were in the order of 2% for a 9mm translation, while there was no apparent shear strain. That is, the deformation appears to be characterized by near uniform expansion of the plate. As with the observed displacements, this is expected. The plate appears to move away from the right-hand camera, and as the view in that camera does not change, this is only possible if the plate expands. Noise in the apparent strain measurements is small, as seen by the contours in figure *14*.

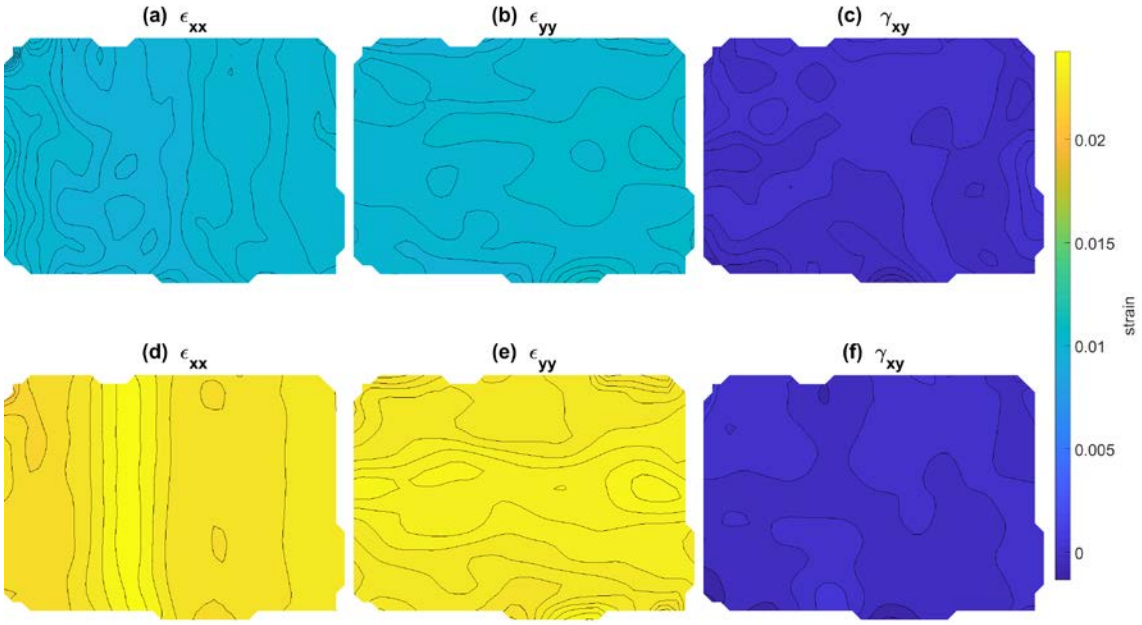

Figure 14 Apparent strains resulting from translating the left camera in the positive x-direction. (a), (b) and (c) show results for a 4mm translation and (d), (e) and (f) for a 9mm translation.

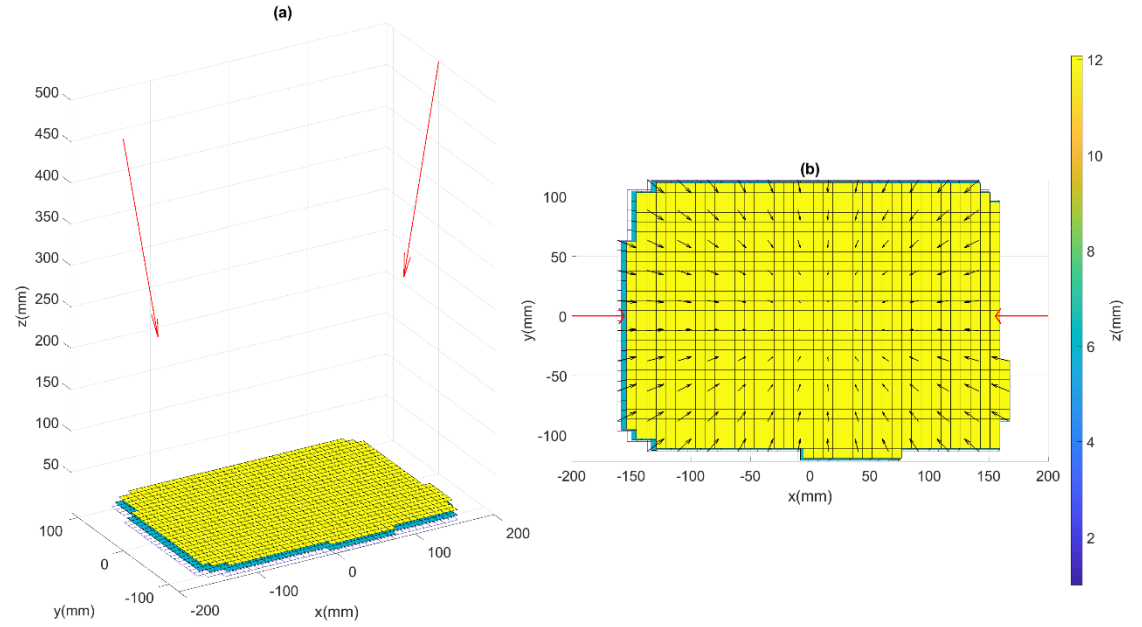

Figure 15 (a) Positions and poses of the cameras (red), plate position (white) and apparent measured plate position when the left camera is translated along the x-axis away from the right camera 5mm (turquoise) and 10mm (yellow). (b) The extent of apparent translations in x and y. Arrows on (b) give an indication of how the plate is observed to deform.

Figures *15* and *16* show the apparent translations and strains when the left-hand camera is moved in the negative x-direction, away from the right-hand camera. Here we can see that the plate appears to move in the positive x-direction and closer to the cameras in the z-direction. As expected, this behavior is the opposite of what was observed for camera translation in the positive x-direction. Similarly, the plate appears to undergo uniform contraction, rather than expansion.

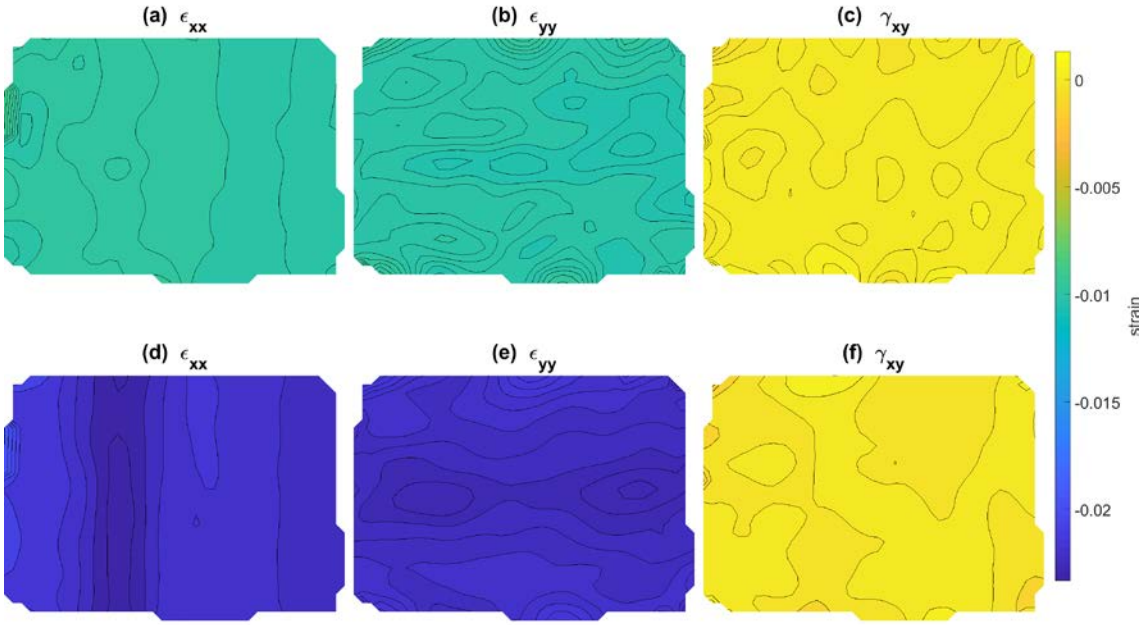

Figure 16 Apparent strains resulting from translating the left camera in the negative x-direction. (a), (b) and (c) show results for a 5mm translation and (d), (e) and (f) for a 10mm translation.

5.2.2 Translations along the y-axis

Figures *17* and *18* show the apparent displacements and strains resulting from positive y-axis camera transformations (t_y). Along this axis, direction can be considered arbitrary due to symmetry. These translations are observed to be characterized by an apparent shift of the plate in the opposite direction to the camera motion. This can be understood using the same reasoning as for t_x, described in section 5.2.1. As can be seen in figure *17*, the plate appears to buckle slightly, with one pair of diagonally opposite corners moving toward the cameras in the positive z-direction. The reason for this deformation is not immediately obvious, however it was observed for all y-axis camera transformations, so is believed to be systematic. The effect is small, with maximum observed displacement in the z-direction being approximately 1mm for a 9mm translation. Apparent strains are also observed to be very small, as seen in figure *18*.

It is interesting to note that t_y transformations violate the coplanarity constraint discussed in section 2.4. Therefore, resultant errors in the image matching process could have been expected. However, the small noise levels presented in figure *18* indicate that these do not occur.

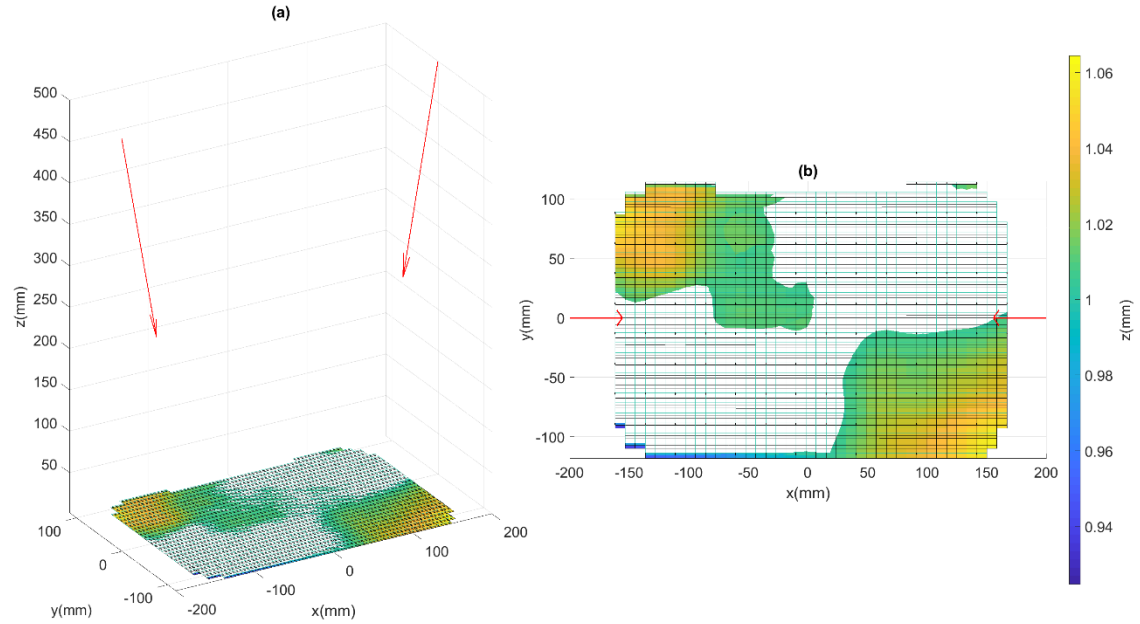

Figure 17 (a) Positions and poses of the cameras (red), plate position (white mesh) and apparent measured plate position when the left camera is translated 4mm and 9mm, upward in the positive y-direction. The observed displacements are very small, so cannot be seen in the figure. (b) The extent of apparent translations in x and y. The plate appears to shift downward along the y-axis, with the magnitude indicated by spacing between grid lines. Displacement in the z-direction is indicated by the color bar.

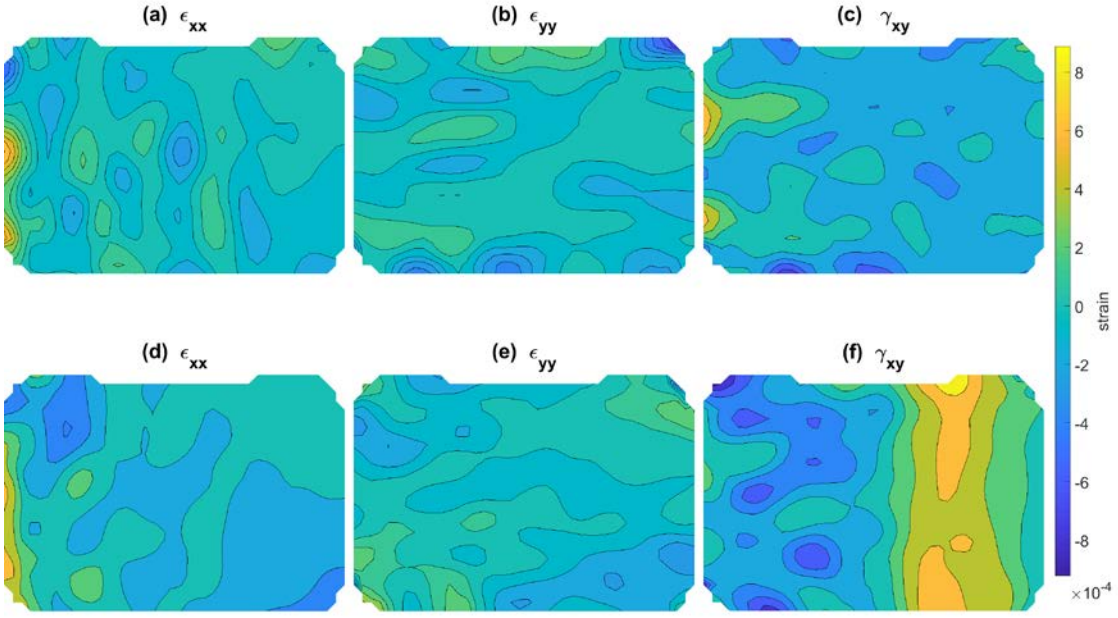

Figure 18 Apparent strains resulting from translating the left camera in the positive y-direction. (a), (b) and (c) show results for a 4mm translation and (d), (e) and (f) for a 9mm translation.

5.2.3 Translations along the z-axis

Translations along the z-axis (t_z) resulted in very little apparent rigid-body transformation of the plate, but with some significant buckling, as shown in figures *19* and *21*. Moving the left-hand camera 9mm toward the plate in the negative z-direction results in an apparent maximum z-displacement at the right-hand edge of the plate, toward the camera. The magnitude of this error is approximately the same as the camera translation. No significant z-axis displacement was recorded at the left edge of the plate, with the plate instead appearing to expand. In both cases, this is intuitive, as moving the camera closer to the plate makes it appear bigger. Since the DIC system assumes the camera is stationary, this can only be reconciled by either an apparent expansion of the plate or motion toward the camera.

It is noteworthy that the in-plane deformation and strain fields for t_z displayed distinct systematic errors when compared with other transformations. Figures *19*(b) and *21*(b) show regions of expansion and contraction on opposite sides of the plate. Which side expands and which contracts is dependent on the direction of translation. In figures *20* and *22*, it can be seen that apparent strains also have a clearly recognizable pattern. ϵ_{xx} and ϵ_{yy} both vary in an approximately linear fashion in the x-direction across the plate. The direction of increasing or decreasing strain is dependent on whether the camera was translated in the positive or negative z-direction. ϵ_{xx} is observed to be approximately constant across the width of the plate in the x-direction, while ϵ_{yy} displays periodic behavior, with the number of oscillations increasing with the amount of camera translation.

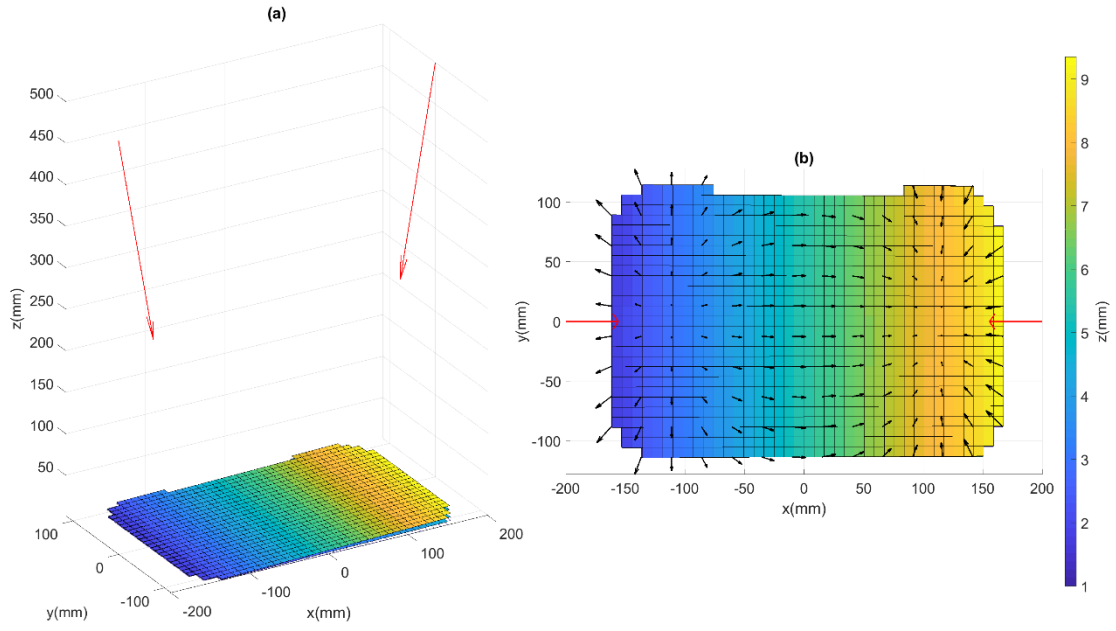

Figure 19 (a) Positions and poses of the cameras (red), plate position (white mesh) and apparent measured plate position when the left camera is translated 4mm and 9mm, forward in the negative z-direction. (b) The extent of apparent translations in x and y. Displacement in the z-direction is indicated by the color bar. Arrows on (b) give an indication of how the plate is deforming.

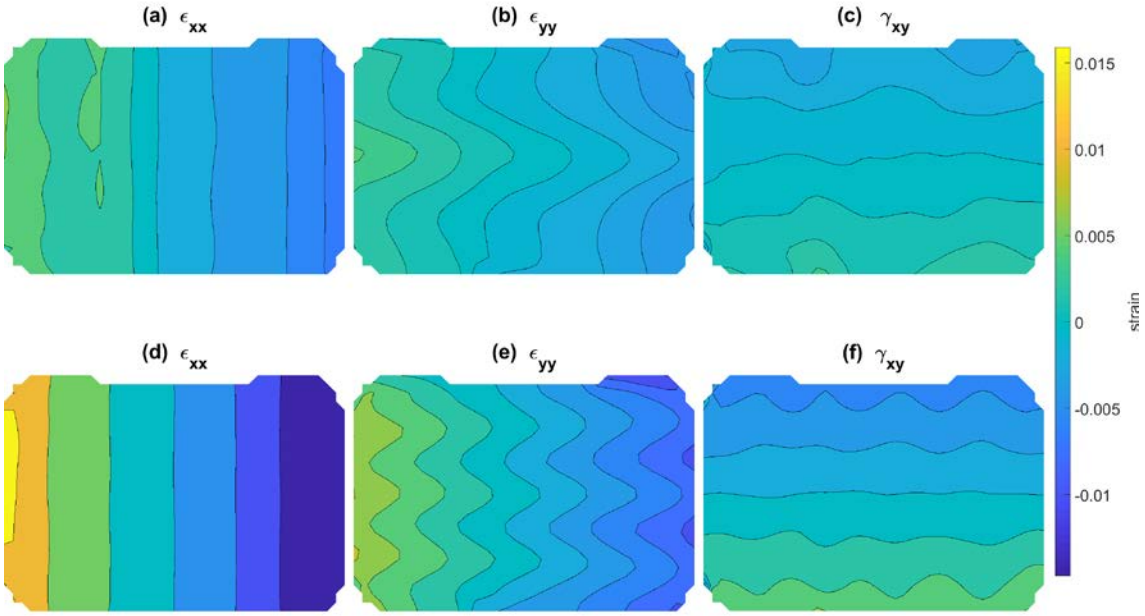

Figure 20 Apparent strains resulting from translating the left camera in the negative z-direction. (a), (b) and (c) show results for a 4mm translation and (d), (e) and (f) for a 9mm translation.

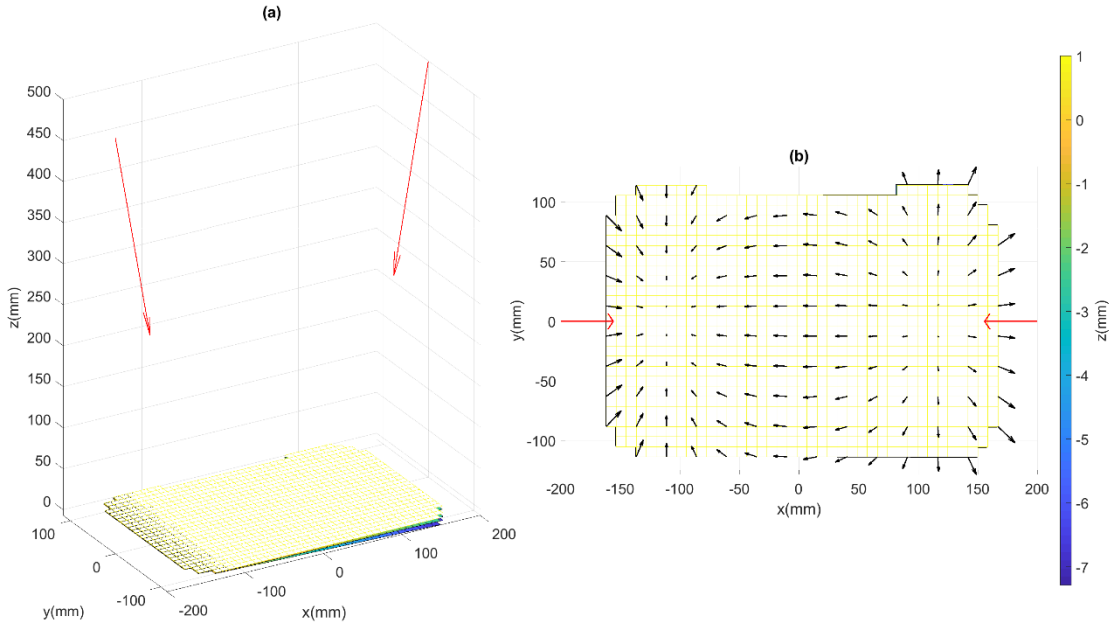

Figure 21 (a) Positions and poses of the cameras (red), plate position (white mesh) and apparent measured plate position when the left camera is translated 4mm and 9mm, forward in the negative z-direction. (b) The extent of apparent translation in x and y. Displacement in the z-direction is indicated by the color bar. Arrows on (b) give an indication of how the plate is deforming.

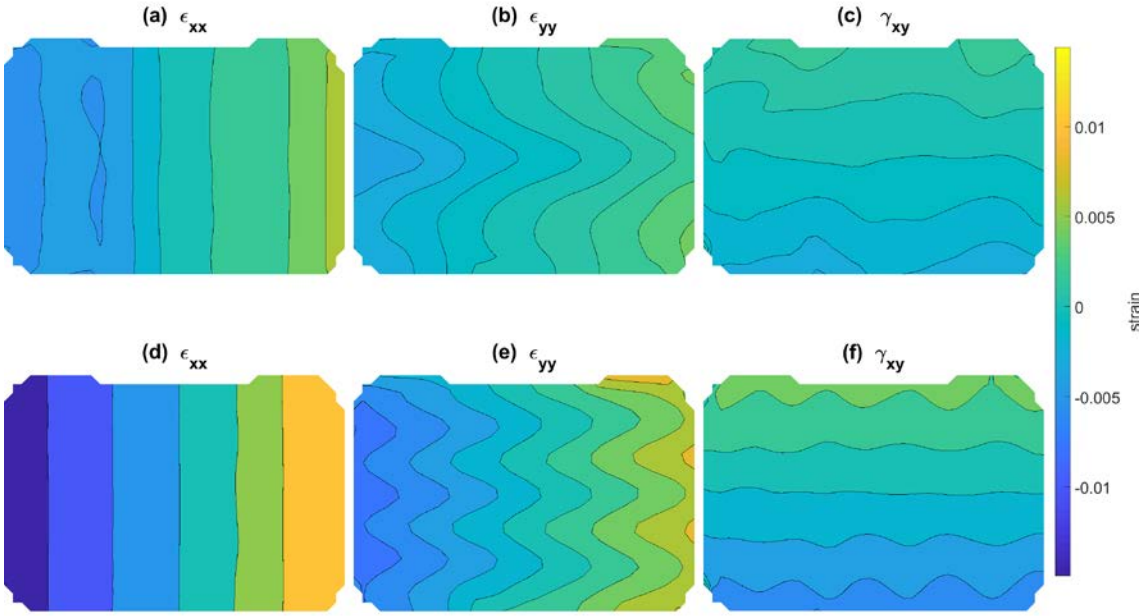

Figure 22 Apparent strains resulting from translating the left camera in the negative z-direction. (a), (b) and (c) show results for a 4mm translation and (d), (e) and (f) for a 9mm translation.

5.3 Camera rotations

The effects of camera rotations were found to be consistent with those observed for translations. However, errors were much larger for rotations.

5.3.1 Rotations about the x-axis

Of all the camera transformations investigated, rotations around the x-axis (R_x) were the only ones observed to cause image correlation failure within the range of motion tested. This was observed for rotations larger than 6°, with complete failure occurring for rotations larger than 7°. Errors resulting from these rotations were observed to consist of an apparent translation of the plate in the y-direction, accompanied by a distinct deformation pattern comprising significant buckling and out of plane displacement in regions of the plate.

Figure *23* shows the apparent translation of the plate in the y-direction for camera rotations of 3° and 6°. Significant distortion of the plate can also be seen, with the top left and bottom right corners appearing to move toward the cameras, while corners on the other diagonal appear to move away in the negative z-direction. Figure *24* further illustrates this, showing the extent of out of plane deformation and indicating the nature of in plane local displacements. Strain maps for 3° and 6° rotations are shown in figure *25*. They are characterized by regions of maximum positive strain at one set of diagonally opposite corners, and regions of maximum negative strain at the other corners.

These motion and deformation patterns closely resemble those observed for t_y, as presented in section 5.2.2. However, the observed transformations resulting from rotation are much larger. This is expected, because rotations about the x-axis cause a relatively large apparent y-direction shift through the view of the moving camera. By considering basic trigonometry it is evident that this shift, m_y, and the rotation angle, θ, can be related

by $m_y \approx D \times tan\theta$, where D is the distance between the camera and the plate. In view of this relationship, when a camera is placed very close to the plate, the effects of rotations could be less than the effects of translations. However, for any likely industrial DIC camera configurations, the effects of rotations should be much more significant.

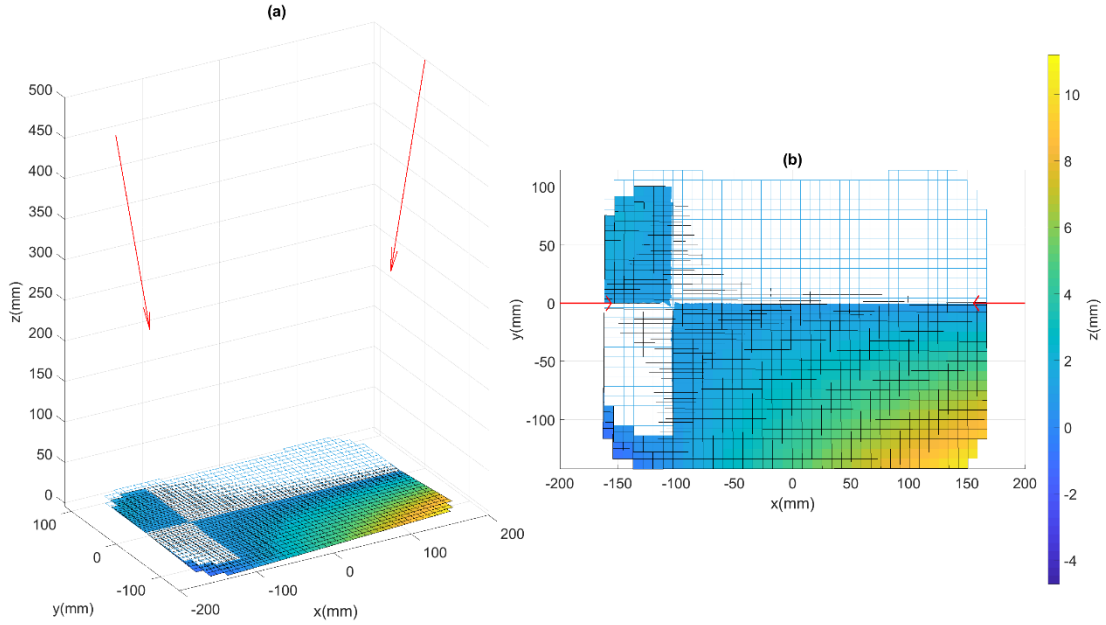

Figure 23 (a) Positions and poses of the cameras (red), plate position (white mesh) and apparent measured plate position when the left camera is rotated 3° and 6° upward about the x-axis. (b) The extent of apparent translations in x and y. Displacement in the z-direction is indicated by the color bar.

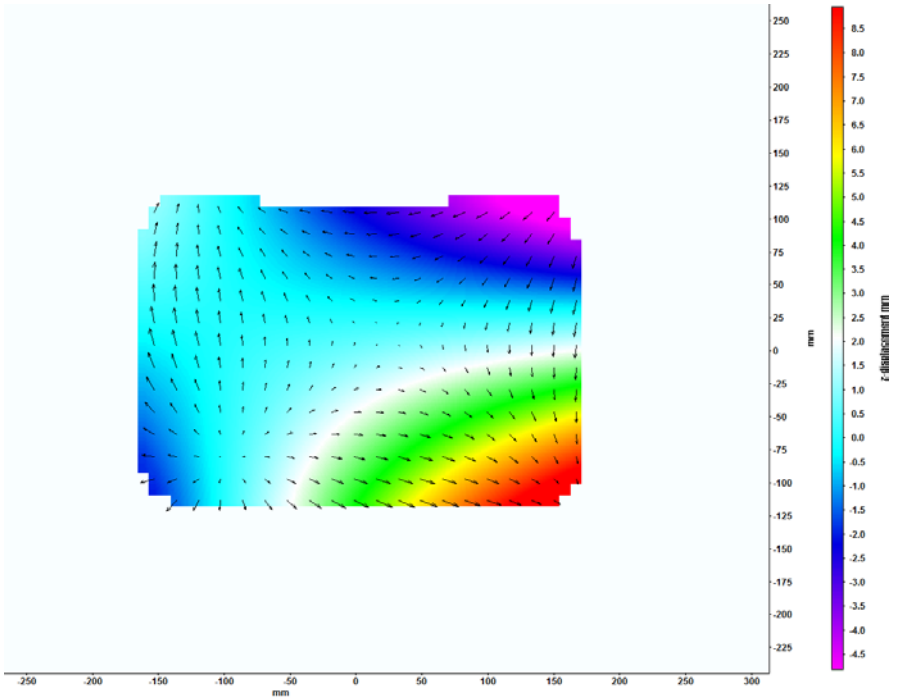

Figure 24 Indication of apparent plate deformation when the left camera is rotated 6° upward about the x-axis.

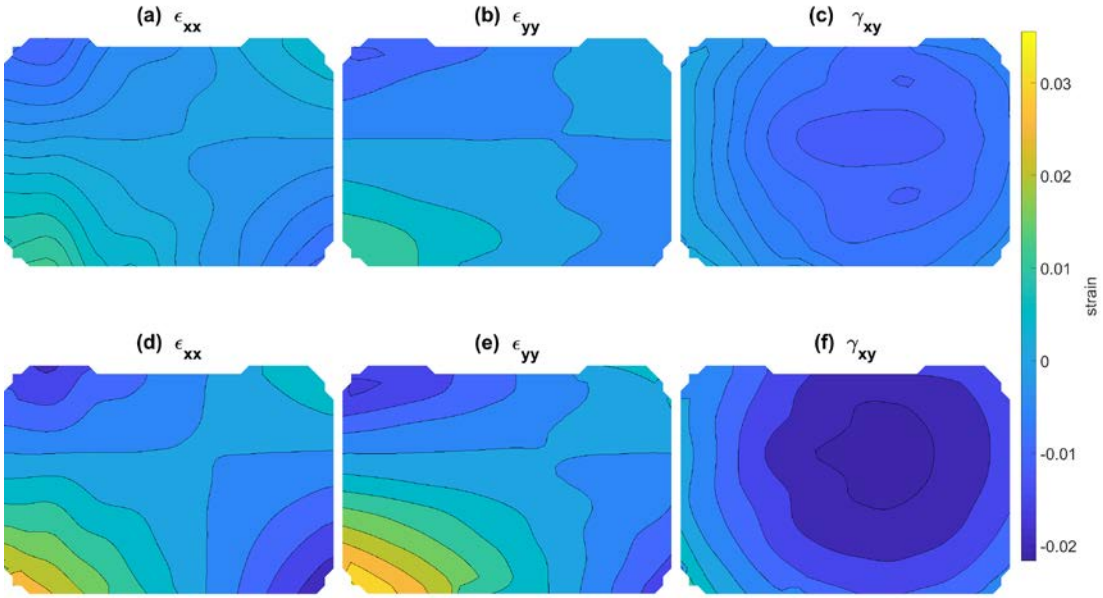

Figure 25 Apparent strains resulting from rotating the left camera upward about the x-axis. (a), (b) and (c) show results for a 3° rotation and (d), (e) and (f) for a 6° rotation.

5.3.2 Rotations about the y-axis

Camera rotations about the y-axis (R_y) were observed to result in large apparent plate transformations, including significant movement and deformation. These transformations had similar characteristics to those for t_x. This is intuitive, because R_y causes the plate to appear to move along the x-axis in the view of the left-hand (moving) camera.

Figures *26* and *27* show the results for rotations in the negative direction, and figures *28* and *29* show the results for the positive direction. Negative rotations are characterized by a significant shifting of the plate in the negative z-direction, away from the cameras, as well as a shift in the negative x-direction. These plate movements correspond to those observed for camera translations in the positive x-direction, and as discussed in section 5.2.1, they are expected to be observed in tandem due to the orientation of the stationary right-hand camera. That is, translations in the negative x-direction correspond to movements further into the background in the right-hand camera view.

The apparent motion of the plate was again observed to coincide with expansion. As discussed previously, such deformation is necessary to compensate for the apparent movement in the negative z-direction and the unchanging scene in the right-hand camera. Both the translations and strains were observed to be much larger for R_y than for t_x. This is to be expected, since rotations create a greater apparent movement of the plate across the view of the moving camera than in the case of translations, as discussed in section 5.3.2.

As would be anticipated, rotating the camera in the positive direction about the y-axis had the opposite effect to that of negative rotations. That is, the plate was observed to move toward the right-hand camera in the positive x and z directions. The same applied for strains, with the plate undergoing contraction instead of expansion.

In addition to the general direction of plate translations and strains, some interesting deformation behavior was observed to result from R_y transformations. Firstly, there was significant apparent buckling of the plate, which can be clearly seen in figures *26*(a) and *28*(a). In both cases, the side of the plate closest to the stationary right-hand camera appears to move further than the opposite side. As discussed previously, movements in the z-direction must be accompanied by expansion or contraction, so predictable strain patterns were also observed, with variation in both ϵ_{xx} and ϵ_{yy} greatest on the side of the plate closest to the right-hand camera. Interesting characteristics were also observed for the shear strain, with regions of maximum strain occurring in diagonally opposite corners of the plate, and regions of minimum strain occurring in opposite corners along the other diagonal.

The distinct deformations are believed to be associated with the change in viewing direction of the left-hand camera that occurs when it is rotated. This is supported by the fact that these same patterns were not observed for t_x. It is commonly known that observing a rectangular surface from an angle creates a distorted image, as one end of the surface is further from the camera than the other, and thus appears smaller. Rotating the camera changes this viewing angle, and therefore also changes the extent of this distortion. As expected, it is the edge of the plate furthest from the left-hand camera that appears to undergo the greatest deformation.

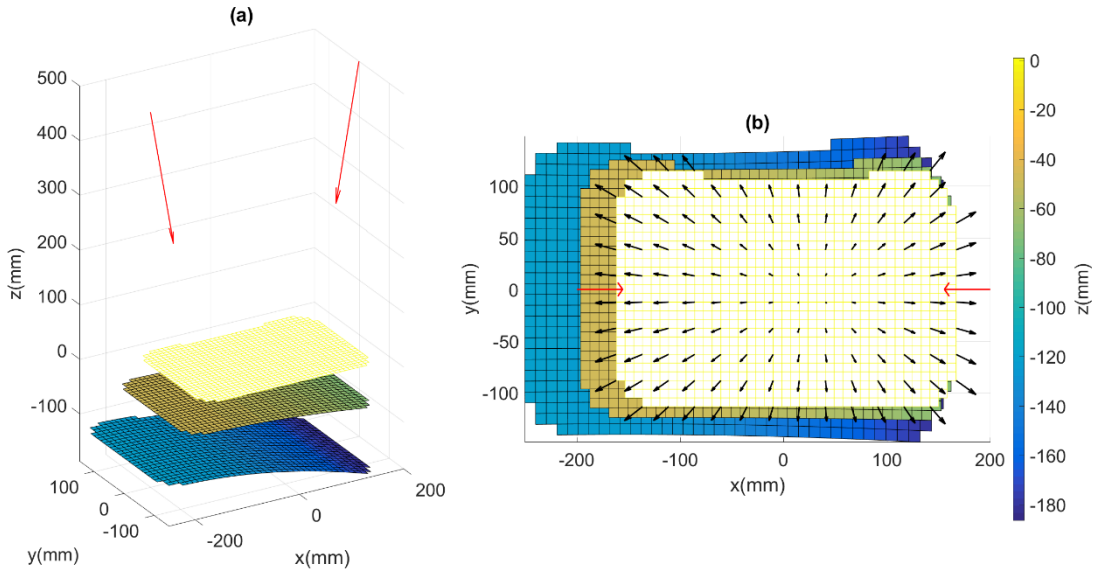

Figure 26 (a) Positions and poses of the cameras (red), plate position (yellow mesh) and apparent measured plate position and deformation when the left camera is rotated -4° and -9° about the y-axis. (b) The extent of apparent plate movement in x and y. Displacement in the z-direction is indicated by the color bar. Arrows on (b) give an indication of how the plate is deforming.

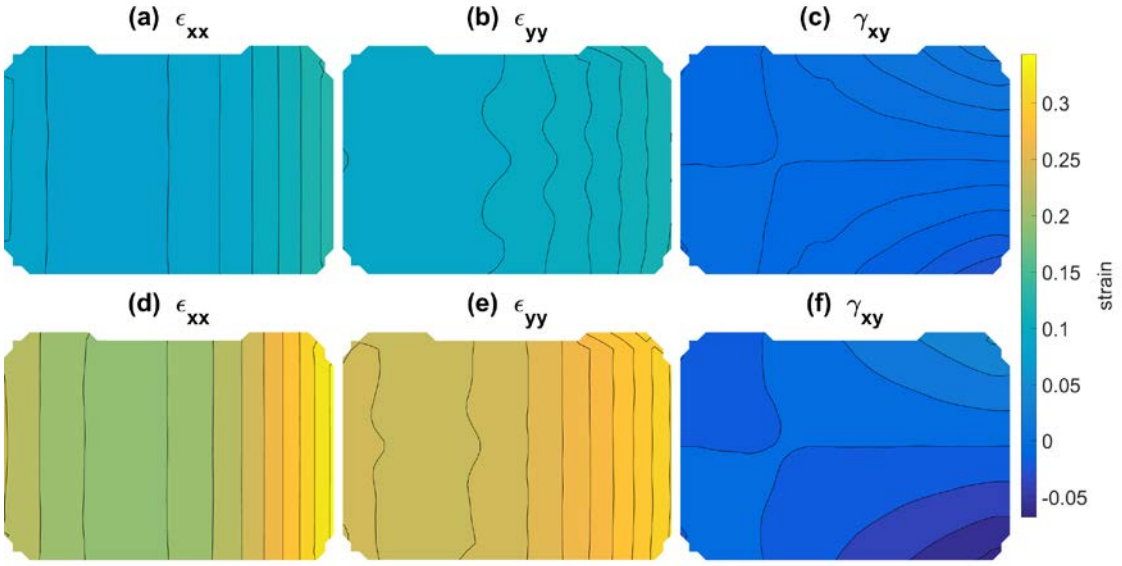

Figure 27 Apparent strains resulting from rotating the left camera about the y-axis in the negative direction. (a), (b) and (c) show results for a -4° rotation and (d), (e) and (f) for a -9° rotation.

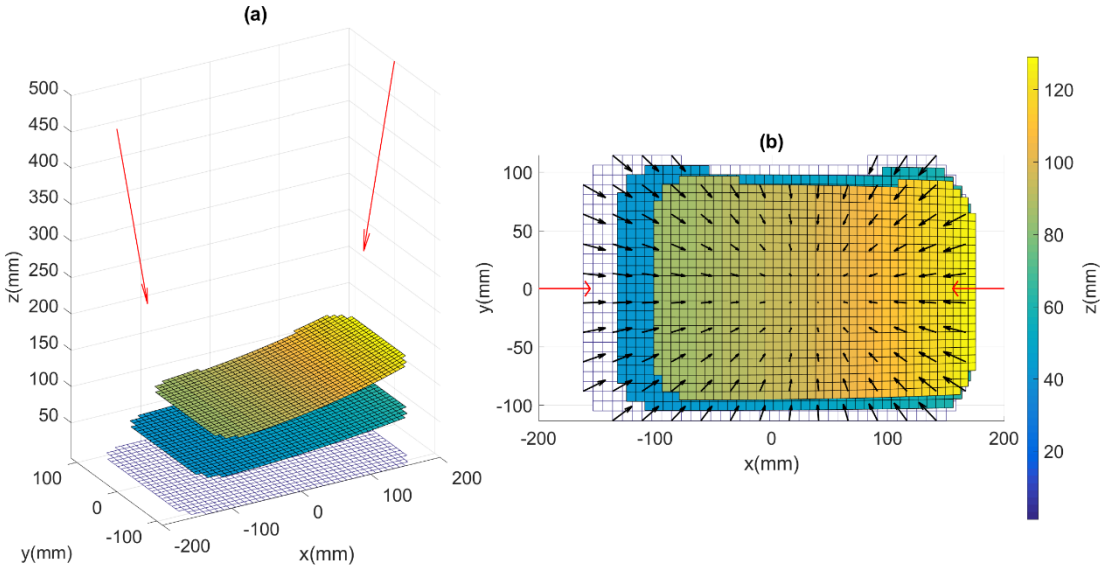

Figure 28 (a) Positions and poses of the cameras (red), plate position (white mesh) and apparent measured plate position and deformation when the left camera is rotated 4° and 9° about the y-axis. (b) The extent of apparent plate movement in x and y. Displacement in the z-direction is indicated by the color bar. Arrows on (b) give an indication of how the plate is deforming.

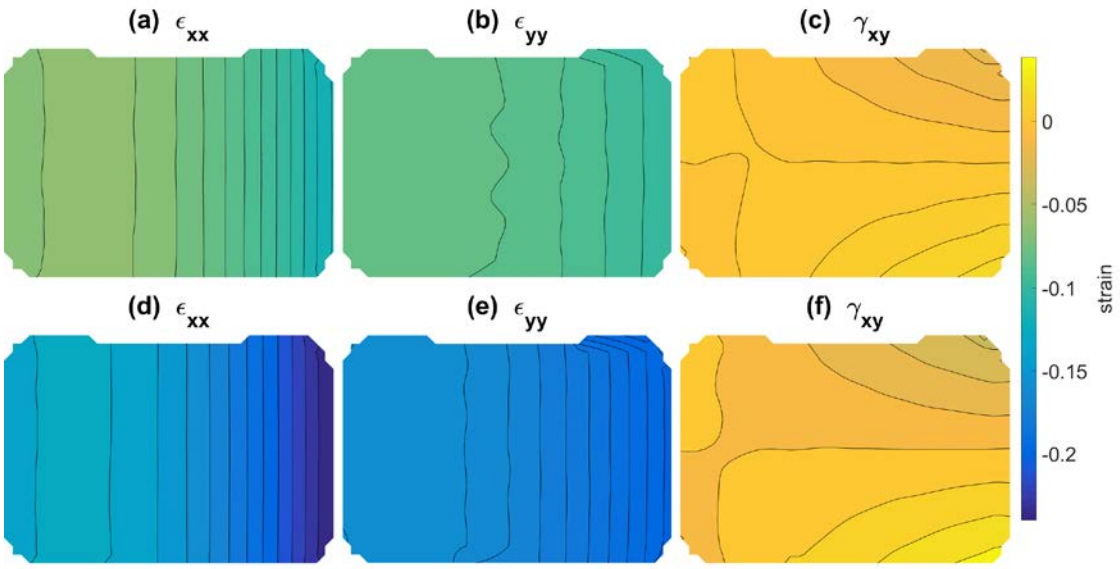

Figure 29 Apparent strains resulting from rotating the left camera about the y-axis in the negative direction. (a), (b) and (c) show results for a 4° rotation and (d), (e) and (f) for a 9° rotation.

5.3.3 Rotations about the z-axis

Rotating a camera about the z-axis (R_z) was distinctly characterized by an apparent rotation of the plate around both the z-axis and x-axis, as can be clearly seen in figure *30*. The observed rotation around the z-axis is intuitive, as rotating a camera in this direction approximately coincides with rotating it around its own optical axis, which results in rotation of the camera view. The rotation around the x-axis can be understood by considering the t_x results, as discussed in section 5.2.1. Due to the observed z-axis rotation, the top of the plate appears to move in one direction along the x-axis, and the bottom of the plate appears to move in the opposite direction. The direction of z-axis camera rotation can be considered arbitrary. That is, changing the direction of rotation reverses the direction of observed plate transformations, but the effects are otherwise the same. For positive rotations, the top of the plate moves in the positive x-direction and the bottom moves in the negative direction. Since the direction of x-axis translation influences the direction of apparent movement along the z-axis, the top half of the plate appears to move toward the cameras along the z-axis, while the bottom half of the plate is observed to move away from the cameras.

Apparent normal strains resulting from R_z were characterized by variation from the top to the bottom of the plate for both ϵ_{xx} and ϵ_{yy}. Conversely, shear strains varied across the width of the plate from left to right. In all cases, strains were approximately zero at the center of the plate, positive in one half and negative in the other half. In the case of a positive z-axis rotation, normal strains were positive in the bottom half and shear strains were positive on the left side, which can be seen in figure *31*. As expected, the magnitude of the strains increases with rotation angle. Comparing figures *31* (a) and (b), we see that the direction of strain gradient is slightly different for a 6° rotation than for a 9° rotation. Comparison with other rotation angles suggests that this variation in gradient direction is systematic. This can be understood by considering that strain is expected to increase as surface distance from the camera increases, as explained in section 5.2.1. In figure *30* it

can be seen that due to the rotation of the plate around the z -axis, the direction of maximum variation in the plate's z-position changes with the rotation angle of the camera. Therefore, so too does the direction of normal strain gradient.

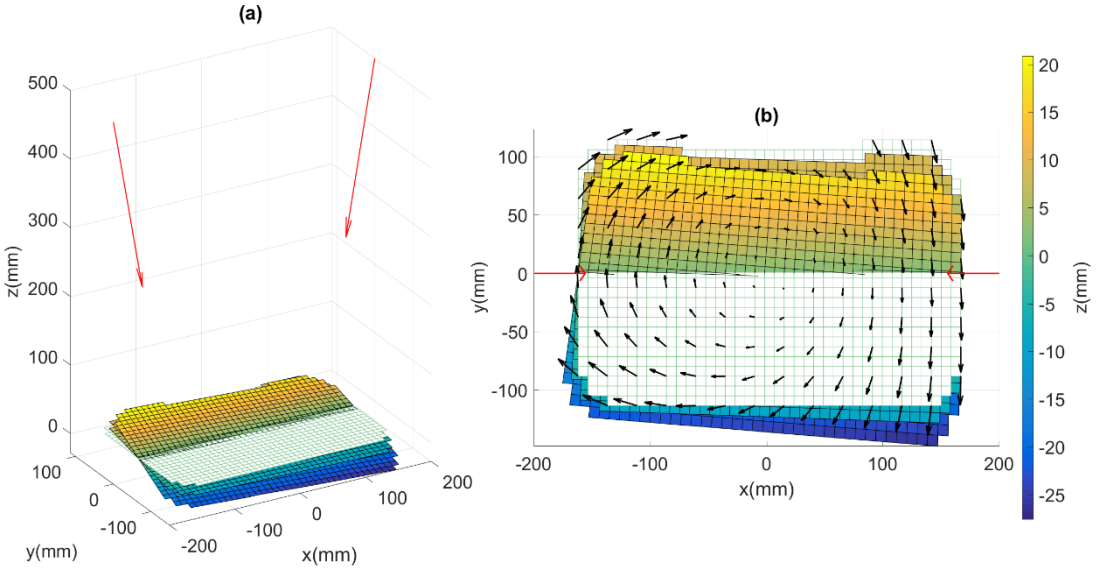

Figure 30 (a) Positions and poses of the cameras (red), plate position (white mesh) and apparent measured plate position and deformation when the left camera is rotated 4° and 9° about the z-axis. (b) The extent of apparent plate movement in x and y. Displacement in the z-direction is indicated by the color bar. Arrows on (b) give an indication of how the plate is deforming.

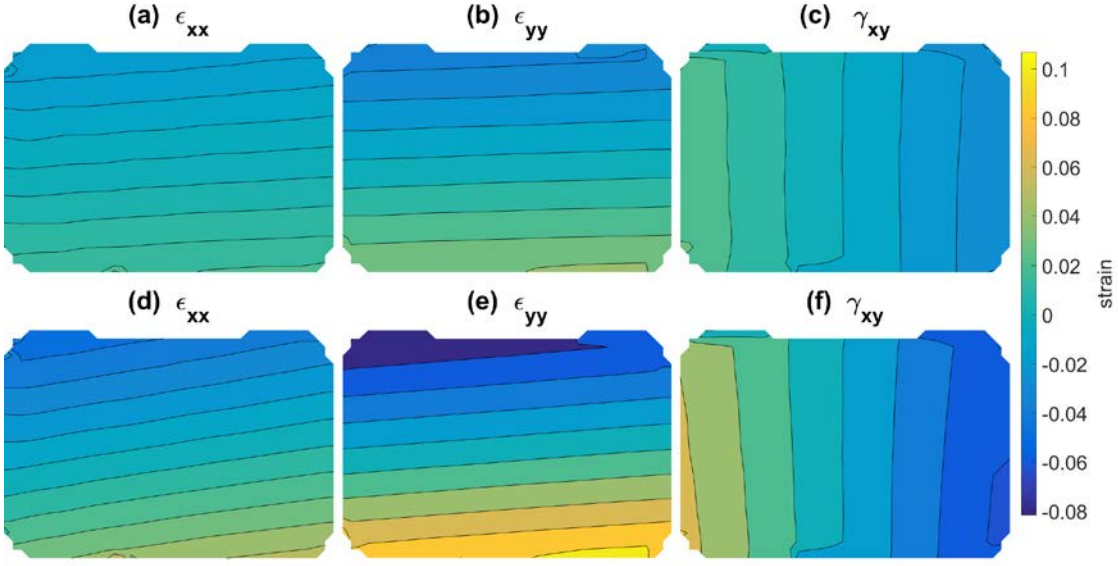

Figure 31 Apparent strains resulting from rotating the left camera about the z-axis in the positive direction. (a), (b) and (c) show results for a 4° rotation and (d), (e) and (f) for a 9° rotation.

5.4 Variable illumination

Changes in illumination were observed to introduce a small amount of noise to DIC measurements. Figure *32* shows the apparent strains that are detected when a bright spot is

moved across the surface of a reflective plate, such that it appears in only one camera view at any given time. As shown previously in figure *10*, the intensity level of the bright spot was such that the surface pattern appeared to be washed out, with some of the smaller features becoming difficult to distinguish with the naked eye.

The error introduced by a moving bright spot was significant, with strain values of approximately $\pm 1.5\%$. This noise appears to be random at a local level. However, average errors were observed to be higher in areas covered by the bright spot. This is evident in figure *32*, where strain maps (a), (b) and (c) show that error magnitudes are discernably larger on the right half of the plate, which was mostly covered by the bright spot. Maps (d), (e) and (f) were taken for a frame where the bright spot was centered in the image and covering most of the view. Here, errors of all magnitudes seem to be more evenly distributed across the plate.

The locally random nature of this noise makes it unlikely that this type of error could be identified or compensated for using measurement data alone. However, because the variation occurs on a local scale, in many applications it may be possible to mitigate the effects by filtering. Deciding when and how to apply such filtering should be feasible, given that errors of significant magnitude were only observed to occur when inconsistent illumination is obvious to the naked eye in the raw images. It may also be possible to sufficiently correct digital photographs using conventional image processing techniques prior to performing DIC measurements. The goal of such processing would be to produce images with the qualities that are generally desirable for DIC. That is, they should have high-contrast and approximately the same illumination between frames and images. However, one drawback of such processing is that it has the potential to introduce noise to images, which too could be expected to result in noisy DIC measurements [1,37].

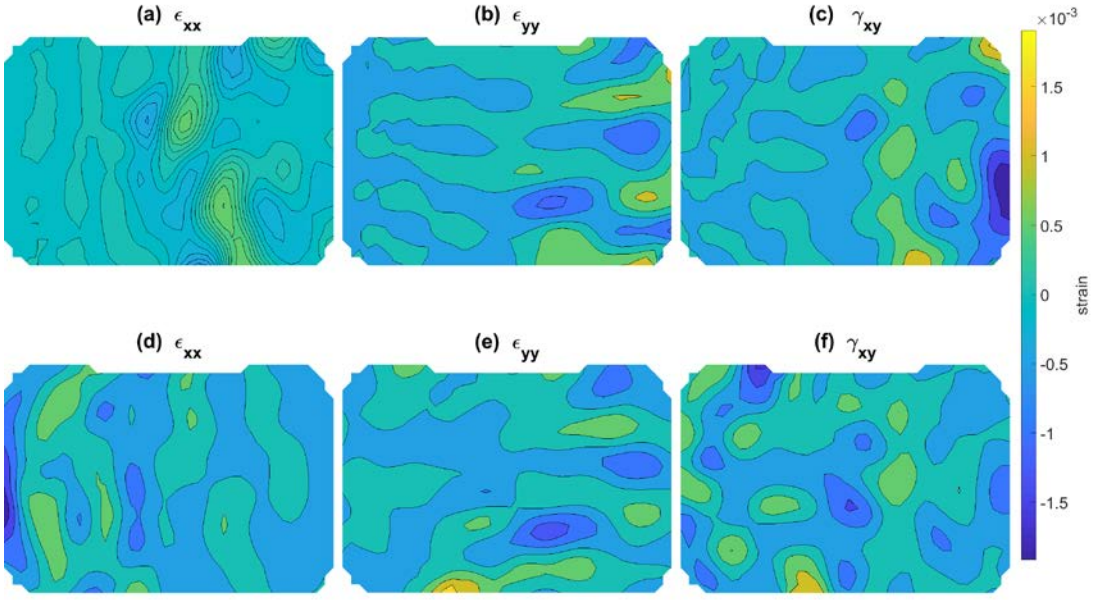

Figure 32 Apparent strains resulting when a bright spotlight illuminates a plate with glossy reflectance and is moved across the surface in the x-direction. (a), (b) and (c) show results when the bright spot appears to cover approximately half of the area of interest in one of the cameras, but does not appear in the other camera view. (d), (e) and (f) show strains when the bright spot is centered covering most of the view. Again, the bright spot cannot be seen in the other camera view.

5.5 Camera de-focus

Camera de-focus was observed to introduce random noise to DIC measurements, with the magnitude of error increasing as the image became more blurred. At a certain point, this blurring lead to correlation failure.

Figure *33* shows the apparent strains when the point of focus is moved in the negative *z*-direction, beyond the plate. The effects of moving the focus in the positive *z*-direction are shown in figure *34*. In both cases, it is evident that small adjustments in focus lead to small errors. These errors would most likely be difficult to distinguish from other noise sources in regular DIC measurements. However, they are also of a magnitude that may be acceptable in many industrial applications.

Correlation failure was observed to occur when the point of focus was moved beyond approximately 50cm in the negative direction, and 15cm in the positive direction. These represent approximately double and one third of the distance between the camera plate respectively. Maximum errors of over 3% were recorded for images where the focus was adjusted close to the point of causing correlation failure. It should be noted that levels of blur sufficient to cause large errors were easily detectable to the human eye. Examples of a sharp image and one where the plate is out of focus to this extent are presented in figures *35* and *36*.

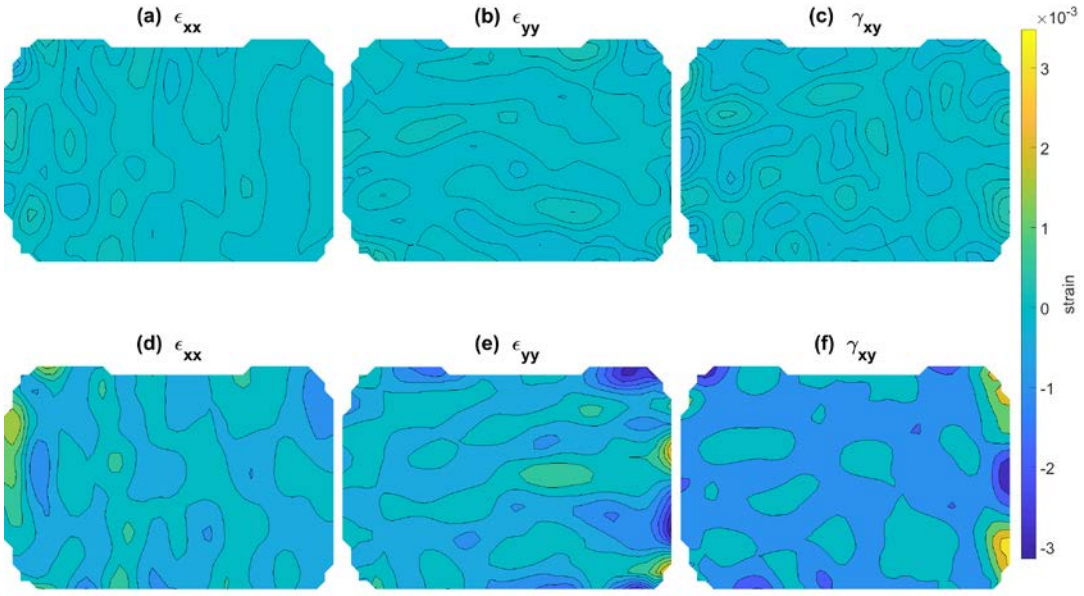

Figure 33 Apparent strains resulting when a camera's point of focus is moved into the foreground in the positive z-direction. (a), (b) and (c) show results when the point of focus is 9cm in front of the plate. (d), (e) and (f) show strains when the point of focus is 16cm in front of the plate.

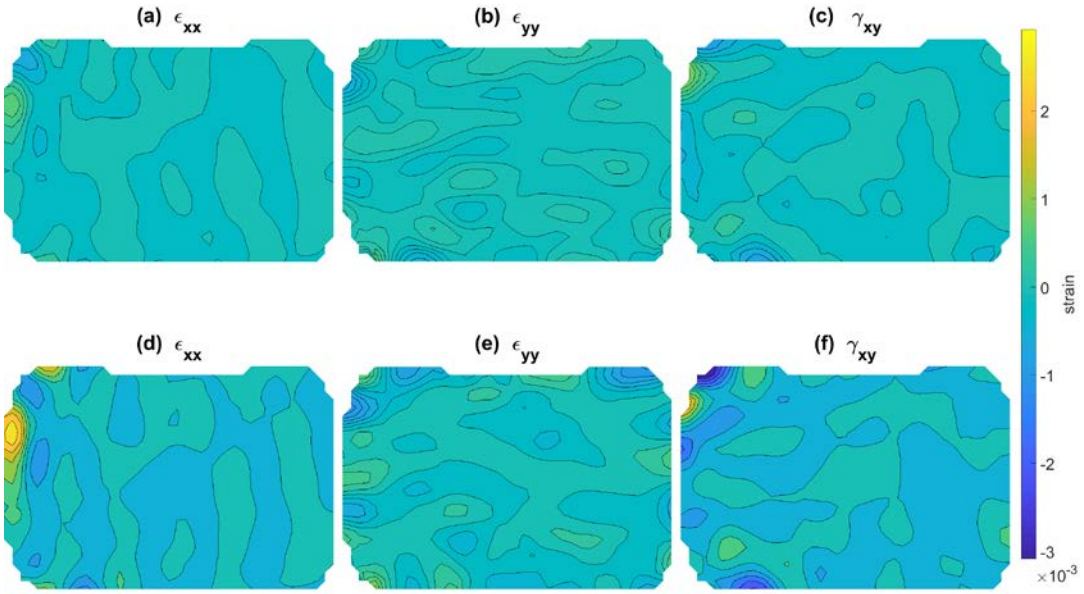

Figure 34 Apparent strains resulting when a camera's point of focus is moved into the background in the negative z-direction. (a), (b) and (c) show results when the point of focus is 15cm in behind the plate. (d), (e) and (f) show strains when the point of focus is 30cm behind the plate.

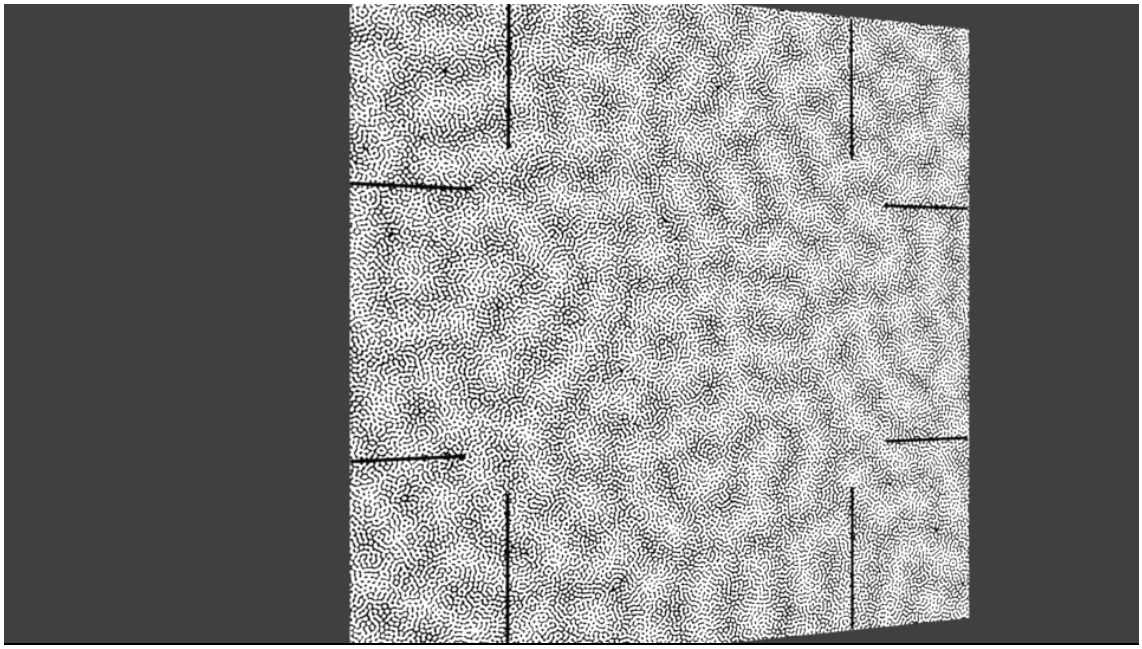

Figure 35 Image quality when the left-hand camera is focused on the plate. The speckle pattern appears sharp to the naked eye.

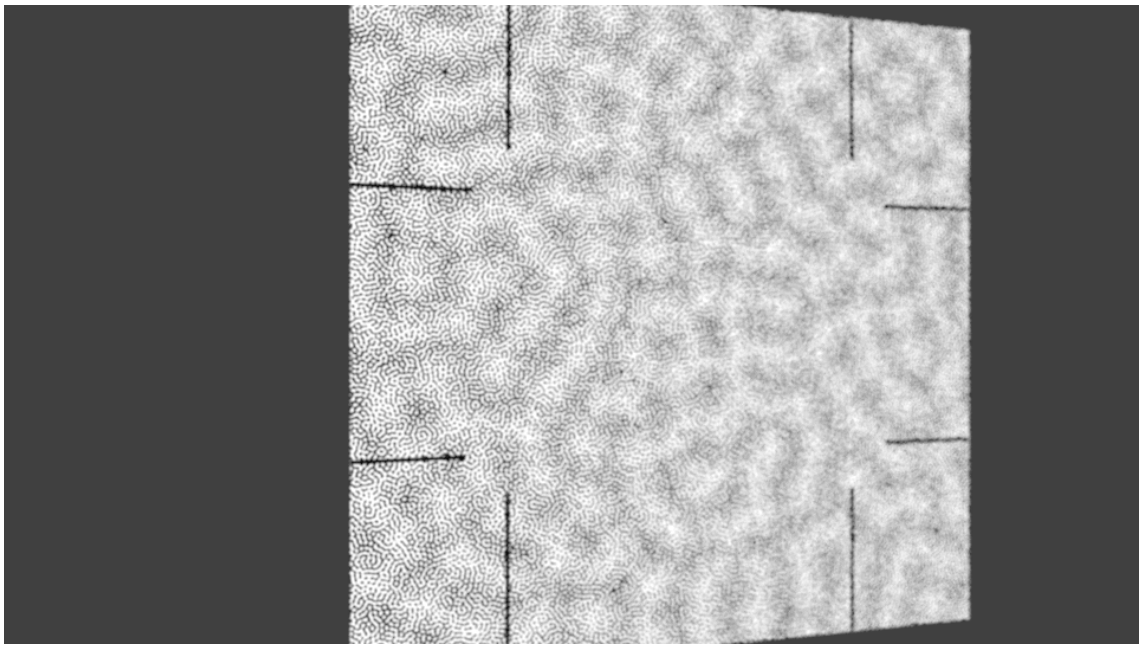

Figure 36 Image quality when the point of focus of the left-hand camera is moved 16cm toward the camera in the positive z-direction. The speckle pattern appears blurry, particularly at the right-hand edge of the plate.

5.6 Angled and curved surfaces

The effects of changes in camera orientation were very similar when viewing curved surfaces to those observed for the plate. Most tests showed no significant differences in either strain or displacement characteristics. However, there were exceptions, with the effects of some camera motions being dependent on whether the cylinder was oriented with its axis parallel to the x-axis or the y-axis.

5.6.1 Curvature around the y-axis

When viewing a cylinder oriented parallel to the y-axis, transformations t_x, t_z, R_y and R_z produced near identical results to those observed for the plate. Results for these tests are shown in Appendix 3. However, for translation along the y-axis and rotation about the x-axis, some slight differences were observed in relation to strain magnitude. The characteristic pattern of shear strain was also different, particularly in the latter case.

For t_y, maximum apparent strains were a few times greater than that observed on the plate. However, it should be noted that the magnitude of these errors was still small, and could be indistinguishable from more significant causes of strain in practical applications. Figures *37* and *38* show the displacements and strains observed on the cylinder, and the difference in strain values is clear when compared with figure *18*. Normal strains are close to uniform throughout the measured area. However, in the case of shear strain, lowest values can be seen at the left edge. Given the small strain variations, this observation could simply be attributed to noise, however, since it aligns with the direction of curvature and was not observed for the plate, the possibility of systematic error should not be dismissed.

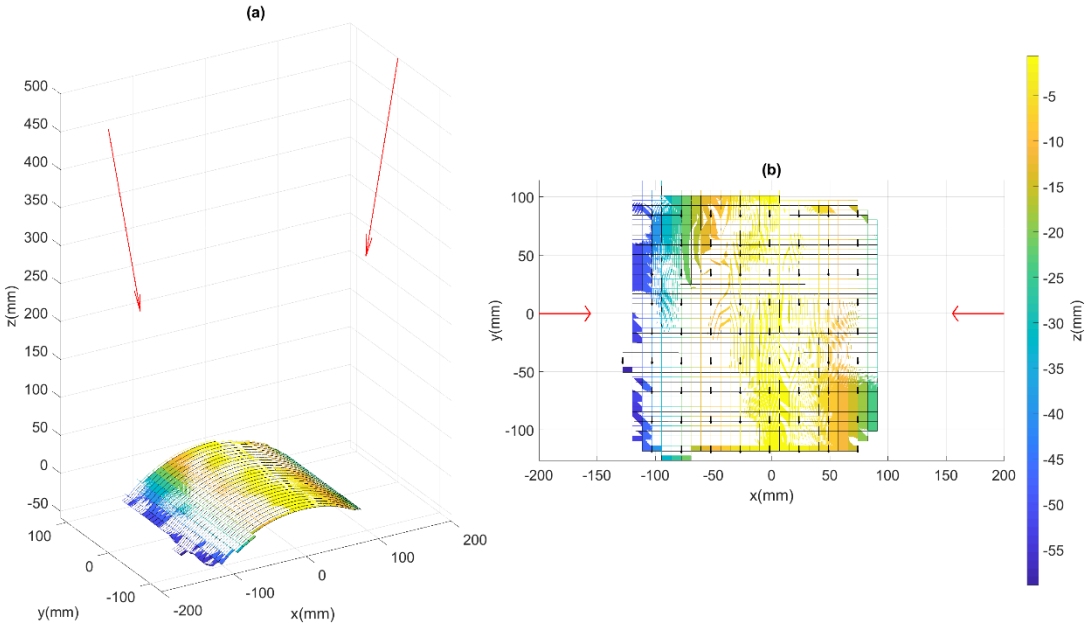

Figure 37 (a) Positions and poses of the cameras (red), cylindrical surface position (white mesh) and apparent measured plate position and deformation when the left-hand camera is translated 9mm upward in the positive y-direction. (b) The extent of apparent surface movement in x and y.

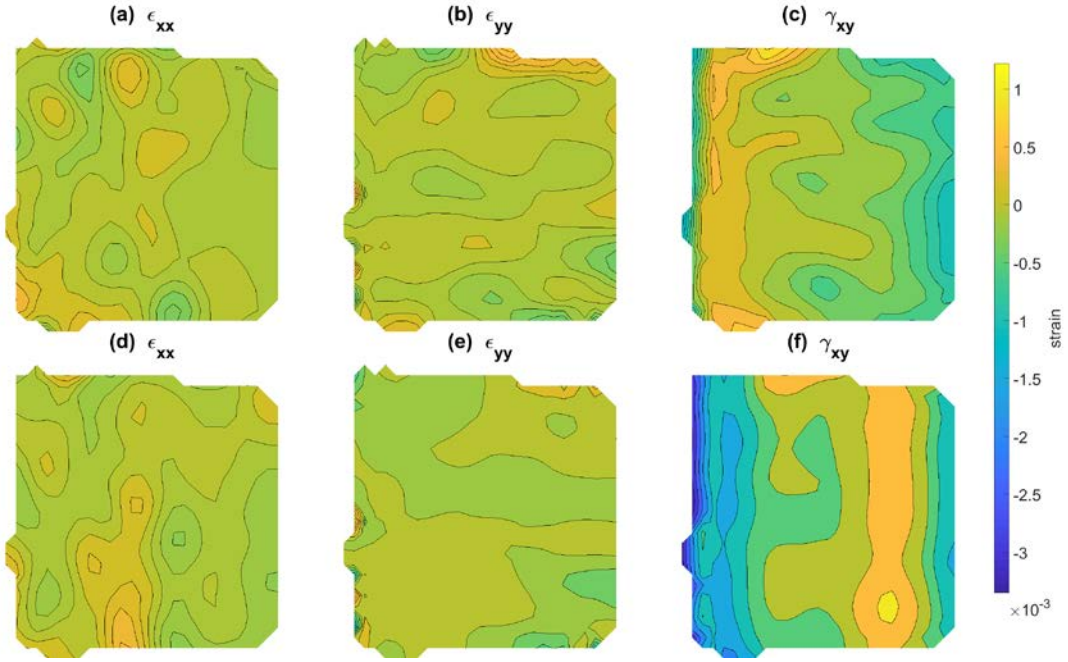

Figure 38 Apparent strains resulting from translating the left-hand camera upwards in the positive y-direction. (a), (b) and (c) show results for a 4mm translation and (d), (e) and (f) for a 9mm translation.

R_x was also observed to produce larger apparent strain magnitude on a curved surface than in the case of the plate. Results for the y-direction oriented cylinder are shown in figures *39* and *40*, and can be compared with the strain results for the plate shown in figure *25*. Maximum positive strain for both ϵ_{xx} and ϵ_{yy} components was in the range of 3-4% on the plate when compared with 4-5% percent on the cylinder. Minimum shear

strain values were approximately -2% on the plate, compared with approximately -5% on the cylinder.

Figure *25* shows that for the cylinder, apparent shear strain is not characterized by the distinctive local minimum that was observed on the plate. Instead, the minimum is seen at the edge of the field of view. Figure *41* shows a comparison of the contour plots between the two tests. The contours on the cylinder indicate that shear strain is approaching a local minimum somewhere just outside the field of view, but this is substantially less distinctive than the pattern observed on the plate. The reduced visible surface width in the case of the cylinder provides an obvious explanation for why this shear strain minimum value does not appear in the field of view. However, this reduced field of view also emphasizes that the strain gradients observed are significantly higher on the cylinder than on the plate.

In the R_x test, increased strain magnitudes were most apparent at the left and right edges of the measured area, where the surface curves away furthest from the camera. As discussed previously, a similar observation was made for t_y, though it is much less clear in that case. The fact that strain varies in the direction of curvature indicates that the phenomenon is a result of either increased distance from the camera or a changing of angle between the camera axis and surface. One important consideration is that both t_y and R_x cause an apparent y-direction shift through the view of the left-hand camera. Therefore, it is possible that the underlying cause of the increased strain gradients is the same in both cases. Greater distance between the camera and surface could be an explanation, given that a single pixel shift corresponds to greater movement in the real world for objects further in the background. However, this is true for all camera transformations, and no significant change in strain values was observed in the other cases. Additional testing would be required to reveal whether the effects of distance are independent of the surface angle and curvature.

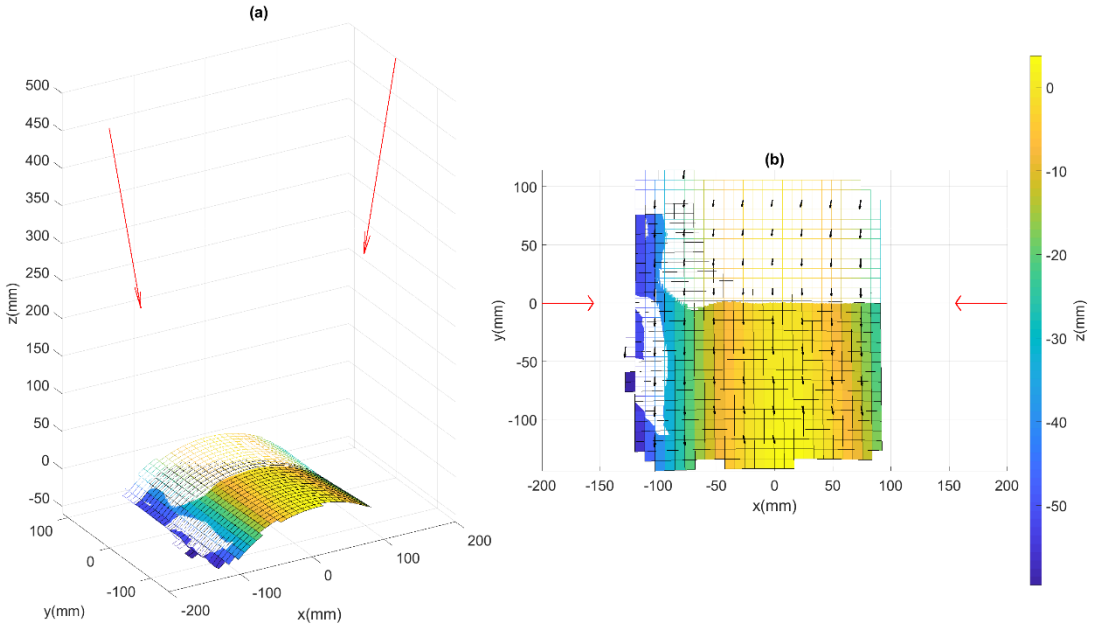

Figure 39 (a) Positions and poses of the cameras (red), cylindrical surface position (white mesh) and apparent measured plate position and deformation when the left-hand camera is rotated 6° about the x-axis. (b) The extent of apparent surface movement in x and y. Arrows indicate how the surface has deformed.

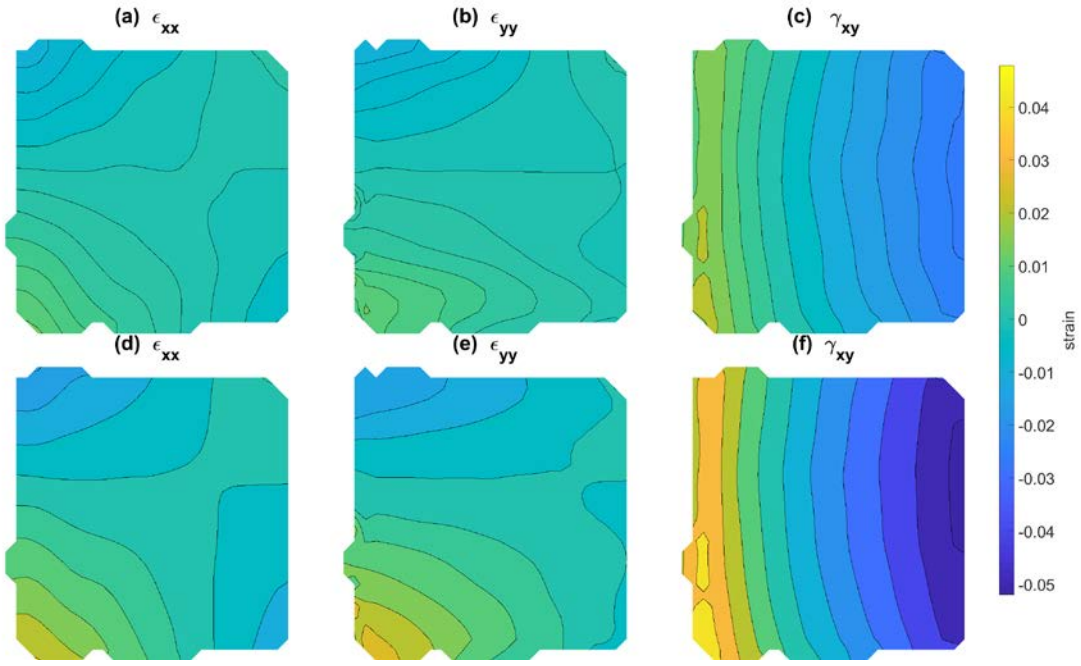

Figure 40 Apparent strains resulting from rotating the left-hand camera upward about the x-axis. (a), (b) and (c) show results for a 3° rotation and (d), (e) and (f) for a 6° rotation.

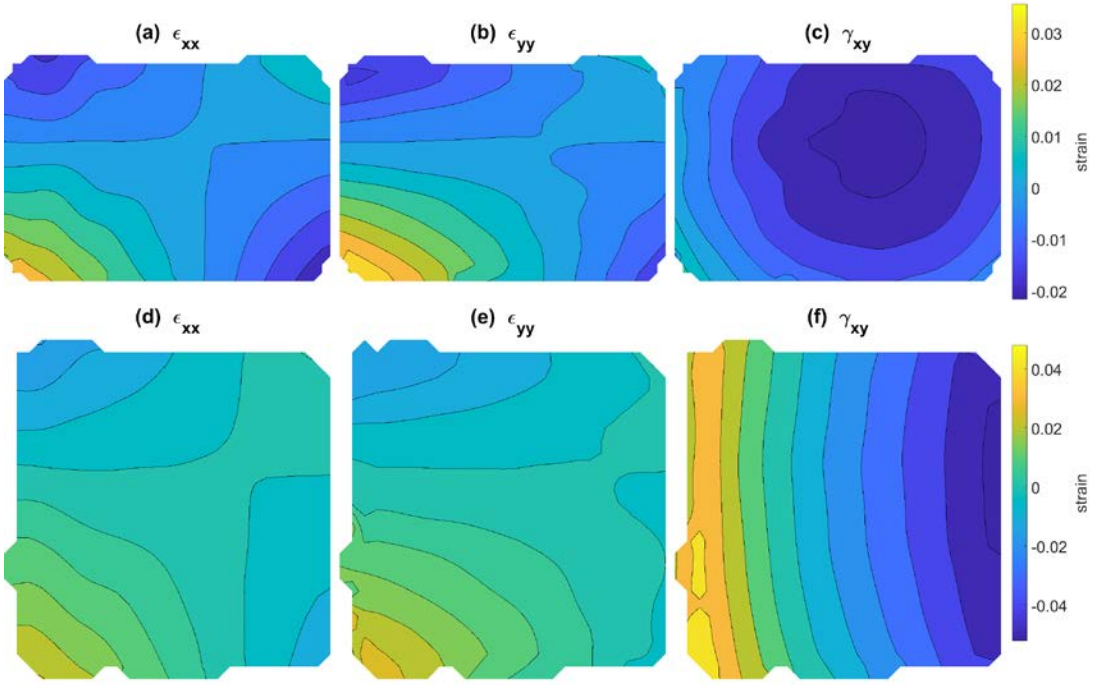

Figure 41 Apparent strains resulting from rotating the left-hand camera 6° upward about the x-axis. (a), (b) and (c) show results for the plate and (d), (e) and (f) for the cylinder oriented parallel to the y-axis.

5.6.2 Curvature around the x-axis

Results when viewing the cylinder oriented along the x-axis were again similar to those from the experiments performed on the plate. As per the y-oriented cylinder, camera transformations t_y and R_x were exceptions, differing from plate measurements in terms of strain magnitude and gradient. In addition, apparent strains resulting from R_y in this configuration were different to those observed for the plate.

Figures *42* and *43* show the resultant displacements and strains when the camera is translated along the y-axis. As in tests on other surfaces, small apparent strains can be seen. When comparing with figure *38*, we see that unlike the y-oriented cylinder, strain components ϵ_{xx} and γ_{xy} are of approximately the same magnitudes as observed for the plate. Maximum values of ϵ_{yy} are significantly higher than on the plate, but these are located on the top and bottom edges of the measured area, which differs to the results for the y-oriented cylinder. This suggests that the locations of these regions of higher strain gradient may not be random, since in both cases they were found to be on the parts of the surface that curved furthest from away from the camera. Again, it should be noted that camera translations in the y-direction do not result in large apparent strains, so the effects may not be detectable in practice and could also be attributed to noise.

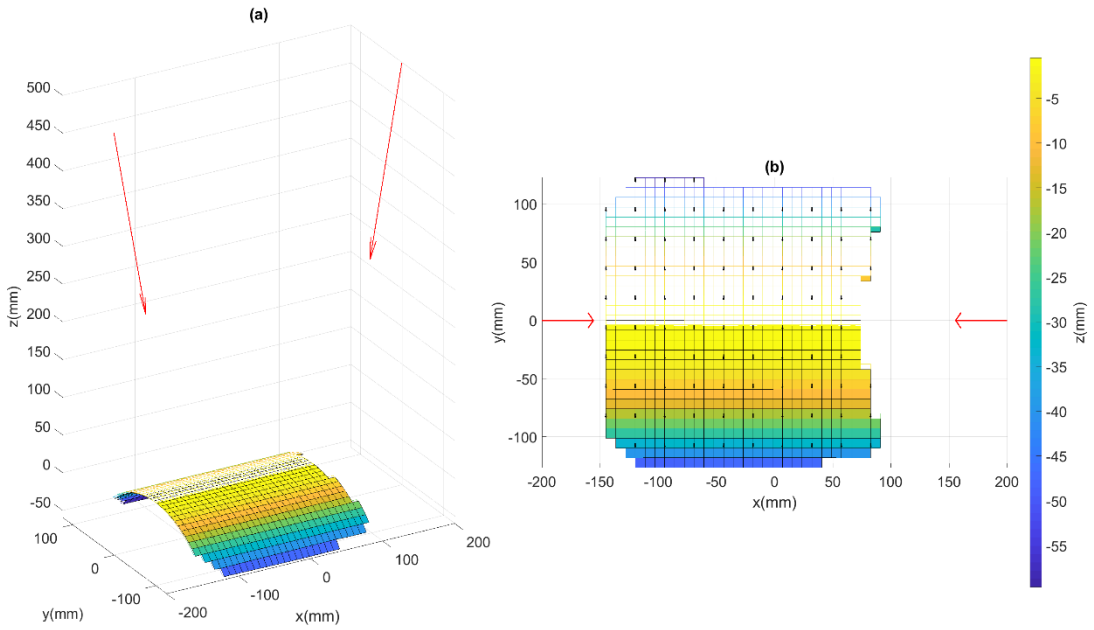

Figure 42 (a) Positions and poses of the cameras (red), cylindrical surface position (white mesh) and apparent measured surface position and deformation when the left-hand camera is translated 9mm along the y-axis. (b) The extent of apparent surface movement in x and y.

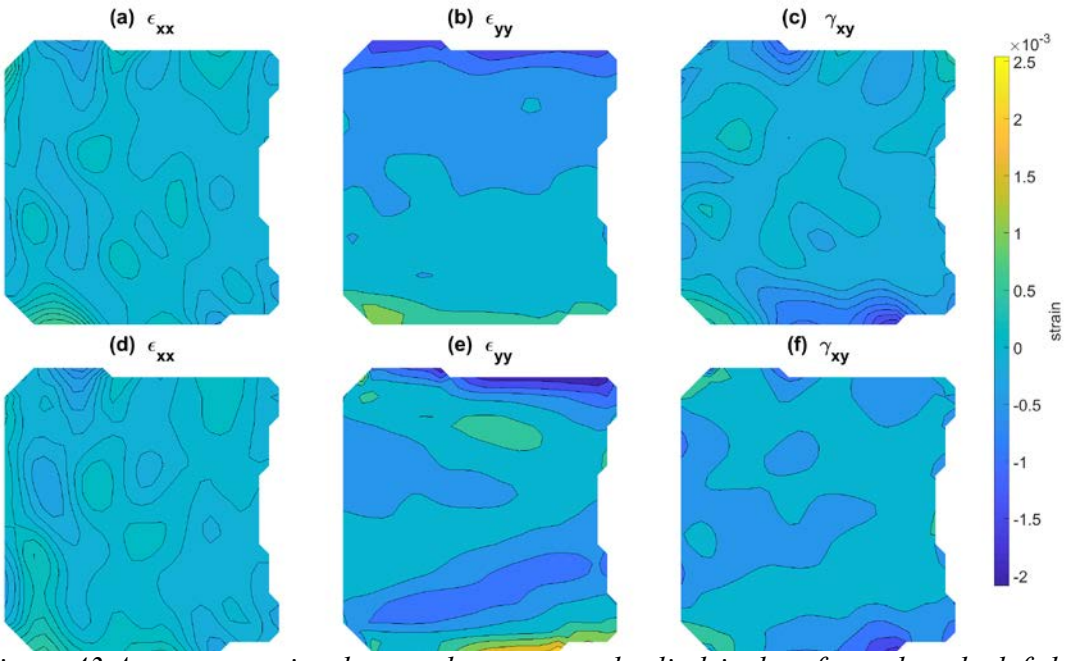

Figure 43 Apparent strains that result on a curved cylindrical surface when the left-hand camera is translated along the y-axis. (a), (b) and (c) show results for a 4mm translation and (d), (e) and (f) for a 9mm translation. The cylinder is orientated with its axis parallel to the x-axis.

The results for camera rotations around the x-axis are shown in figures *44* and *45*, and a comparison with the strain patterns from the plate test is shown in figure *46*. Similar results to the plate tests can be seen for strain components ϵ_{xx} and γ_{xy}. However, component ϵ_{yy} differs in two ways. Firstly, maximum and minimum strains on the cylinder are more than double those recorded for the plate. Secondly, a different strain distribution pattern can be seen. Instead of the distinctive saddle feature that was observed on the plate, strains appear to increase from minimum to maximum values when moving down across the surface in the negative y-direction. As with the observations for shear strain on the y-oriented cylinder, the shape of contours suggests that the strain pattern we see on the cylinder may be a small window of the pattern seen on the plate. If this is true, it again emphasizes that strain gradients on the curved surface are significantly larger.

R_y results were also noticeably different between the plate and the y-oriented cylinder. The apparent displacements and strains are shown in figures *47* and *48*, and a comparison with the plate results can be seen in figure *49*. The observed magnitudes of normal strains are very similar. However, the strain distribution pattern varies in both the x and y directions, while in the other tests it varied only in the x-direction. Results for shear strain are shown in figures *48* (c) and (f), and when compared with results from the plate test shown in figure *29*, we see that while the distribution pattern is similar, the magnitudes and gradients are significantly larger.

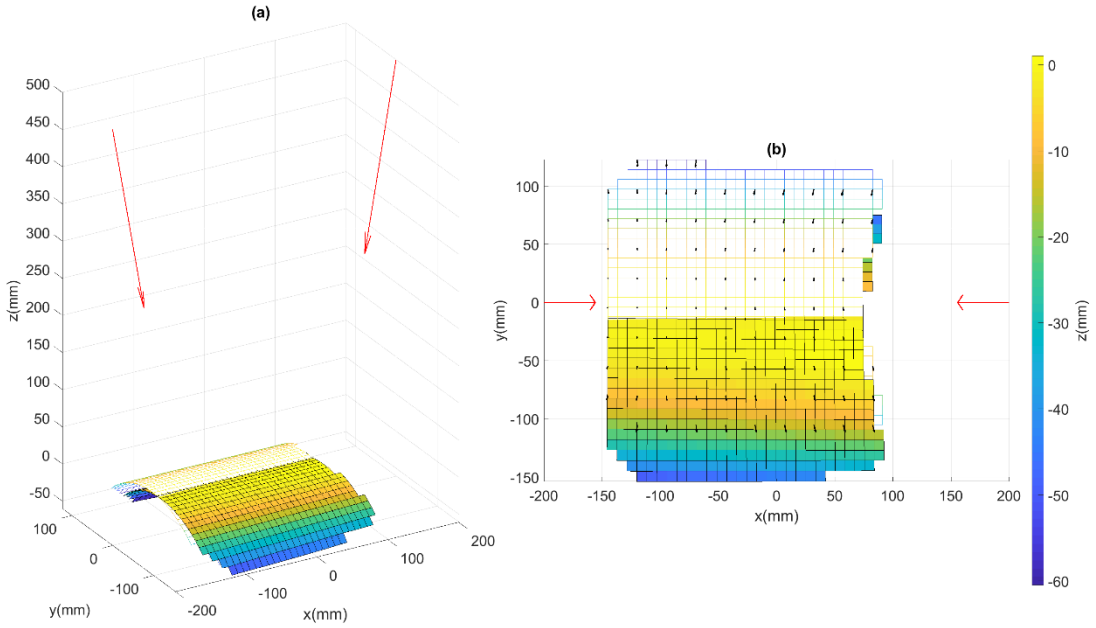

Figure 44 (a) Positions and poses of the cameras (red), cylindrical surface position (white mesh) and apparent measured surface position and deformation when the left-hand camera is rotated 6° about the x-axis. (b) The extent of apparent surface movement in x and y.

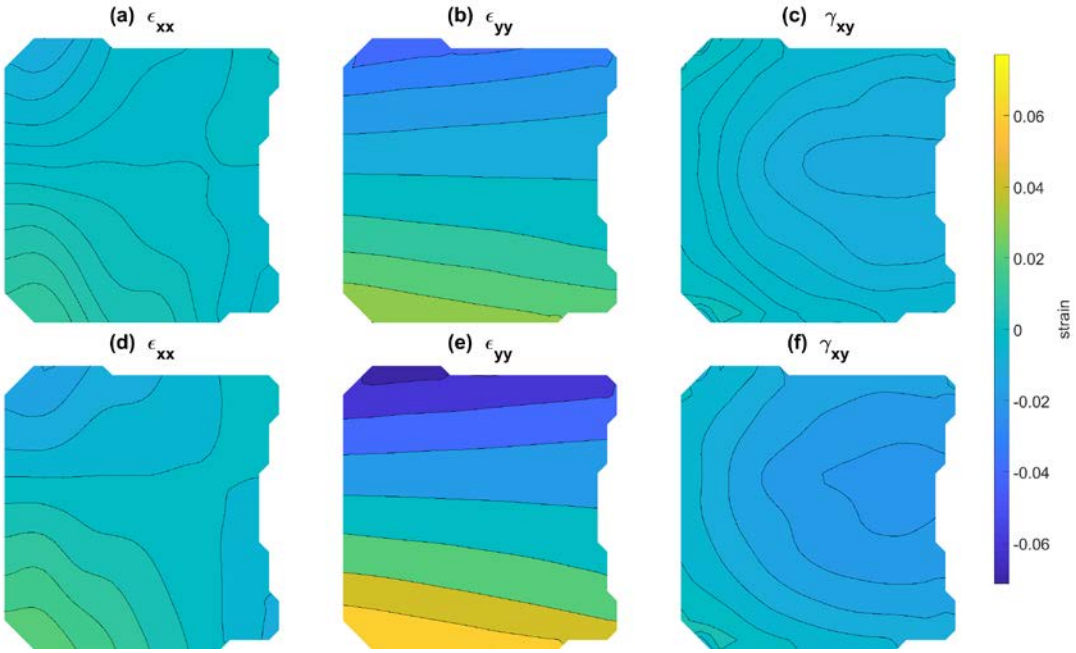

Figure 45 Apparent strains resulting from rotating the left-hand camera upward about the x-axis when viewing a cylinder orientated parallel to the x-axis. (a), (b) and (c) show results for a 3° rotation and (d), (e) and (f) for a 6° rotation. The cylinder is orientated with its axis parallel to the x-axis.

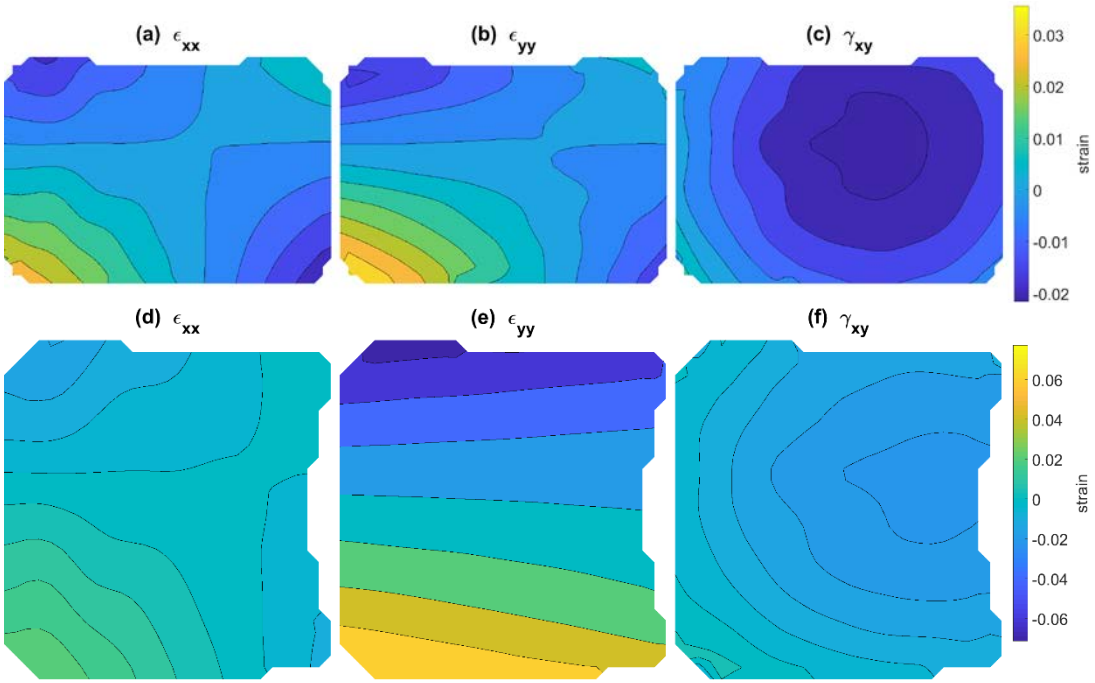

Figure 46 Apparent strains resulting from rotating the left-hand camera 6° upward about the x-axis. (a), (b) and (c) show results for the plate and (d), (e) and (f) for the cylinder oriented parallel to the x-axis.

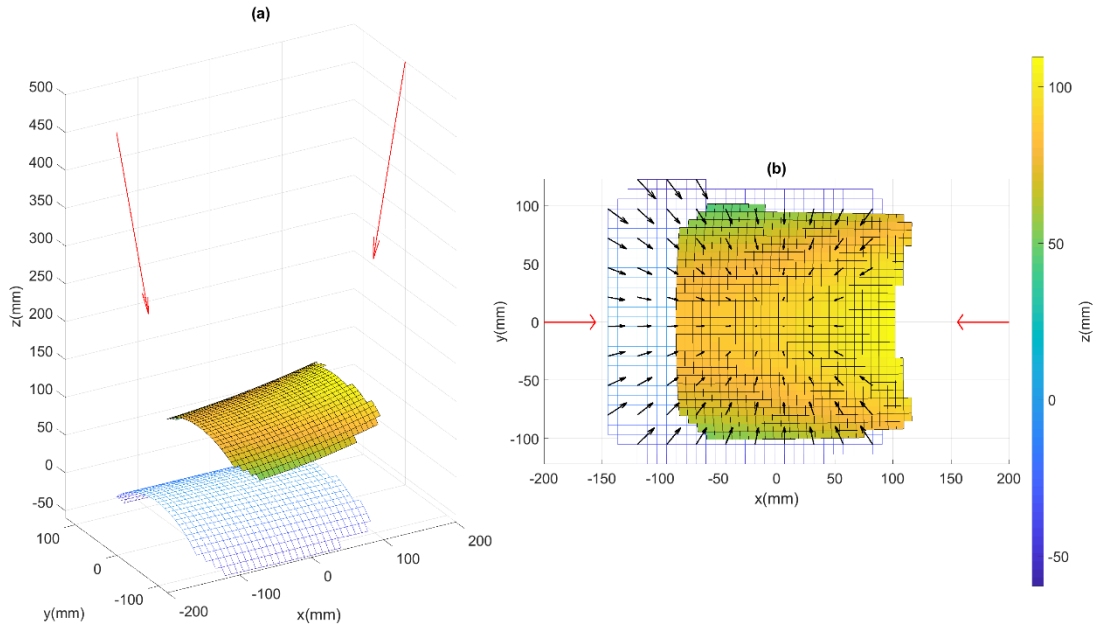

Figure 47 (a) Positions and poses of the cameras (red), cylindrical surface position (white mesh) and apparent measured plate position and deformation when the left-hand camera is rotated 9° away from the right-hand camera about the y-axis. (b) The extent of apparent surface movement in x and y. Arrows indicate how the surface has deformed.

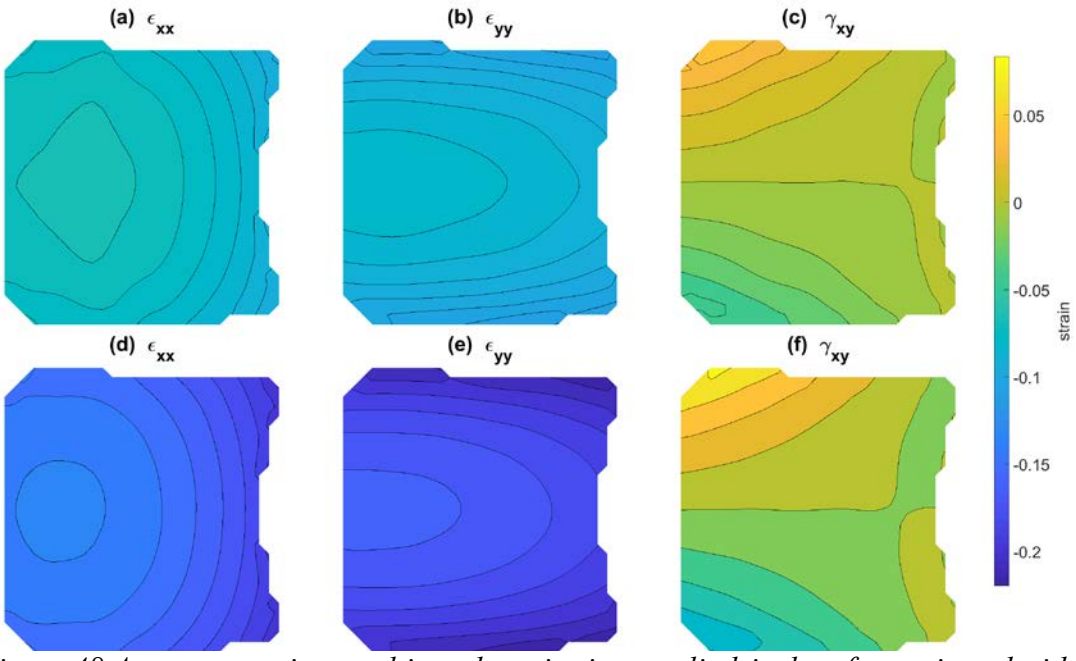

Figure 48 Apparent strains resulting when viewing a cylindrical surface oriented with its axis parallel the x-axis and the left-hand camera is rotated away from the right-hand camera about the y-axis. (a), (b) and (c) show results for a 5° rotation and (d), (e) and (f) for a 9° rotation.

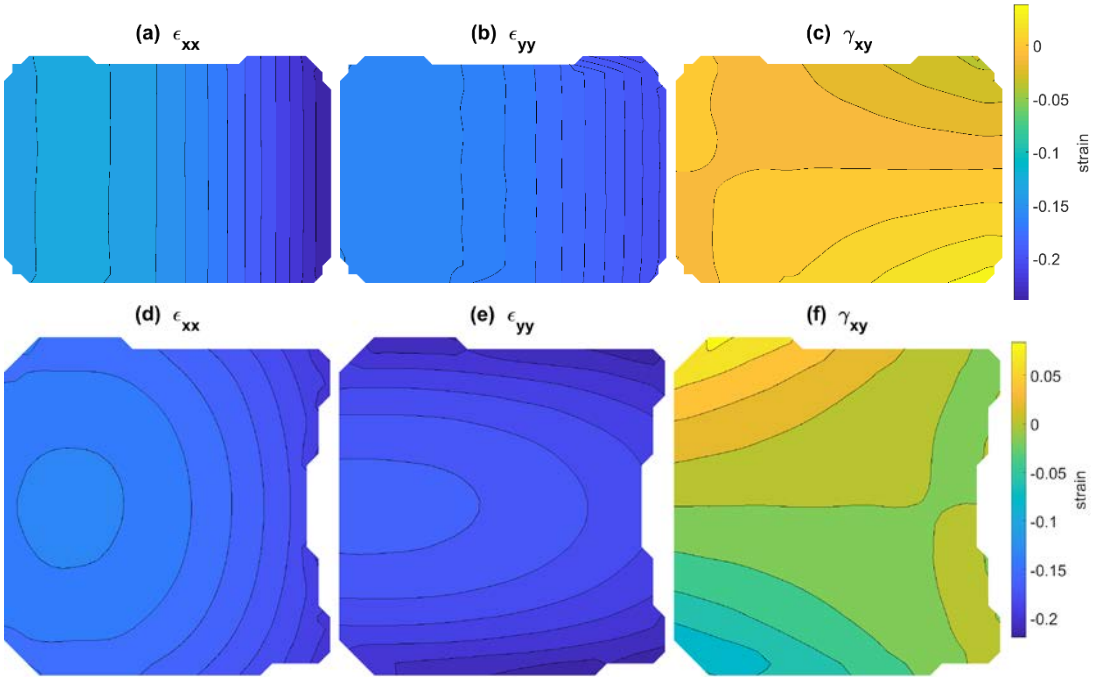

Figure 49 Apparent strains resulting from rotating the left-hand camera 9° away from the right-hand camera about the y-axis. (a), (b) and (c) show results for the plate and (d), (e) and (f) for the cylinder oriented parallel to the x-axis.

5.7 Implications and opportunities for future investigation

A consistent and significant finding of this thesis is that undesired camera motions produce predominantly systematic errors, while variations in lighting and camera focus produce random errors. This means there is the potential for camera motion to be compensated for with the appropriate inverse transformation. Systematic behavior was largely expected due to geometric constraints on the relationship between the surface displacement field and camera orientations. However, the finding is non-trivial given the uncertainties arising from the DIC process. As discussed in section 2.7, the potential exists for optimization algorithms to incorrectly match pixels between images. However, the results of this investigation suggest that with ideal lighting and optimized speckle patterns, the random errors caused by correlation failure are insignificant compared to the errors that should naturally result from unexpected camera motion.

Error analysis in this work has been largely limited to qualitative descriptions of displacement fields and strains. However, before such errors can be accurately identified and compensated for in practice, a precise mathematical description of them is required. This should therefore be the subject of future investigations if the suitability of DIC in uncontrolled environments is to be well understood. Additionally, the results presented here suggest that curved or angled surfaces display distinctive characteristics compared with those of flat surfaces for some camera motions. These effects also need to be understood in detail before precise correction of errors is feasible.

Any camera disturbance in practical applications is likely to comprise a combination of translations and rotations. Therefore, determining individual components of motion by identifying their separate characteristics is a recommended area of further investigation. Similarities between the error patterns of some of the camera transformations will likely make this process challenging. For example, translations along the y-axis display similar characteristics to rotations around the x-axis. This is due to the apparent motion of the surface in the moving camera view, as discussed in section 5.3.1. Likewise, translations along the x-axis and rotations around the y-axis could be difficult to distinguish from each other. The results of this thesis indicate that the contribution of rotations should be determined before that of translations, since they typically cause much greater apparent displacements and deformations. Also, translations along the z-axis and rotations around the z-axis both produce very distinct deformation characteristics. Therefore, it may be advantageous to identify their contributions first, which would then simplify the process of identifying more ambiguous camera motion components.

As mentioned, errors resulting from variable light and camera focus were found to be largely random. This means that they must be compensated for in a different manner to camera motion errors. Aside from filtering, it is expected that there is little post-processing that can be done after DIC is performed to improve accuracy of results. The effectiveness of filtering is dependent on the level of precision that is required, and whether any bias in the errors can be accounted for. Therefore, further investigation is needed to determine the suitability of filtering for correcting image blur or variable light induced errors.

As discussed in section 3, one existing method for mitigating the effects of variable lighting conditions is to use a combination of monochromatic illumination and optical filters [3]. This approach is well worth considering for industrial applications, though additional hardware and setup requirements may make it infeasible.

It may also be possible to compensate for inconsistent lighting and image blur using existing image processing techniques after images are recorded, but prior to performing DIC. Various methods exist for reducing glare, balancing local brightness discrepancies, and improving contrast [1,37]. However, depending on the method, these can have undesired effects such as introducing noise or reducing image sharpness. Image sharpening techniques also exist [1]. While they too tend to have the negative side effects of introducing artefacts and amplifying noise, improvements in the field continue to be made [38]. Further investigation into the suitability of combining image processing techniques with DIC may help to facilitate applications in industrial environments. The results presented here suggest that DIC has a reasonable level of robustness in relation to both image blur and variable light. This means that only a small amount of processing would be required in most circumstances, and that in turn, any negative effects may be tolerably small.

All DIC measurements conducted in this work were performed using default settings in DaVis. Specific parameter values are shown in Appendix 2. While these settings were considered suitable for the tests performed here, it should be noted that parameter choices could have an influence on results, and should therefore be the subject of further research. Adjusting the subset size may influence the magnitude of random errors and resistance to correlation failure due to variable lighting and image blur. This is because in both cases it is most likely that errors occur due to the system's inability to correctly identify fine features in the speckle pattern in the left-hand image. This leads to the possibility of incorrectly matching them with the un-altered features in the right-hand camera. Using larger subsets means that more data is included in the optimization process, and could therefore make it more likely that a correct pixel match between images would be found. However, the usual considerations for limiting subset size, such as extent of expected deformation, would apply in practical applications.

Correlation failure was also observed to occur for large camera rotations about the x-axis. It is possible that this could be addressed by using a different choice of shape function. As discussed in section 2.7, shape functions determine how well optimization algorithms can match between deforming subsets. Given the knowledge that calibration failure can result from large x-axis rotations, it may be possible to incorporate a shape function that can accurately describe the associated subset transformations.

It should also be noted that all the tests presented here utilized optimized speckle patterns. Applying such patterns to a surface is not always easy, depending on the scale, material and environment. This means that it may not be feasible to use them in some industrial applications. As mentioned in section 2.6, spray-painted speckle patterns are a common, versatile alternative that is suitable in most environments. DIC without speckle patterns has also been demonstrated on many occasions, and may be particularly appealing in some industrial settings. However, the image matching process is generally made more difficult by the camera disturbances and lighting changes that have been investigated here, and it is likely that in many cases errors would be greater with sub-optimal patterns. Therefore, continued research into alternative methods for applying optimized patterns would be beneficial in facilitating industrial applications of DIC. Similarly, investigations into the relationship between pattern quality and the errors identified in this thesis could be of value.

The camera motion and focus experiments assumed that only a single camera is disturbed. This is reasonable if the source of disturbance is expected to be a person or equipment

bumping the camera, but does not account for other error sources such as large vibrations, which would have the potential to move both cameras simultaneously. In the latter case, there is no fixed reference from which to determine camera motions, so it is unlikely that errors could be compensated for using the methods suggested thus far. Therefore, if simultaneous camera disturbance is likely, a completely different approach would be required for implementing DIC. One common method in computer vision is to place fixed control points in the field of view of both cameras so that motion can be tracked and the system can be re-calibrated at any time. As discussed in section 3, similar methods have been used previously for 2D DIC analysis of bridges [30,33]. However, this may not be feasible in some situations, as if one cannot guarantee that a camera is not disturbed, then the same is probably true for control points. Another alternative would be to place optical targets on the DIC cameras themselves, and use additional cameras to monitor their motions from a distance. This would have the advantage that a single camera can monitor the motions of multiple cameras dispersed over a wide area. Also, the possibility of placing them far away increases the likelihood of being able to position them such that disturbance is unlikely.

6 Conclusion

This thesis investigated the types of errors that occur in DIC measurements when a camera is moved, its focus adjusted, or lighting conditions vary between calibration and recording of surface images. Open source, ray tracing software (Blender) was used to model these effects and produce photo-realistic images. These were then used to perform measurements with commercial DIC software (DaVis). Increasing the dimensions of a plate in Blender by 5% and measuring the same size increase in DaVis verifies that ray tracing software is a suitable tool for simulating stereo imaging systems, capable of producing images that are compatible with DIC programs. The ability to precisely define lighting conditions and camera motions could make such software a valuable tool for conducting further research in the field.

Camera motions were found to cause systematic errors, with each translation and rotation component observed to cause an apparent displacement field with distinct characteristics. Precisely defining the mathematical relationships between camera movements and errors could allow for them to be identified and corrected for in industrial applications, and should be the subject of further research.

Camera translations along, and rotations around, the z-axis both result in clearly identifiable apparent displacements and strains. It is therefore likely that separating these effects from those of other camera motions would be relatively simple, and doing so first might facilitate the subsequent correction of more subtle transformations. In general, rotations cause larger and more distinct errors than translations, due to the greater apparent shift of the surface in the view of the moving camera. It is recommended that rotations should therefore be accounted for before translations when correcting for camera motion.

The characteristic effects of most camera motions appear to be the same for measurements on a flat plate as for a curved surface. Therefore, it is believed that angle of the surface and distance from the cameras do not have a significant effect on measurement error in most cases. However, camera translations along the y-axis and rotations around the x-axis were found to result in slightly different deformation characteristics with higher strain magnitudes on curved surfaces. Discrepancies were observed for curvature around either the x or y axes, with slightly different outcomes in each case. Surfaces curving around the y-axis also exhibited different strain behavior compared with a flat plate in situations where a camera was rotated around the y-axis. The influence of surface curvature, angle and distance from cameras should be further investigated if they are to be accounted for when precisely defining the effects of camera motion.

It should be noted that correcting for camera disturbances is only considered possible in situations where a single camera is moved. Any applications that could result in both cameras being unknowingly disturbed, and where re-calibration is not possible, would require a different approach such as the use of stationary reference points or monitoring with additional cameras.

Changes in camera focus and variations in illumination were found to cause small but significant random noise. In practice, these errors would be difficult to distinguish from other noise sources. However, these results indicate that they become most significant when image quality is affected such that fine details in the speckle pattern are not visible

to the naked eye, due to either blur or glare. Therefore, it is likely that one would know when camera focus or illumination were a problem. In such cases, it may be possible to use existing image processing techniques to make photographs more suitable for DIC.

The results of this investigation suggest that DIC image matching algorithms are robust, and work well even when cameras are disturbed. This is evident from the small amount of random error recorded in most cases. However, excessive image blur and camera rotations around the x-axis beyond a certain extent were seen to cause correlation failure, and the same could be expected for other sufficiently large camera transformations or variations in illumination. Correlation failure, along with the random errors induced by changing camera focus and illumination, may have the potential to be addressed by changes to subset size. Choice of shape functions could also reduce the likelihood of subset matching failure being caused by camera motions.

DIC is a measurement technique with growing potential for industrial use. The initial insights provided by this thesis suggest that DIC algorithms have sufficient inherent robustness to perform in uncontrolled environments if the effects of likely error sources can be accounted for. With further investigation, it is considered likely that such errors could be reliably identified and corrected, thus allowing measurements of suitable accuracy to be performed in a wide variety of applications.

References

[1] R Klette, Concise computer vision - an introduction into theory and algorithms, Springer, London, 2014.

[2] MA Sutton, J Orteu, HW Schreier, Image Correlation for shape, motion and deformation measurements, Springer, New York, 2009.

[3] B Pan, D Wu, Y Liping. Optimization of a three-dimensional digital image correlation system for deformation measurements in extreme environments, Applied Optics. 51 (2012) 4409.

[4] M Malesa, M Krzysztof, U Tomczak, B Sivek, M Kujawinska, A Sieminska-Lewadowska. Application of 3D digital image correlation in maintenance and process control in industry, Computers in Industry. 64 (2013) 1301-1315.

[5] E Borgia. The Internet of Things vision: Key features, applications and open issues, Computer Communications. 54 (2014) 1-31.

[6] XG Wang, CH Liu, C Jiang. Simultaneous assessment of Lagrangian strain and temperature fields by improved IR-DIC strategy. Optics and Lasers in Engineering. 94 (2017) 17-26.

[7] C Wöhler, 3D Computer Vision - Efficient Methods and Applications, second edition ed., Springer, London, 2013.

[8] F Civerchia, S Bocchino, C Salvadori, E Rossi, L Maggiani, M Petracca, Industrial Internet of Things Monitoring Solution for Advanced Predictive Maintenance Applications, Journal of Industrial Information Integration. doi: 10.1016/j.jii.2017.02.003 (2017) 29.07.2017.

[9] IIC, The industrial internet consortium - about us. 2017 (2017).

[10] B Mellish, Pinhole-camera, public domain. (2005).

[11] A Nordman, Epipolar geometry, creative commons license CC BY-SA 3.0. (2007).

[12] S Birchfield, An Introduction to Projective Geometry (for Computer Vision), (1998).

[13] P Rönnholm, M McCluskey, Unpublished image, produced for the Aalto University course GIS-E3040 Advanced photogrammetry, Assignment 2, 2017.

[14] HC Longuet-Higgins, A computer algorithm for reconstructing a scene from two projections. in: Fischler MA, Firschein O (Eds.), Readings in Computer Vision: Issues, Problems, Principles, and Paradigms. Morgan Kaufmann Publishers Inc., San Francisco, 1987, pp. 61-62.

[15] D Nistér. An Efficient Solution to the Five-Point Relative Pose Problem, IEEE transactions on pattern analysis and machine intelligence. 26 (2004) 756.

[16] S Bossuyt, Optimized patterns for digital image correlation. Proceedings of the 2012 Annual Conference on Experimental and Applied Mechanics. Volume 3: Imaging Methods for Novel Materials and Challenging Applications (2013) 16.05.2017.

[17] K De Wilder, P Lava, D Debruyne, Y Wang, G De Roeck, L Vandewalle. Experimental investigation on the shear capacity of prestressed concrete beams using digital image correlation. Engineering Structures. 82 (2015) 82-95.

[18] B Triggs, P McLauchlan, R Hartley, W Fitzgibbon, Bundle Adjustment - A Modern Synthesis, in: Triggs B, Zisserman A, Szeliski R (Eds.), Vision Algorithms: Theory and Practice. IWVA 1999. Lecture Notes in Computer Science, vol 1883 ed., Springer, Berlin, Heidelberg, Berlin Heidelberg, 2000, pp. 298-300.

[19] M Kashfuddoja, M Ramji. Whole-field strain analysis and damage assessment of adhesively bonded patch repair of CFRP laminates using 3D-DIC and FEA, Composites: Part B. 53 (2013) 46-51.

[20] B Pan, H Xie, B Xu, F Dai, Performance of sub-pixel registration algorithms in digital image correlation, Measurement Science and Technology. 17 (2006) 08.05.2017.

[21] B Pan, K Qian, H Xie, A Anand, Two-dimensional digital image correlation for in-plane displacement and strain measurement: a review, Measurement Science and Technology. 20 (2009) 05.05.2017.

[22] M Bornert, P Brémand, P Doumalin, JC Dupré, M Fazzini, M Grédiac, et al. Assessment of Digital Image Correlation Measurement Errors: Methodology and Results, Experimental Mechanics. 49 (2009) 353-370.

[23] Z Gao, X Xu, Y Su, Q Zhang. Experimental analysis of image noise and interpolation bias in digital image correlation, Optics and Lasers in Engineering. 81 (2016) 46-53.

[24] P Lava, WV Paepegem, S Coppieters, ID Baere, Y Wang, D Debruyne. Impact of lens distortions on strain measurements obtained with 2D digital image correlation, Optics and Lasers in Engineering. 51 (2013) 576-584.

[25] W Tong. An Evaluation of Digital Image Correlation Criteria for Strain Mapping Applications, Strain. 41 (2005) 167-175.

[26] H Lu, PD Cary. Deformation Measurements by Digital Image Correlation: Implementation of a Second-order Displacement Gradient, Experimental Mechanics. 40 (2000) 393.

[27] JH Reif, JD Tygar, A Yoshida. Computability and complexity of ray tracing, Discrete & Computational Geometry. 11 (1994) 265.

[28] Z Xu, J Nielsen, J Yu, H Jensen, R Ramamoorthi, Minimal BRDF Sampling for Two-Shot Near-Field Reflectance Acquisition, ACM Transactions on Graphics - Association for Computing Machinery. 35 (2016) 11.05.2017.

[29] G Tran, Raytraced image of several glass objects, public domain. (2006).

[30] S Yoneyama, A Kitagawa, S Iwata, K Tani, H Kikuta. Bridge deflection measurement using digital image correlation. Experimental techniques. 31 (2007) 34-40.

[31] M Kujawinska, R Sitnik, G Dymny, M Malesa, K Malowany, D Szczepanek, Hierarchical, multitasks optical system for health monitoring of civil engineering structures, SPIE Proceedings. 7387 (2010) 12.07.2016.

[32] J Peddle, A Goudreau, E Carlson, E Santini-Bell. Bridge displacement measurement through digital image correlation, Bridge Structures. 7 (2011) 165-173.

[33] S Yoneyama, H Ueda. Bridge deflection measurement using digital image correlation with camera movement correction. Materials Transactions. 53 (2012) 285-290.

[34] B Pan, L Tian, X Song. Real-time, non-contact and targetless measurement of vertical deflection of bridges using off axis digital image correlation, NDT&E International. 79 (2016) 73-80.

[35] D Feng, M Feng. Experimental validation of cost-effective vision-based structural health monitoring, Mechanical Systems and Signal Processing. 88 (2017) 199-211.

[36] D Feng, M Feng. Vision-based multi-point displacement measurement for structural health monitoring, Structural Control and Health Monitoring. 23 (2015).

[37] E Abel, P White. Methods for removing glare in digital endoscope images, Surg Endosc. 25 (2011) 3898-3905.

[38] CP Cuong, JW Jeon. Efficient image sharpening and denoising using adaptive guided image filtering, IET Image Processing. 9 (2015) 71-79.

Appendix list

Appendix 1. Blender parameters used in experiments

Table A1.1 Blender parameters for camera motion experiments with plate.

Parameter	Values
Right-hand camera location x/y/z (m)	0.2/0/0.5
Right-hand camera pose x/y/z (°)	0/10/0
Left-hand camera initial location x/y/z (m)	-0.2/0/0.5
Left-hand camera initial pose x/y/z (°)	0/350/0
Sensor size (mm)	32
Focal length (mm)	16
F-stop	128
Focus	Auto-focus
Plate dimensions x/y/z (m)	0.6/0.6/0.01
Plate position x/y/z (m)	0/0/-0.005
Plate pose x/y/z (°)	0/0/0
Plate material finish (Blender category)	Diffuse BSDF
Area of diffuse lighting surface (m2)	4 x area lights, each 1m2
Area light locations x/y/z (m)	-0.5/0.5/0.6, 0.5/0.5/0.6, 0.5/-0.5/0.6, -0.5/-0.5/0.6
Area light poses x/y/z (°)	0/0/90
Area light strength (Blender unit)	100
Area light surface (Blender category)	Emission
Light color	White
Render engine	Cycles render

Table A1.2 Additional blender parameters for camera focus experiments with plate.

Parameter	Values
F-stop	1.8
Focus	Variable, 1cm increments in z-direction

Table A1.3 Additional Blender parameters for variable light experiments with plate.

Parameter	Values
Spotlight location x/y/z (m)	0/0/0.7
Spotlight pose x/y/z (°)	Variable, 4° increments around y-axis
Spotlight strength (Blender units)	150
Spotlight size (°)	30
Plate material finish (Blender category)	Glossy BSDF
Area light strength (Blender units)	3

Table A1.4 Additional Blender parameters for camera motion experiments with cylinder oriented parallel to the y-axis.

Parameter	**Values**
Cylinder location x/y/z (m)	0/0/-0.159
Cylinder pose x/y/z (°)	90/65/0
Cylinder dimensions x/y/z (m)	0.318/0.318/0.61

Table A1.5 Additional Blender parameters for camera motion experiments with cylinder oriented parallel to the x-axis.

Parameter	**Values**
Cylinder location x/y/z (m)	0/0/-0.159
Cylinder pose x/y/z (°)	0/90/0
Cylinder dimensions x/y/z (m)	0.318/0.318/0.61

Appendix 2. DaVis experimental settings

Table A2.1 DaVis StrainMaster vector processing settings.

Parameter	Setting
Correlation mode	Relative to first
Max. expected displacement	512 pixels
Surface height recalculation	No
Subset size	31
Step size	8
Calculation mode	medium
Outlier filter	Yes
Smoothing filter	Yes

Appendix 3. Supplementary curved surface results

Supplementary results for curvature around the y-axis

Translation along the x-axis

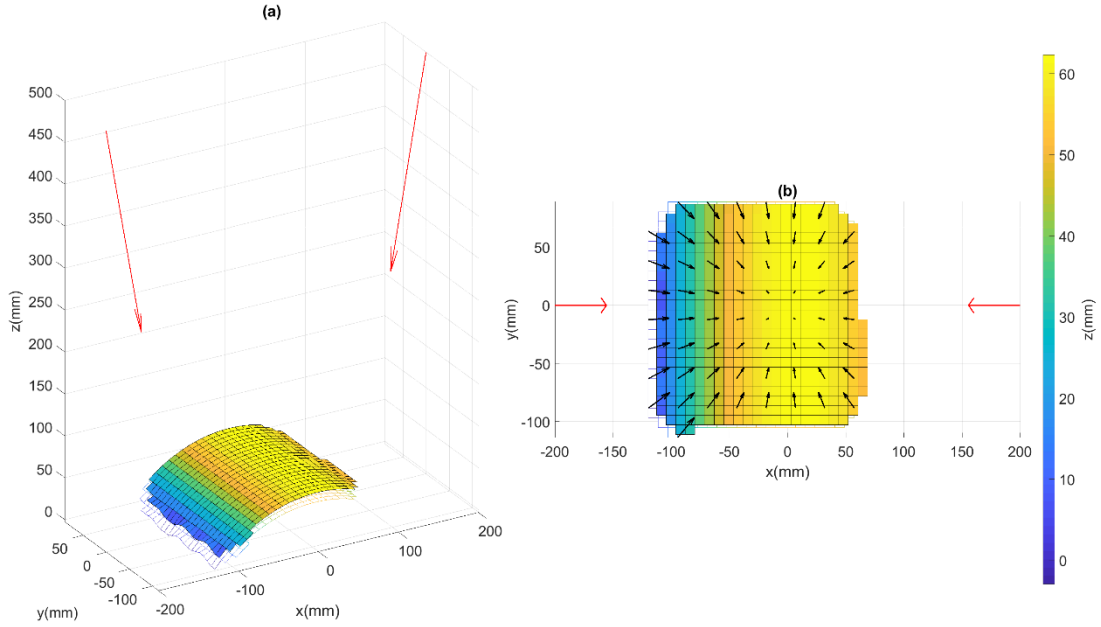

Figure A3.1 (a) Positions and poses of the cameras (red), cylindrical surface position (white mesh) and apparent measured plate position and deformation when the left-hand camera is translated 9mm away from the right-hand camera in the negative x-direction. (b) The extent of apparent surface movement in x and y. Arrows indicate how the surface has deformed.

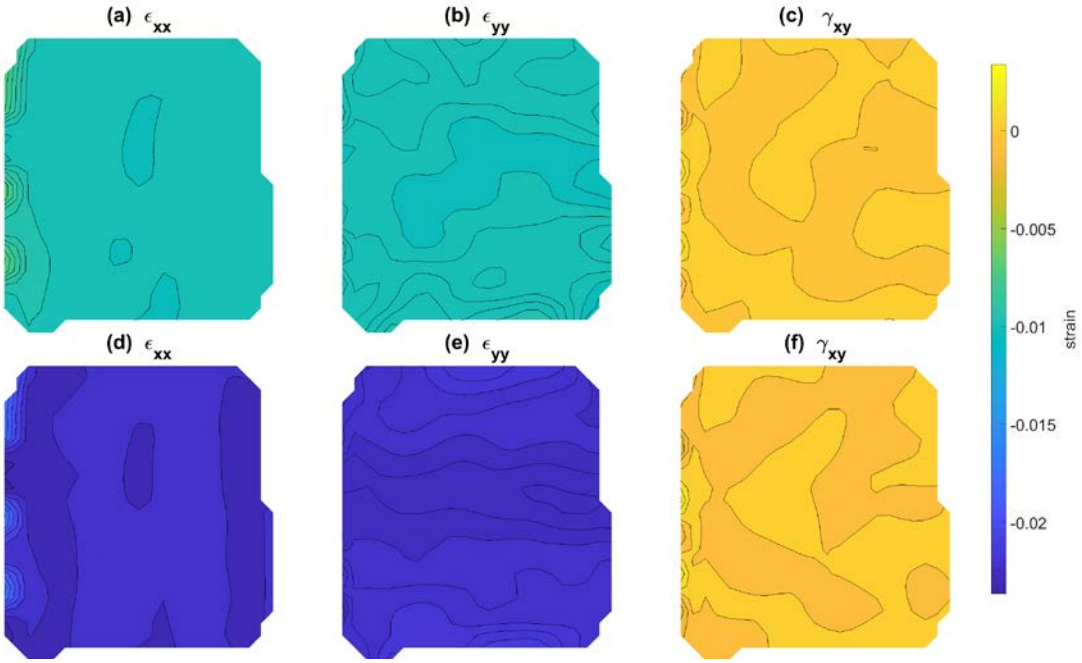

Figure A3.2 Apparent strains resulting from translating the left-hand camera leftwards in the negative x-direction. (a), (b) and (c) show results for a 4mm translation and (d), (e) and (f) for a 9mm translation.

Translation along the z-axis

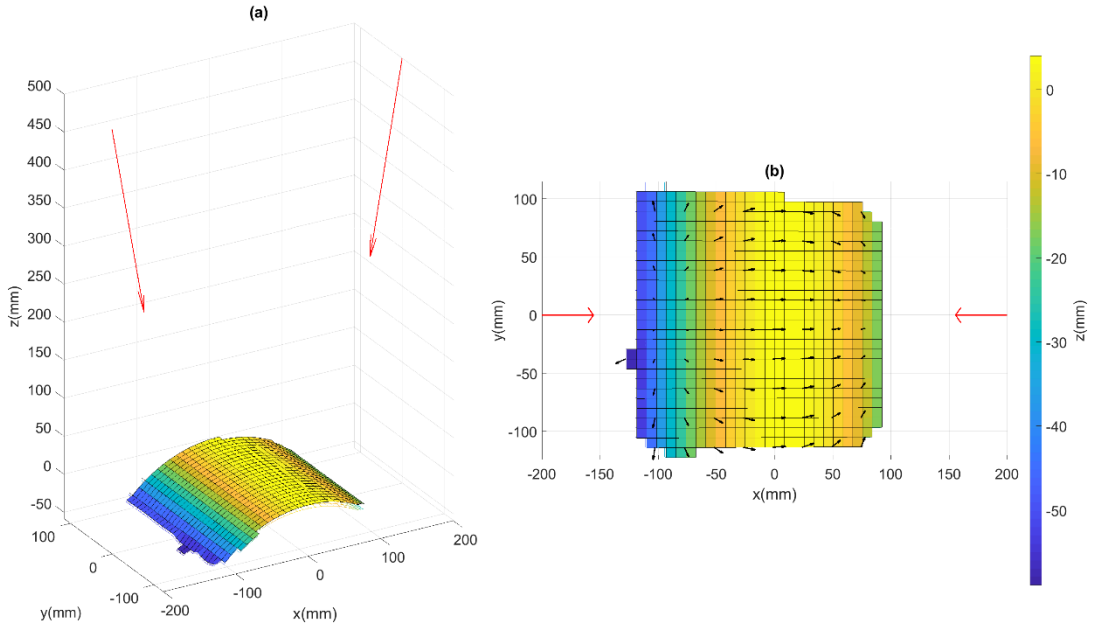

Figure A3.3 (a) Positions and poses of the cameras (red), cylindrical surface position (white mesh) and apparent measured plate position and deformation when the left-hand camera is translated 9mm toward the surface in the negative z-direction. (b) The extent of apparent surface movement in x and y. Arrows indicate how the surface has deformed.

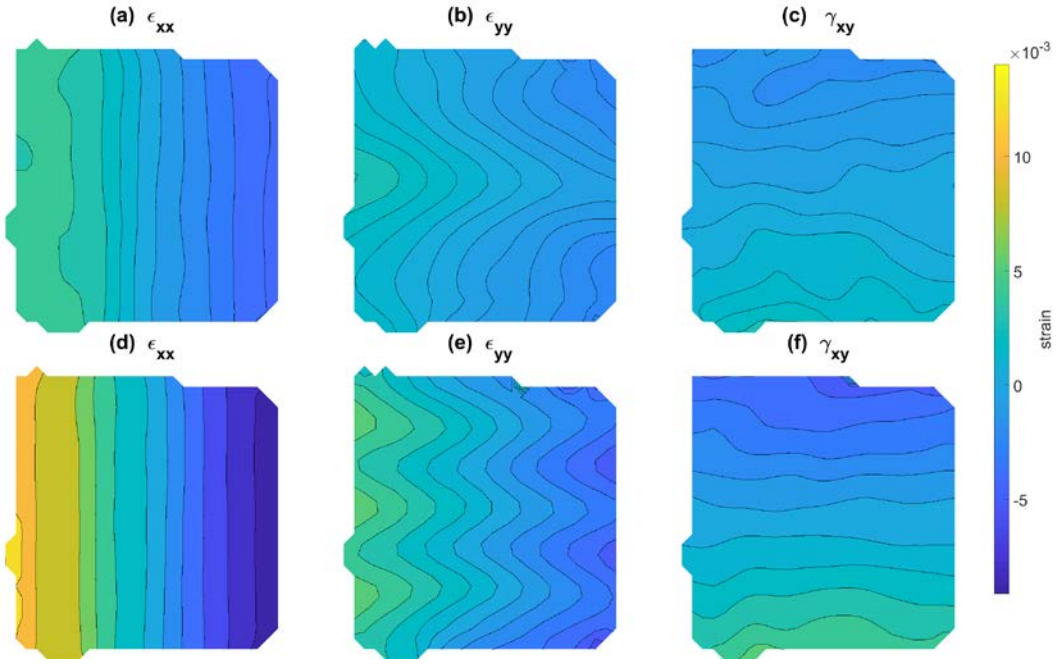

Figure A3.4 Apparent strains resulting from translating the left-hand camera forwards in the negative z-direction. (a), (b) and (c) show results for a 4mm translation and (d), (e) and (f) for a 9mm translation.

Rotation around the y-axis

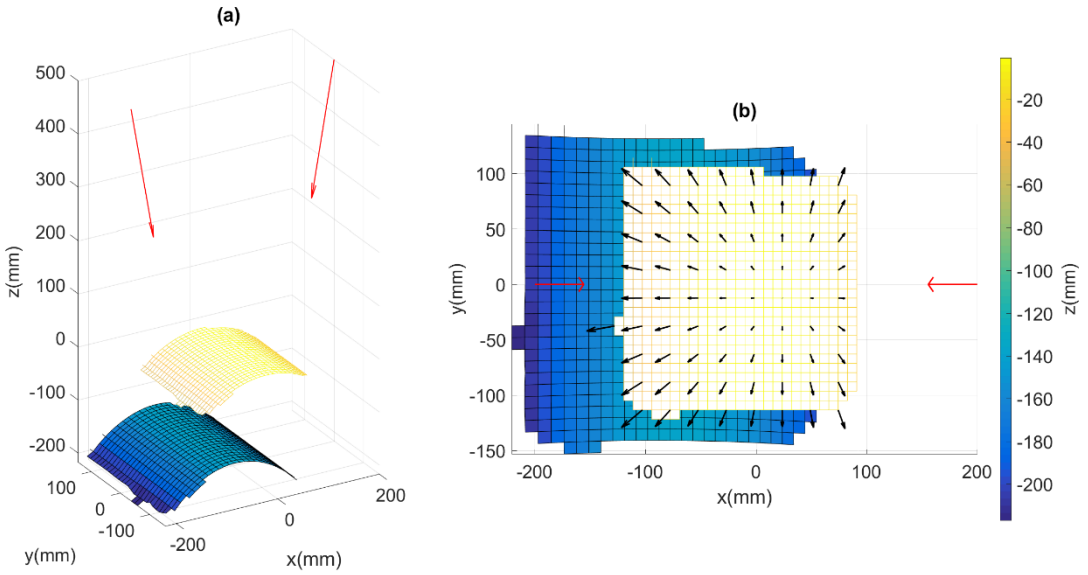

Figure A3.5 (a) Positions and poses of the cameras (red), cylindrical surface position (white mesh) and apparent measured plate position and deformation when the left-hand camera is rotated 9° away from the right-hand camera about the y-axis. (b) The extent of apparent surface movement in x and y. Arrows indicate how the surface has deformed.

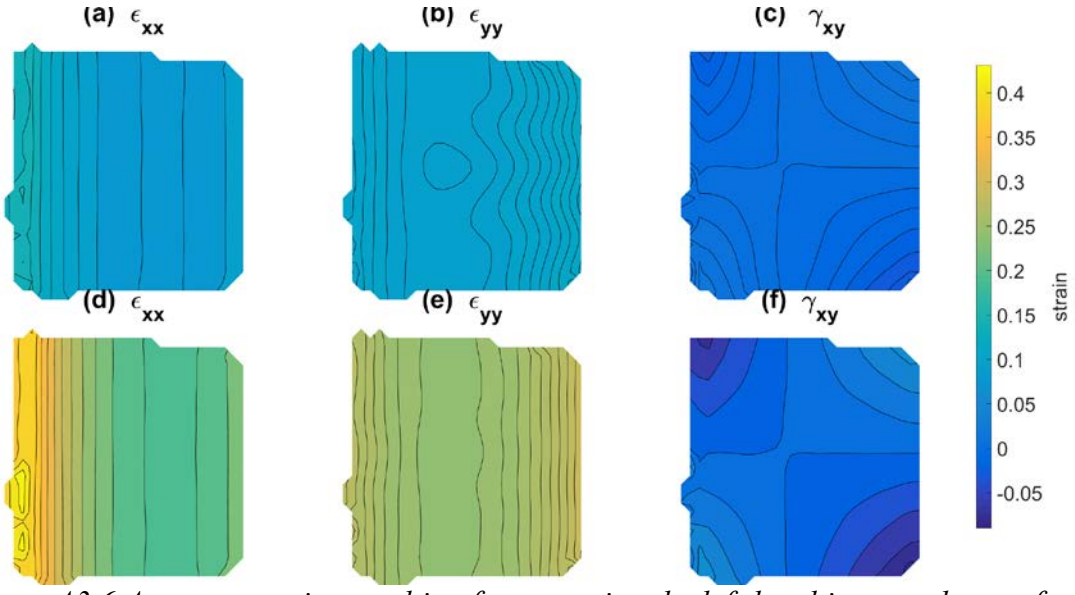

Figure A3.6 Apparent strains resulting from rotating the left-hand is rotated away from the right-hand camera about the y-axis. (a), (b) and (c) show results for a 5° rotation and (d), (e) and (f) for a 9° rotation.

Rotation around the z-axis

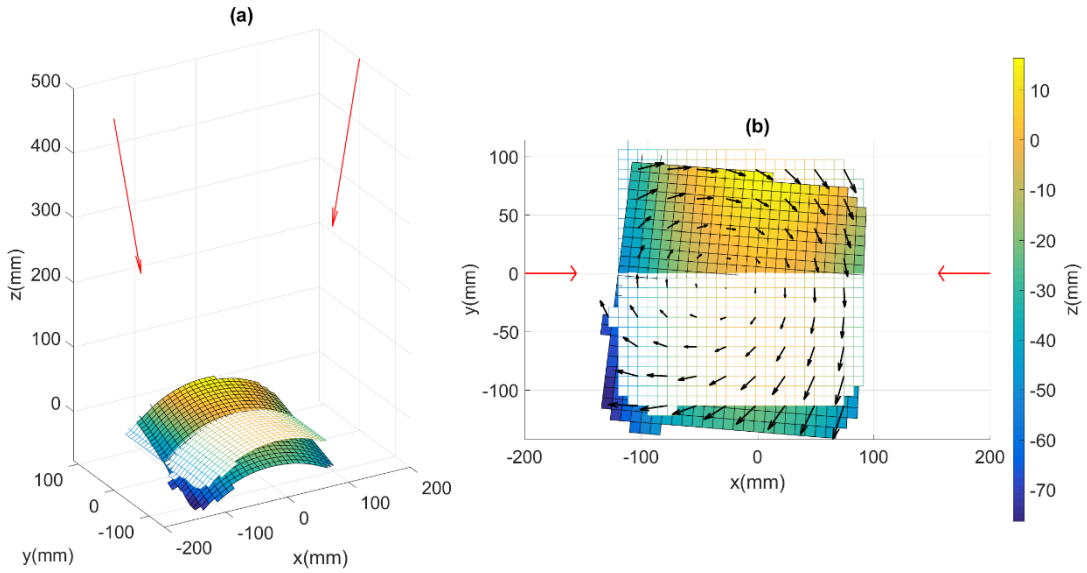

Figure A3.7 (a) Positions and poses of the cameras (red), cylindrical surface position (white mesh) and apparent measured surface position and deformation when the left-hand camera is rotated 9° around the z-axis. (b) The extent of apparent surface movement in x and y. Arrows indicate how the surface has deformed.

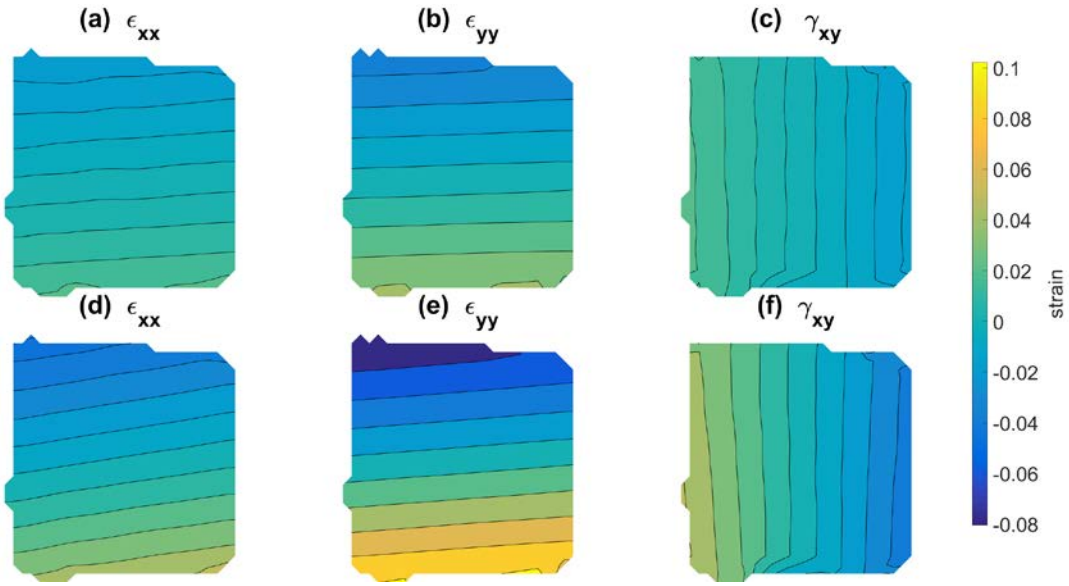

Figure A3.8 Apparent strains that result on a curved cylindrical surface when the left-hand camera is rotated in the positive direction about the z-axis. (a), (b) and (c) show results for a 5° rotation and (d), (e) and (f) for a 9° rotation. The cylinder is orientated with its axis parallel to the y-axis.

Supplementary results for curvature around the x-axis

Translation along the x-axis

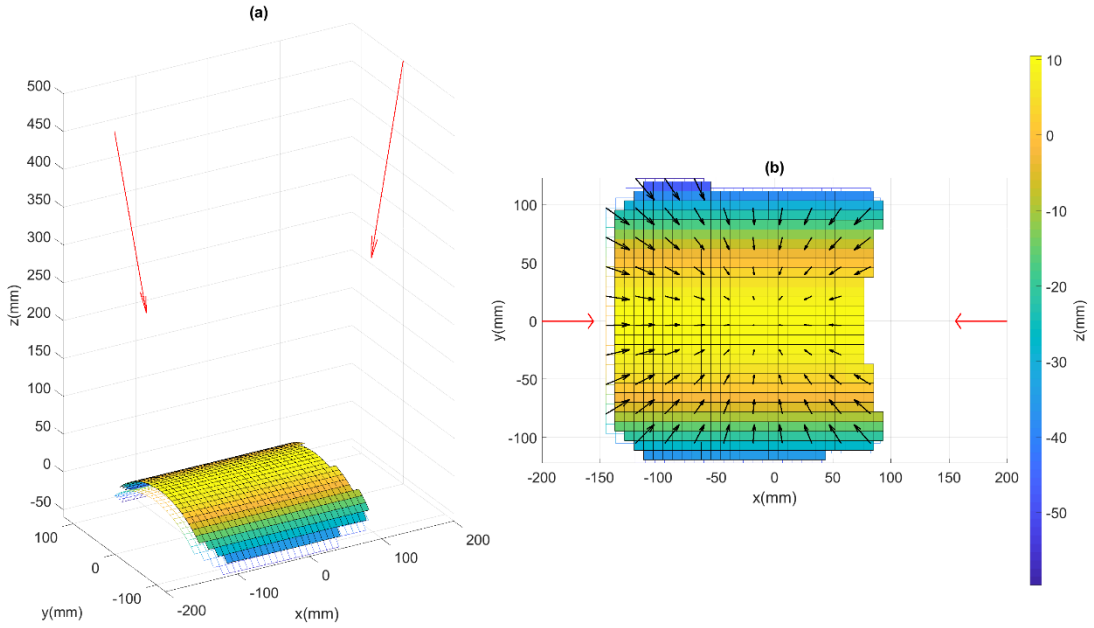

Figure A3.9 (a) Positions and poses of the cameras (red), cylindrical surface position (white mesh) and apparent measured plate position and deformation when the left-hand camera is translated 9 mm away from the right-hand camera along the x-axis. (b) The extent of apparent surface movement in x and y. Arrows indicate how the surface has deformed.

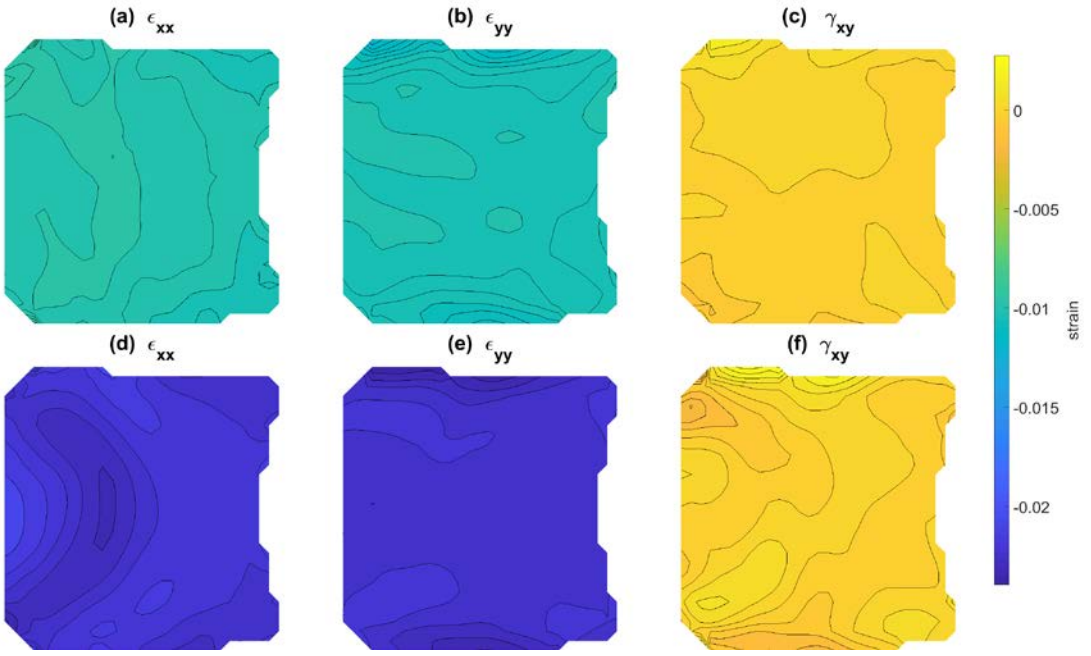

Figure A3.10 Apparent strains that result on a curved cylindrical surface when the left-hand camera is translated in the negative direction along the x-axis. (a), (b) and (c) show results for a 5mm translation and (d), (e) and (f) for a 9mm translation. The cylinder is orientated with its axis parallel to the x-axis.

Translation along the z-axis

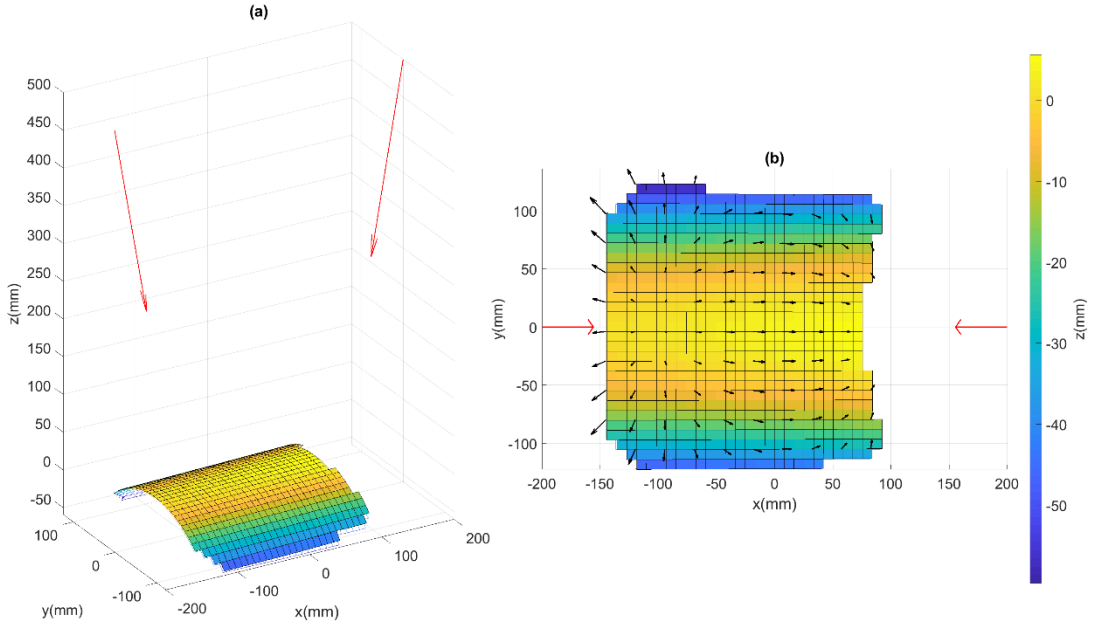

Figure A3.11 (a) Positions and poses of the cameras (red), cylindrical surface position (white mesh) and apparent measured plate position and deformation when the left-hand camera is translated 9 mm toward the surface along the z-axis. (b) The extent of apparent surface movement in x and y. Arrows indicate how the surface has deformed.

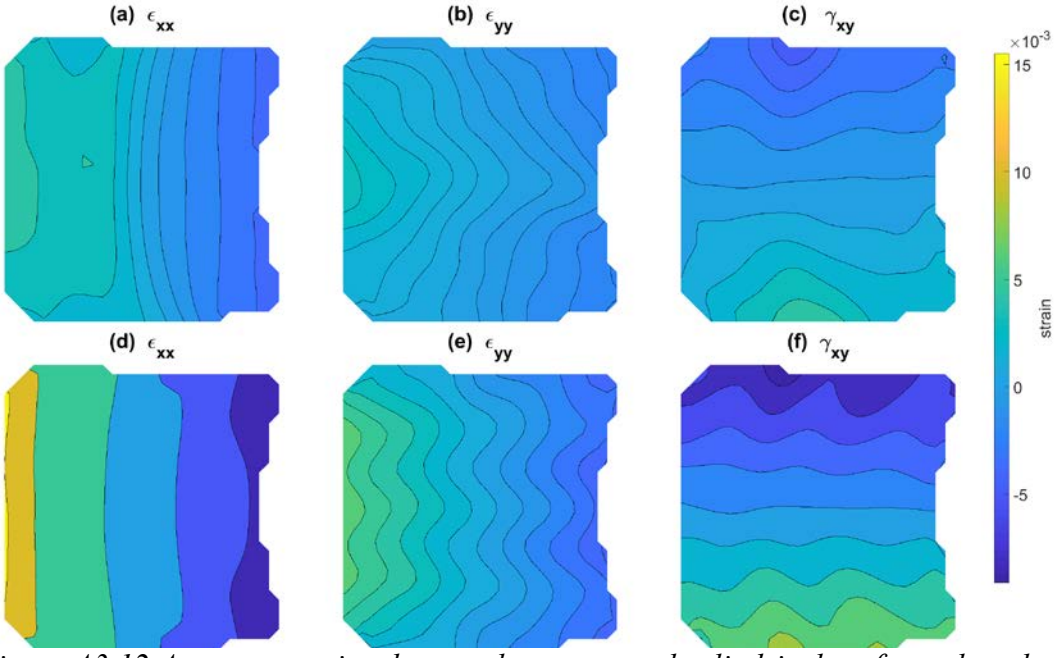

Figure A3.12 Apparent strains that result on a curved cylindrical surface when the left-hand camera is translated in the negative direction along the z-axis. (a), (b) and (c) show results for a 4mm translation and (d), (e) and (f) for a 9mm translation. The cylinder is orientated with its axis parallel to the x-axis.

Rotation around the z-axis

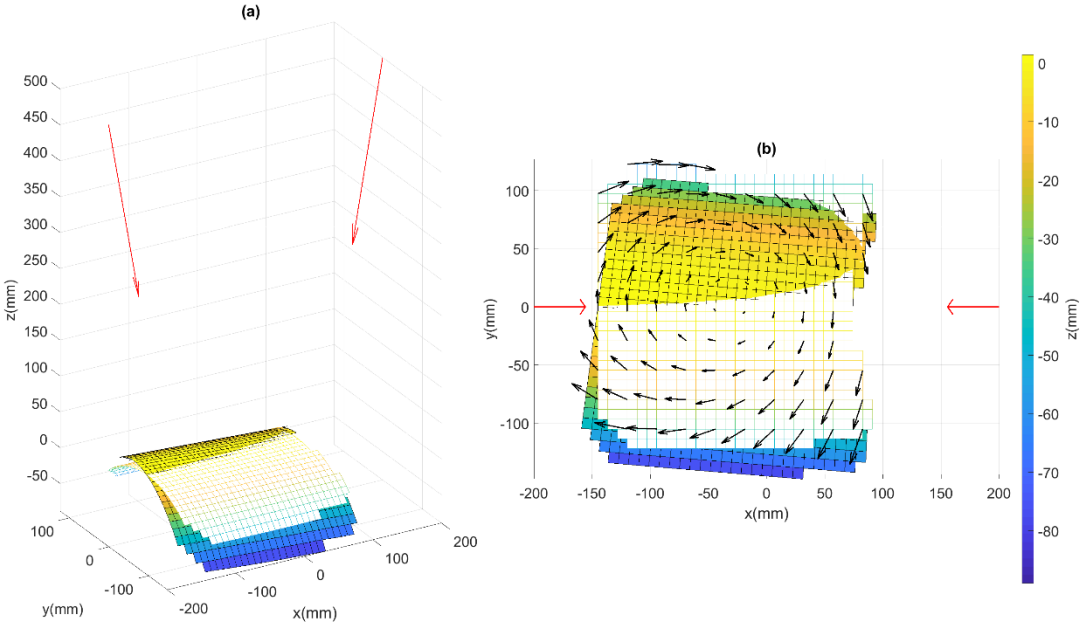

Figure A3.13 (a) Positions and poses of the cameras (red), cylindrical surface position (white mesh) and apparent measured surface position and deformation when the left-hand camera is rotated 9° about the z-axis. (b) The extent of apparent surface movement in x and y. Arrows indicate how the surface has deformed.

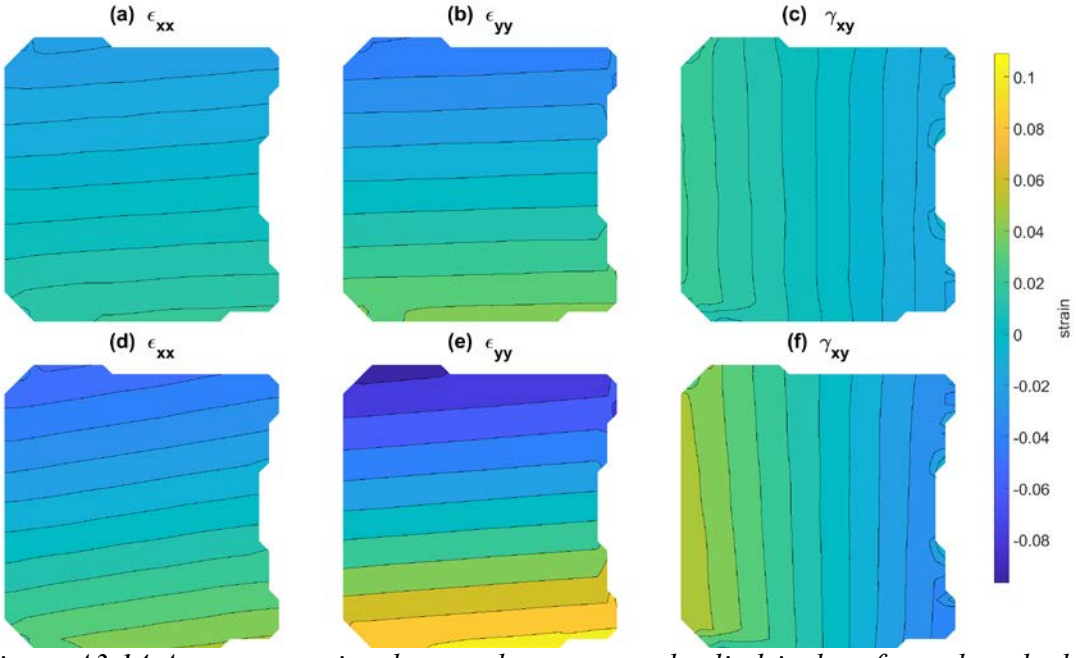

Figure A3.14 Apparent strains that result on a curved cylindrical surface when the left-hand camera is rotated in the positive direction around the z-axis. (a), (b) and (c) show results for a 4° rotation and (d), (e) and (f) for a 9° rotation. The cylinder is orientated with its axis parallel to the x-axis.